Title
Super-Resolution Imaging of Plasmonic Near-fields: Overcoming Emitter Mislocalizations

Author
Miao, Yuting

Publication Date
2021

Peer reviewed|Thesis/dissertation

UNIVERSITY OF CALIFORNIA
Los Angeles

Super-Resolution Imaging of Plasmonic Near-fields: Overcoming Emitter Mislocalizations

A dissertation submitted in partial satisfaction
of the requirements for the degree
Doctor of Philosophy in Chemistry and Biochemistry

by

Yuting Miao

2021

ABSTRACT OF THE DISSERTATION

Super-Resolution Imaging of Plasmonic Near-fields:
Overcoming Emitter Mislocalizations

by

Yuting Miao
Doctor of Philosophy in Chemistry and Biochemistry
University of California, Los Angeles, 2021
Professor Shimon Weiss, Chair

Plasmonic nano-objects have shown great potential in enhancing sensing, energy transfer and computing, and there has been much effort to optimize plasmonic systems and exploit their field enhancement properties. Super-resolution imaging with quantum dots (QDs) is a promising method to probe plasmonic near-fields. However, due to the strong coupling between QDs and plasmons, this technique is hindered by the formation of distorted point spread functions (PSFs) and QD mislocalizations. Chapter 4 of this dissertation investigates the coupling between QDs and 'L-shaped' gold nanostructures, and demonstrates both theoretically and experimentally that this strong coupling can induce polarization- / wavelength-dependent changes to the apparent QD emission intensity, polarization and position. From the magnitude and direction of the PSF shift under emission polarization modulation, the coupling strength can be extracted, and the true PSF location can be back-calculated from tabulated theoretical and experimental values. This discovery helps to better apply super-resolution imaging techniques to detect the plasmonic near-fields.

Besides using fluorescence intensity as the local-field intensity indicator, photophysical

properties of the emitter (e.g. on-time ratio) have shown to be a great candidate as well. Super-resolution fluctuation imaging (SOFI) has great potential in extracting the photophysical properties of emitters with super-resolution. In chapter 5, I discuss an open-source, modular SOFI analysis package we built for both reconstructing super-resolved plasmonic near-fields and engaging the SOFI community with a wide range of applications. Chapter 6 demonstrates how we characterize the photophysical properties of a specific fluorescent protein suitable for SOFI analysis. Our work provides a practical method with higher precision for plasmonic near-field mapping, which benefits many applications like biosensing and optical quantum computing.

The dissertation of Yuting Miao is approved.

Jianwei Miao

David Bensimon

Daniel Neuhauser

Shimon Weiss, Committee Chair

University of California, Los Angeles

2021

This dissertation is dedicated to my family.

TABLE OF CONTENTS

LIST OF FIGURES

ACKNOWLEDGMENTS

I would like to express my sincere gratitude to my advisor, Dr. Shimon Weiss, for providing inspiring guidance and advice throughout my Ph.D. training. With his support, I was able to develop both personally and professionally. I would like to thank Dr. Daniel Neuhauser for his support on instruction on the project of plasmonic near-field detection (chapter 4). Thank all the committee members for their devotion. I would also like to thank Dr. Xiyu Yi and Dr. Robert Boutelle for the valuable training on biological and optical experiments. Thanks Dr. Xiyu Yi for going through the SOFI theory with me, building up my confidence in coding, and help me implement the PySOFI package (chapter 5). I would like thank my collaborators, Dr. Anastasia Blake, Dr. Vigneshwaran Chandrasekaran for their contribution of DPN and g(2) measurements. Thanks Dr. Ivo Atanasov and Dr. Michael Lake for helping me with imaging single-molecule quantum dots and plasmonic structures using SEM and AFM. I would love to thank Dr. Leihao Wei for his love and support, for spending countless late nights with me. In the end, I would like to thank all the current and previous lab members of the Weiss lab for their help and inspiration. Thanks to University of California, Los Angeles (UCLA) and department of chemistry for providing me this precious opportunity.

VITA

2012–2016 B.S. in Materials Science and Engineering, Nanjing University of Science and Technology, Nanjing, China.

2016–2018 M.S. in Chemistry and Biochemistry, University of California - Los Angeles, Los Angeles, USA.

2018–2021 Ph.D. candidate in Chemistry and Biochemistry, University of California - Los Angeles, Los Angeles, USA.

PUBLICATIONS

Y. Miao*, R. C. Boutelle, A. Blake, V. Chandrasekaran, J. Hollingsworth, S. Weiss*, "Super-Resolution imaging of plasmonic Near-fields: Overcoming Emitter Mislocalizations," Manuscript

Y. Miao*, S. Weiss, and X. Yi*, "*PySOFI*: an open source python package for SOFI," Manuscript

CHAPTER 1

Introduction

1.1 Background and objectives

The rapid development of new fabrication techniques has allowed control of visible light at a subwavelength scale. The study of nanoscale light-matter interactions in metallic structures is known as plasmonics. Plasmonics is an emerging field with a broad range of possible applications where light manipulation is needed [11–13]. Plasmonic nanostructures have the ability to reduce the mode volume of propagating or standing light waves, leading to massive local-field enhancements for enhanced chemical sensing [14, 15], bio-sensing [16–18] and high-resolution bioimaging [19, 20].

A plasmonic system's structure, resonance frequencies, and field enhancement are all coupled, making their characterization difficult. Thus, with the development of plasmonics-based devices and circuits, there is a growing need for detecting and characterizing plasmonic effects in nanoscale systems. Typically, this information can be obtained through finite difference time domain (FDTD) simulations. However, experimental verification of simulation results is challenging since it usually requires sophisticated fabrication and imaging support. Even though advanced fabrication and synthesis techniques have driven down the size of structures to the nanoscale regime, the constructed plasmonic nanostructures might not match the modeled structures (e.g., uneven edges, rounded corners). In addition, when microscopic field structures are created, they can not be resolved by conventional optical microscopy. Current approach for measuring plasmonic fields like near-field scanning optical

microscopy (NSOM) [21–23], two-photon luminescence imaging [24, 25] and photoemission electron microscopy [rob37] either have low throughput or a high cost.

To map these minute-sized plasmonic fields optically, a super-resolution approach is preferred. In recent years, super-resolution imaging with single emitters (e.g., dyes or quantum dots) has emerged as a powerful method for detecting nanoscale structures and their near-fields. For instance, Cang and co-workers used freely diffusing fluorescent dyes to probe the field distribution inside the hotspots [26]. Each data acquisition determines the location of the dye through fitting with a point spread function (PSF), and the fluorescence intensity shows the field intensity at that location. Thus, knowing the true location of the emitter is crucial to map the field precisely. However, learning the true probe location and characterizing plasmonic near-fields is complicated by using an emitter's fluorescent intensity. For instance, when the probe is close to the metallic structure (less than 30 nm), fluorescence intensity changes non-monotonically because of quenching, and enhancement effects [27, 28]. The interaction with the metallic structure would also induce distortion to the apparent PSF of the system [7, 29]. Moreover, a user-friendly image processing package is in need to help researchers localize and extract the photophysical properties of the emitters.

The goal of this dissertation is to understand and develop approaches for better plasmon-enhanced super-resolution imaging. Since point-spread-function (PSF) distortion of QDs is polarization-dependent, and will affect the localization accuracy, especially at high labeling density, polarization modulation and characterization of the coupling strength is crucial to counteract mislocalization of QDs and to further optimize plasmon-enhanced single-molecule fluorescence imaging. Moreover, the overlapping between the plasmon resonance and QD emission spectrum also plays a crucial role in the coupling strength and PSF distortion. Thus, in this dissertation, measuring and decoupling the PSF of a QD close to a metallic surface from the distortion component with polarization and emission wavelength modulation is discussed. A Python package for super-resolution image analysis is introduced as well.

1.2 Thesis Overview

A comprehensive introduction to plasmonics is given in chapter 2, which includes two types of surface plasmons, surface plasmon polaritons and localized surface plasmon resonances, to understand plasmonics better. Chapter 3 covers the basics of super-resolution fluorescence imaging and how plasmonic nanostructures can enhance this type of imaging technique. In addition, the difficulty of localizing a single molecule on plasmonic surfaces using emitter dipoles is discussed. Later chapters focus on the effort to understand and develop approaches for better plasmon-enhanced super-resolution imaging. Chapter 4 illustrates a study of the interaction between plasmonic nanoantenna and fluorescent probes (quantum dots) and the relationship to the apparent localization and polarization of the probe. The far-field mislocalization and mispolarization of the probe are found to be determined by a combination of effects and vary at different positions relative to the plasmonic nanostructure. Both simulation and experimental methods for far-field super-resolution detection of plasmonic near-fields are discussed. An open-source Python package for SOFI analysis is covered in chapter 5. This package, named *PySOFI*, is designed to be user-friendly for both image processing experts as well as general SOFI users. It is facilitated with a collection of SOFI analysis and related post-processing methods and is highly customizable for various SOFI applications. Two new image analysis algorithms are introduced and demonstrated using *PySOFI* as well. Chapter 6 covers the characterization of a specific fluorescent protein designed for SOFI imaging and analysis. This mutant of Dronpa, called 'Dronpa-C12', has a prolonged blinking period before bleaching and is a great candidate for studies that require a long acquisition time. Different *in vitro* sample preparation methods are compared, and the procedure that produce the condition that mimics the live cell environment is determined. The response of Dronpa-C12 to the change of the local environment is explored. Lastly, the conclusions of these studies are presented along with the possibility of improving the experiment in the future and applying the technique to future research and applications.

CHAPTER 2

Plasmonics

There is an increasing need to control and manipulate light on the nanoscale as the sensing and imaging devices getting smaller and more compact. Plasmonics devices have provide novel ways of controlling light, and have shown great potential in broad applications, including enhanced chemical and biosensing, and high resolution bioimaging. For plasmonic nanostructures, light can be concentrated into a nanometer scale, enabling a large local field enhancement to increase the field intensity by several orders of magnitude [30, 31]. Thus, the analyte that was not able to be excited/detected originally, can be detected in this nanoscale region. In order to take advantage this phenomenon, a better understanding of the relationship between plasmonic structures and their local fields are crucial for optimizing the performance of nano-plasmonic devices.

Plasmonic systems have been optimized for different application scenarios, and their field enhancement properties have been explored extensively. However, the interplay between the system structure, plasmon resonance behavior, and field enhancement effect are still not fully understood. A better knowledge of near-field distribution around plasmonic devices would greatly enhance plasmonic systems optimization and application.

In this chapter, we go through a brief introduction of two types of plasmonic systems, surface plasmon polaritons and localized surface plasmon resonances. We discuss how they are generated and how their characteristics can be utilized to better manipulate light in nanoscale.

2.1 Overview

Plasmonics studies the interaction of electromagnetic fields (e.g., light) with metallic structures. When light hits an interface between metal and dielectric at the right frequency, the electromagnetic field is confined at this interface due to the induced oscillation of the electrons (plasmons) [2]. Surface plasmons (SPs) are collective coherent delocalized conduction-band electron oscillations induced by a strong light-matter interaction (figure 2.1). They usually exist in certain metals or doped semiconductors where the sign of the real part of the dielectric function shifts across the interface.

One characteristic of plasmonic devices is their ability to generate enormous local field enhancement within nanoscale dimensions with different field intensities and shapes (figure 2.1). SPs can be generated from the coupling between an external electromagnetic (EM) radiation and conduction electrons inside the metallic material. Thanks to the resonant excitation of SPs, plasmonic structures can concentrate energy into a nanoscale (under the diffraction limit) around themselves by interacting with incident photons from a much broader area [2, 32, 33]. Thus, plasmonics offers great potential for highly miniaturized and sensitive photonic devices by controlling, manipulating, and amplifying light on a nanometer scale. To date, the rapid development of a wide variety of plasmonic devices (e.g., waveguides [33, 34], filters [34, 35], and switches [36–38]) have been demonstrated, and their application has been extensively adopted for surface-enhanced Raman spectroscopy [39], plasmon resonance sensing [40, 41], and nanoscale optical spectroscopy [42]. These techniques would greatly benefit from a solid understanding of the interaction between plasmonic devices with different physical dimensions and molecules probed (e.g., dyes, 2D materials, quantum dots, and nanoparticles), which has not been thoroughly investigated.

Dependent upon the shape and dimension of the device, SPs can be classified as either localized (localized surface plasmons, or LSPs) or propagating (surface plasmon polaritons, or SPPs). For plasmonic nanostructures like a gold nanoparticle, electrons oscillate coher-

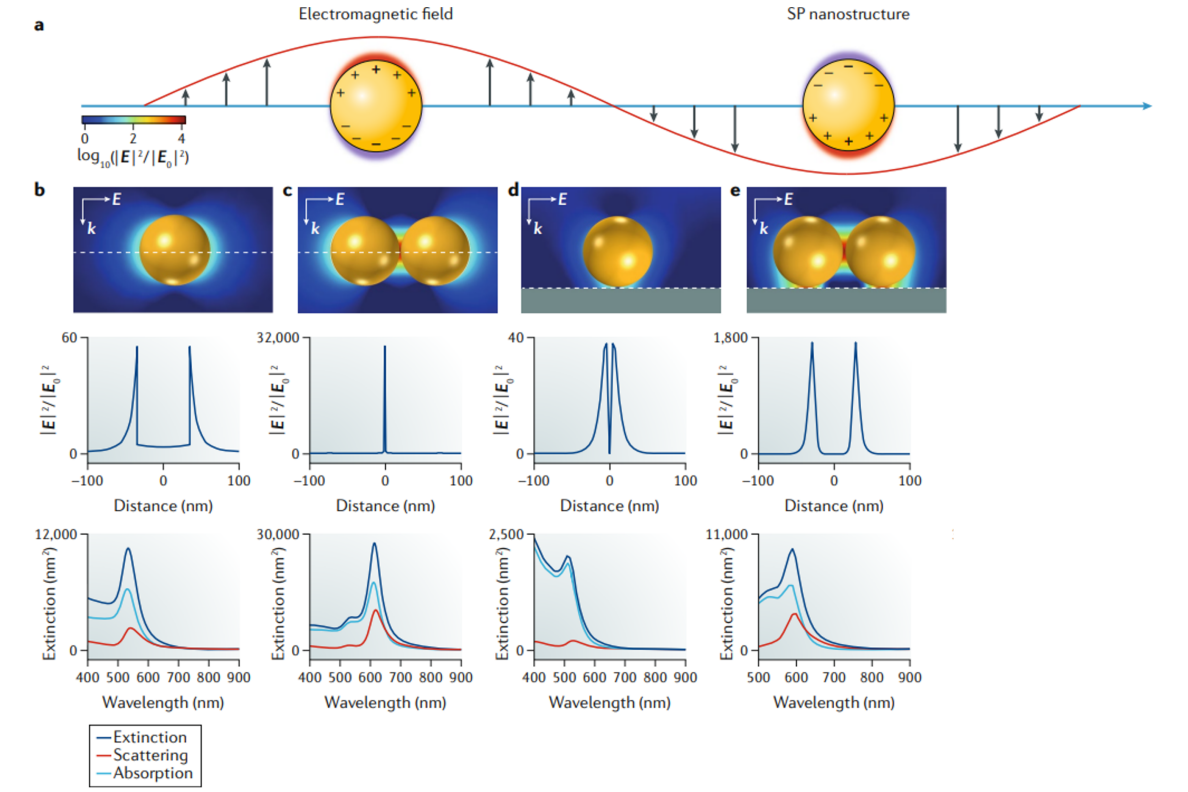

Figure 2.1: **Surface plasmon excitation, optical confinement and spectral features.** (a) Collective oscillation of conduction-band electrons in a nanostructure induced by incident light. (b-e) Electromagnetic field distributions (second and third rows) and extinction spectra (fourth row) of some typical Au nanostructures computed using finite-element simulations, where E is the electromagnetic field and k is the wave vector of incident light. (b) An isolated Au nanosphere of 60 nm diameter in vacuum. (c) A nanosphere dimer with a gap size of 2 nm in vacuum. (d) A single Au nanosphere at 1 nm distance from a flat Si surface. (e) The Au nanosphere dimer (gap of 2 nm) at 1 nm distance from a Si surface. The enhanced local electromagnetic field is expressed by $\frac{|E|^2}{|E_0|^2}$, where $|E|^2$ and $|E0|^2$ are the amplitude of the local and the incident electromagnetic field, respectively. This figure is adapted with permission from ref. [1]

ently and locally within a confined area in the vicinity of the plasmonic nanostructure for LSPs. In contrast, for SPPs, the coherent electron oscillations propagate along with the

'continuous' interface (e.g., metal surfaces) as a longitudinal wave. Most nanoscale plasmonic devices are made of coinage metals like Au and Ag, owing to their ability to meet the dielectric condition for plasmon excitation at their interface with dielectric or air (negative real part and positive imaginary part for the dielectric constant), as well as to support intense surface plasmon resonances (SPR) with resonance spectra overlapping with the visible light spectrum. Recently, metals like aluminum and copper are also widely adopted with better control over the oxide layer formation [43, 44]. The fundamentals of surface plasmon polaritons and localized surface plasmon resonance will be introduced for the rest of this chapter.

2.2 Surface plasmon polaritons

Surface plasmon polaritons (SPPs) are evanescently confined electromagnetic excitations propagating at the interface between a conductor and a dielectric. They are excited in a continuous surface of silver or gold with at least one dimension smaller than the wavelength of light (e.g., smooth, thin films with thicknesses between 10–200 nm). SPPs can generate a moderate field enhancements (10–100 times) in a large spatial range (1000 nm) [45].

In order to investigate the physical properties of SPPs, we start by constructing a propagation geometry (figure 2.2) where waves only propagate in one direction of the interface plane (x-direction of a Cartesian coordinate system). For $z > 0$, there is a dielectric, non-absorbing half space with a real dielectric constant $\varepsilon_2 > 0$. The other side of the interface ($z < 0$) is a conducting half space with a dielectric constant ε_1 that $Re[\varepsilon_1] < 0$. A wave equation for E-field can be defined on this geometry

$$\frac{\partial^2 \mathbf{E}(z)}{\partial z^2} + (k_0^2 \varepsilon - \beta^2)\mathbf{E} = 0 \tag{2.1}$$

where $k_0 = \omega$ is the wave vector of the propagating wave in vacuum, ε is the permittivity of the medium, and $\beta = kx$ is the propagation constant which represents the direction of

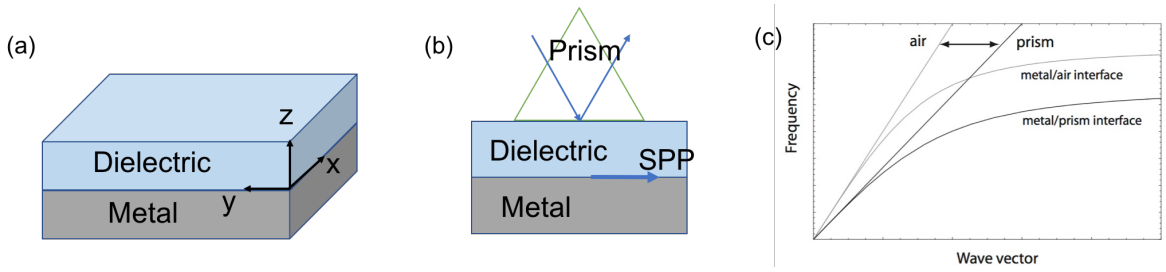

Figure 2.2: **Propagation of SPP.** (a) Geometry for SPP propagation at a single interface between a metal and a dielectric. (b) Prism coupling to SPPs using attenuated total internal reflection in the Otto configuration. (c) Prism coupling and SPP dispersion. Only propagation constants between the light lines of air and the prism (usually glass) are accessible, resulting in additional SPP damping due to leakage radiation into the latter. This figure is adapted with permission from ref. [2]

.

propagation in the wave vector of traveling waves. The wave function for both **E**− and **H**−field can then be broken down into different field components to determine the spatial field profile as well as dispersion relationships. Specifically, for propagation only along the x-direction, we arrive at the following equation set

$$\begin{aligned} \frac{\partial E_y}{\partial z} &= -i\omega\mu_0 H_x \\ \frac{\partial E_x}{\partial z} - i\beta E_z &= i\omega\mu_0 H_y \\ i\beta E_y &= i\omega\mu_0 H_z \\ \frac{\partial H_y}{\partial z} &= i\omega\varepsilon_0\varepsilon E_x \\ \frac{\partial H_x}{\partial z} - i\beta H_z &= -i\omega\varepsilon_0\varepsilon E_y \\ i\beta H_y &= i\omega\varepsilon_0\varepsilon E_z. \end{aligned} \tag{2.2}$$

This system has two solutions, which correspond to two different polarization directions, the transverse magnetic (TM) mode and the transverse electric (TE) mode [2]. For TM modes, only the field components E_x, E_z and H_y are nonzero.

Thus, solution equations for two half spaces are

$$\begin{aligned} H_y(z) &= A_2 e^{i\beta x} e^{-k_2 z} \\ E_x(z) &= i A_2 \frac{1}{\omega \varepsilon_0 \varepsilon_2} k_2 e^{i\beta x} e^{-k_2 z} \\ E_z(z) &= -A_2 \frac{\beta}{\omega \varepsilon_0 \varepsilon_2} e^{i\beta x} e^{-k_2 z} \end{aligned} \tag{2.3}$$

and

$$\begin{aligned} H_y(z) &= A_1 e^{i\beta x} e^{k_1 z} \\ E_x(z) &= -i A_1 \frac{1}{\omega \varepsilon_0 \varepsilon_2} k_1 e^{i\beta x} e^{k_1 z} \\ E_z(z) &= -A_1 \frac{\beta}{\omega \varepsilon_0 \varepsilon_2} e^{i\beta x} e^{k_1 z} \end{aligned} \tag{2.4}$$

for $z > 0$ and $z < 0$, respectively. $k_i (i = 1, 2)$ is the wave vector for each medium that defines the extension of the evanescent field into each medium perpendicularly from the interface and $A_i (i = 1, 2)$ are the same at the interface based on the boundary conditions. Each equation is composed of two parts, (1) the $e^{i\beta x}$ part representing a traveling wave, and (2) the $e^{k_1 z}$ or $e^{k_2 z}$ part representing the evanescent fields that decay moving away from the interface. Based on boundary conditions, we have

$$\begin{aligned} A_1 &= A_2 \\ \frac{k_2}{k_1} &= -\frac{\varepsilon_2}{\varepsilon_1}. \end{aligned} \tag{2.5}$$

To fulfill the wave function for TM modes $\frac{\partial^2 H_y}{\partial z^2} + (k_0^2 \varepsilon - \beta^2) H_y = 0$, we have

$$\begin{aligned} k_1^2 &= \beta^2 - k_0^2 \varepsilon_1 \\ k_2^2 &= \beta^2 - k_0^2 \varepsilon_2. \end{aligned} \tag{2.6}$$

Thus, finally, we can write the dispersion relation of SPPs propagating at the interface shown in figure 2.2 as

$$\beta = k_0 \sqrt{\frac{\varepsilon_1 \varepsilon_2}{\varepsilon_1 + \varepsilon_2}}. \tag{2.7}$$

The frequency-dependent permittivity of the metal (ε_1) and the dielectric material (ε_2) must have opposite signs. In general cases, the momentum of the SPP mode, $\hbar_\beta$ is greater than that of a free-space photon of the same frequency, $\hbar_{k_0}$. This increase in momentum is originated from the binding between SPPs and surfaces. To overcome it, techniques like prism or grating coupling or nanoantennas can be used to couple far-field light into SPPs (figure 2.2). The TE mode solutions are not discusses here since no SPPs exist for TE polarization [2].

After converted into an SPP mode, the intensity of the wave will gradually diminish as it propagates along the flat metal surface due to the absorption in the metal. Based on equation 2.7, the propagation length of SPP (the distance after which the SPP intensity decreases to 1/e of the initial value) can be calculated using

$$\begin{aligned} \delta_{spp} &= \frac{1}{2k_{sppi}} \\ &= \frac{\lambda}{2\pi}\left(\frac{\varepsilon_{mr}+\varepsilon_d}{\varepsilon_{mr}\varepsilon_d}\right)^{\frac{3}{2}}\frac{\varepsilon_{mr}^2}{\varepsilon_{mi}} \end{aligned} \tag{2.8}$$

where k_{sppi} is the imaginary part of the complex SPP wavevector, and ε_{mr} and ε_{mi} are the real and imaginary parts of the dielectric function of the metal. From equation 2.8, we can see that the propagation length is the dielectric constant and excitation light wavelength can have a large effect on the propagation length.

The unique optical properties of SPPs allow them to control light at scales much smaller than the wavelength of light. A variety of potential applications exist for SPPs, such as subwavelength optics (e.g. waveguides [33, 46–48] and sources [36, 49, 50]), near-field optics and spectroscopies [51–53], data storage [54–56], chemical sensors [57–59] and biosensors [60–62]. One recent example is a SPP laser at the deep subwavelength scale 2.3. Oulton and coworkers adopt a 'hybrid plasmonics' approach and put high-gain cadmium sulfide (CdS) nanowires on top of a silver film, separated by a 5-nm gap layer of magnesium fluoride (MgF2) [3]. As a result, the SPP mode areas can be as small as $\frac{\lambda^2}{400}$. Moreover, the plasmonic laser

is physically smaller than conventional lasers, achieves a broadband nanowire spontaneous emission rate enhancement, and maintains considerable optical mode-gain overlap without strong dependence of the mode confinement on the nanowire diameter. Based on this type of deep subwavelength SPP laser, new sources operating among the visible spectrum can be built to generate coherent light far below the diffraction limit.

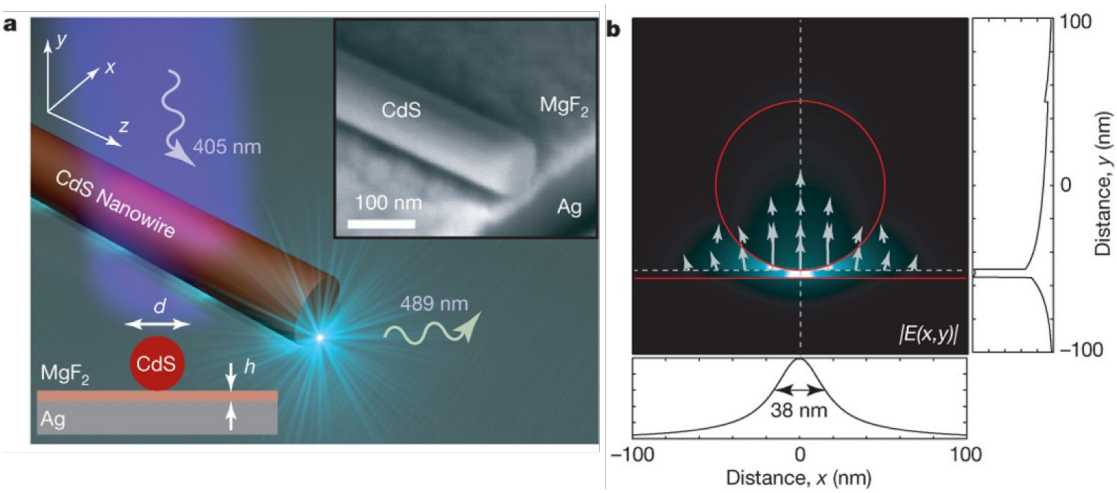

Figure 2.3: **The deep subwavelength plasmonic laser.** (a) The plasmonic laser consists of a CdS semiconductor nanowire on top of a silver substrate, separated by a nanometre-scale MgF_2 layer of thickness h. This hybrid design helps to achieve a novel plasmonic mode with mode size more than 100 times below the diffraction limit. Insert: an image of a typical plamonic laser captured by scanning electron microscope. The sample is sliced in a direction perpendicular to the nanowire's axis. (b) The stimulated electric field distribution and direction $|E(x, y)|$ of a hybrid plasmonic mode at a wavelength of $\lambda = 489nm$, corresponding to the CdS I_2 exciton line. The cross-sectional field plots (along the broken lines in the field map) illustrate the strong overall confinement in the gap region between the nanowire and metal surface with sufficient modal overlap in the semiconductor to facilitate gain. This figure is adapted with permission from ref. [3]

.

2.3 Localized Surface Plasmons

Unlike SPPs, localized surface plasmons (LSPs) are non-propagating excitations of conduction-band electrons of metallic nanostructures with dimensions smaller than the wavelength of light. With the curved surface of the particle, a restoring force is exerted on the driven electrons, allowing resonance to occur, resulting in field amplification. Moreover, one advantage of LSP is that it can be excited by direct light illumination without coupling employment like for SPP excitation [2].

Since the metallic nanostructure has a dimension smaller than the wavelength of light, its interaction with the electromagnetic field can be analyzed using the simple quasi-static approximation. Thus, we can use a simpler model that considers the phase of the harmonically oscillating electromagnetic field to be constant over the particle volume. For instance, for an isotropic, homogeneous sphere with radius $a << \lambda$ which is surrounded by an isotropic, non-absorbing medium with dielectric constant ε_m (figure 2.4), we can assume the static electric field $\mathbf{E} = E_0\hat{x}$. In the electrostatic approach, the electric field $E = \bigtriangledown\phi$ can be calculated based on the solution of the Laplace equation for the potential ($\bigtriangledown^2\phi = 0$). The general solution would be

$$\Phi(r,\theta) = \sum_{l=0}^{\infty}[A_l r^l + B_l r^{-(l+1)}]P_l(cos\theta) \tag{2.9}$$

where $P_l(cos\theta)$ are the Legendre Polynomials of order l, and θ the angle between the position vector and the x-axis.

The equations for the potential Φ inside and outside the sphere can be written as

$$\begin{aligned} \Phi_{in}(r,\theta) &= \sum_{l=0}^{\infty} A_l r^l P_l(cos\theta) \\ \Phi_{out}(r,\theta) &= \sum_{l=0}^{\infty}[B_l r^l + C_l r^{-(l+1)}]P_l(cos\theta) \end{aligned} \tag{2.10}$$

where the coefficients A_l, B_l and C_l can be determined based on the boundary conditions

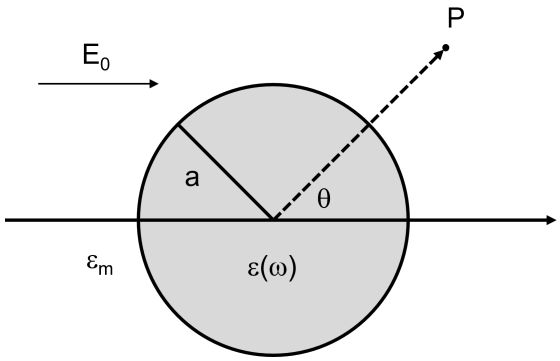

Figure 2.4: **Sketch of homogeneous sub-wavelength spherical particle placed in electrostatic field.** The sphere is homogeneous with a dielectric function $\varepsilon(\omega)$ and radius a. It is positioned in an isotropic, non-absorbing medium with a dielectric constant ε_m. A static electric field **E** is applied.

at $r \to \infty$ and at the sphere surface $r = a$. We can now transform equations 2.10 into

$$\Phi_{in} = \frac{3\varepsilon_m}{\varepsilon + 2\varepsilon_m} E_0 r cos\theta \tag{2.11}$$

$$\Phi_{out} = -E_0 r cos\theta + \frac{\varepsilon - \varepsilon_m}{\varepsilon + 2\varepsilon_m} E_0 a^3 \frac{cos\theta}{r^2} \tag{2.12}$$

where ε and ε_m correspond to the permittivity of the surrounding medium and the dielectric function of the metal sphere, respectively. Equation 2.12 can be described as the addition of the electrostatic field applied at the point (first term) and the field produced by a dipole at the center of the particle (second term)

$$\begin{aligned} \Phi_{out} &= \Phi_{applied} + \Phi_{dipole} \\ &= -E_0 r cos\theta + \frac{\mathbf{p} \cdot \mathbf{r}}{4\pi\varepsilon_0\varepsilon_m r^3} \end{aligned} \tag{2.13}$$

$$\mathbf{p} = \pi\varepsilon_0\varepsilon_m a^3 \frac{\varepsilon - \varepsilon_m}{\varepsilon + 2\varepsilon_m} \mathbf{E} \tag{2.14}$$

where **p** is the induced dipole of the metallic sphere under irradiation proportional to the incident electromagnetic field (E_0). The induced dipole can also be expressed in terms of the polarizability of the metal sphere (α)

$$\mathbf{p} = \varepsilon_0 \varepsilon_m \alpha \mathbf{E_0} \tag{2.15}$$

$$\alpha = 4\pi a^3 \frac{\varepsilon - \varepsilon_m}{\varepsilon + 2\varepsilon_m} \tag{2.16}$$

From equation 2.16, we can see that the as ε approaches $2\varepsilon_m$, the metallic sphere can achieve a resonant enhancement, generating large induced fields. The absorption and scattering efficiency are also consequently enhanced, which can be measured through optical techniques.

LSP can be excited if $Re[\varepsilon]$ is negative and close to $2\varepsilon_m$ while $Im[\varepsilon]$ is positive. The distribution of the induced electromagnetic fields $E = \nabla\phi$ can then be evaluated as

$$\mathbf{E_{in}} = \frac{3\varepsilon_m}{\varepsilon + 2\varepsilon_m} \mathbf{E_0} \tag{2.17}$$

$$\mathbf{E_{out}} = \mathbf{E_0} + \frac{3\mathbf{n}(\mathbf{n} \cdot \mathbf{p})}{4\pi\varepsilon_0\varepsilon_m} \frac{1}{r^3}. \tag{2.18}$$

Here we can understand that the enhanced local field of the plasmonic nanostructure is proportional to $\frac{1}{r^3}$. The resonance in the polarizability implies an enhancement of both the internal and dipolar fields. Most of the notable applications of metal nanoparticles in optical devices and sensors (e.g., plasmon-enhanced molecular spectroscopy (PEMS) and plasmon-mediated chemical reaction (PMCR)) are based on this field-enhancement at the plasmon resonance.

2.4 Relaxation of surface plasmons

After being excited, surface plasmons (SPs) can relax to the ground state through different paths, including radiative paths with photon re-emission and non-radiative paths [63]. Depending on the type of plasmon mode, the population of each electron state is modified

due to incident photons. Afterward, energy redistributions of excited carriers can happen in different timescales determined by different relaxation paths. For example, in the timescale of 1 - 100 fs, after the SPR-assisted photon absorption, the surface plasmons dephase due to the energy exchange between an electromagnetic wave and electron in the plasma, and a hot hole – hot electron pair is created. This process is called the Landau damping effect [64]. During this timescale, the transition from photonic energy to electronic energy happens. The excited electron-hole pair would release the energy through either a photon re-emission electron-electron interaction process. Electron-electron interactions dominate the timescale of 100 fs – 10 ps. The electron energy has a quasi-Fermi–Dirac distribution as excited carriers transfer energy to lower-state electrons (figure 2.5a,c,d). In the timescale of 100 ps – ns, electron-electron interactions switch to electron-photon interactions. The excited electron-hole pair would release heat (thermal energy) during the relaxation (figure 2.5b,e). The electromagnetic field enhancement, charge-carrier excitation, and thermal effect are the three major effects caused by the excitation and relaxation of SPs. Different application favors SP excitation and relaxation behavior happening at different timescales.

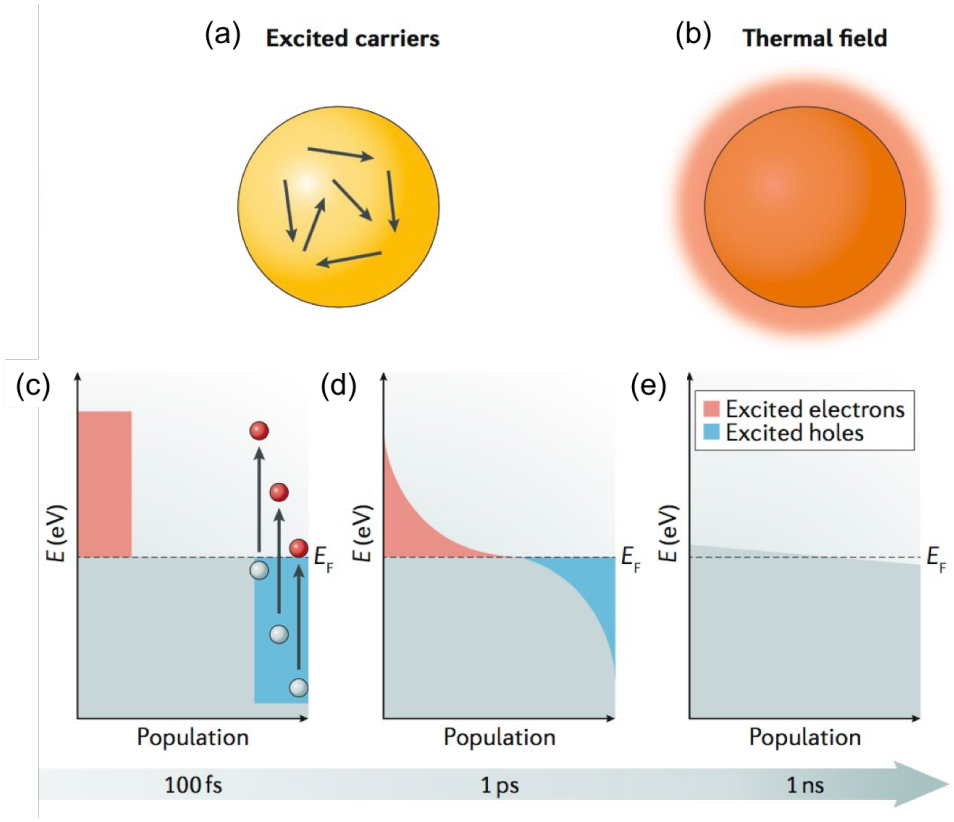

Figure 2.5: **The schematic diagrams of excitation and relaxation of surface plasmons.** Here an example of a SP nanoparticle illuminated by a laser pulse is used. (a) Formation and relaxation of the excited carriers. Incident photons induce changes in the population of the electronic states, which are followed by the energy redistribution of excited carriers over different timescales. The arrows represent electron–electron interactions. (b) The electronic energy converts into thermal energy, which leads to local heating. (c,d) Energy redistribution of the hot carrier. The red areas above the Fermi energy (E_F) represent the distributions of excited electrons, and the blue areas below E_F represent the excited hole distributions. (e) Energy redistribution for thermal release process.

CHAPTER 3

Super-Resolution Fluorescence Imaging

3.1 Overview

Due to its ability to bypass the barrier of the diffraction limit, super-resolution microscopy has been widely recognized for its application for imaging subcellular processes and polymer and metallic dynamics. The spatial resolution of fluorescence microscopy is limited by the diffraction limit of the light, which makes the observation of sub-wavelength structures difficult. This phenomenon can be described as the Abbe diffraction limit

$$d = \frac{\lambda}{2NA} = \frac{\lambda}{2nsin\theta}$$

where d is the smallest distance, the system can distinguish, λ is the wavelength of the emission light, and NA the numerical aperture, which can be re-written by the refraction index of the imaging medium (n) and the half-angle subtended by the optical objective lens (θ). For a typical imaging system, when light passes through an aperture in the objective and is collected at the image plane, it shows as a diffracted pattern (e.g., an Airy disk) instead of an infinitely small point (figure 3.1a,b). The image is a product of observed objects (e.g., emitters) convolved with the system's point spread function (PSF). When two emitters are far apart from each other, they can be identified as two separate Airy disks (figure 3.1e,f). However, when two emitters move closer to a distance where central peaks of two Airy disks overlap and have a distance below the Abbe limit (or Rayleigh limit), it is difficult to distinguish them (figure 3.1c,d).

Over the past decades, super-resolution imaging techniques including stimulated emission depletion microscopy (STED) [65], structure illumination microscopy (SIM) [**?**] photoactivated localization microscopy (PALM) [28] and stochastic optical reconstruction microscopy (STORM) [66] have been developed to push the boundary of the diffraction limit of light microscopy, and have been widely used and providing new insights into fields like cell biology, neurobiology, microbiology, and plasmonic systems [8, 67]. A newer addition to the available array of super-resolution methods is the Super-resolution optical fluctuation imaging (SOFI) method [68, 69]. SOFI is more flexible in terms of photoswitching/blinking requierments allows lower illumination intensities and faster SR information acquisition (but at the expense of a lower resolution enhancement). Also, SOFI does not require special hardware additions and is therefore more affordable than other methods. Details of SOFI methods and a Python implementation of SOFI analysis is presented in chapter 5.

In this chapter, we will discuss how to apply localization-based single-molecule super-resolution techniques to probe plasmonic near-fields. We will start with the mechanisms of fluorescence excitation and emission in general, and how plasmon resonance can enhance fluorescence, then focus on localization-based super-resolution fluorescence techniques to detect the plasmonic near-fields. Current challenges of using this type of techniques will also be discussed.

3.2 Fluorescence

From a quantum mechanical point of view, fluorescence entails a process in which a molecule transitions repeatedly between two quantized energy states (or an electron transitions repeatedly between two atomic orbitals). The transitions after the molecule are photo-excited, and the energy difference between different states are often described using a Jablonski diagram (figure 3.2). All horizontal black lines in this diagram represent all possible energy levels that an electron can occupy and transition in/out, with energy increasing along the vertical

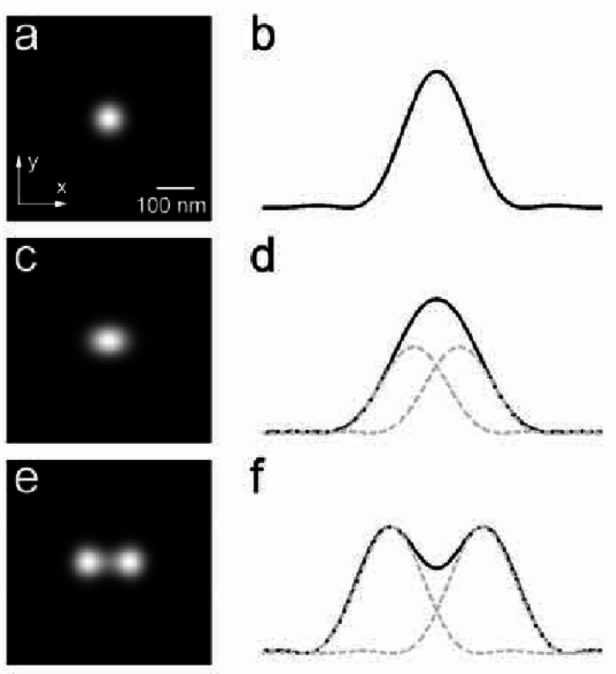

Figure 3.1: **Diffraction limit of classical optical microscopy.** (a) Point spread function (PSF) of a single point source. (b) Intensity cross-section of the Airy disk shown in (a). (c) Image of two overlapping and unresolvable point sources. The point sources are separated by 100 nm, and thus appear as a single, asymmetric peak. (d) Intensity cross-section of the peak shown in (c) along the x -axis. The gray dashed lines represent the separate underlying peaks. Because of the overlap the positions of each point cannot be back-calculated from the image. (e) Image of 2 overlapping point sources separated by around 200 nm. Distinct peaks are beginning to be resolvable. (f) Intensity cross-section along the x -axis of the peaks shown in (e), showing 2 distinct peaks whose positions correspond to the position of the point source.

axis. Only a subset of energy levels is shown in the diagram. As energy increases, vibrational levels become closer together and finally form a continuum. Based on the spin angular momentum configurations, singlet and triplet, ground, and excited states are mapped out in the diagram. Each colored arrow represents a particular transition that can transfer energy between molecular states can be divided into two categories. Solid arrows indicate radiative

transitions with photon interactions (e.g., absorption and emission), while dashes arrows are non-radiative transitions. In a fluorescent system, these repeated transition paths build up the occasions of fluorescent emission, photoblinking, and photobleaching.

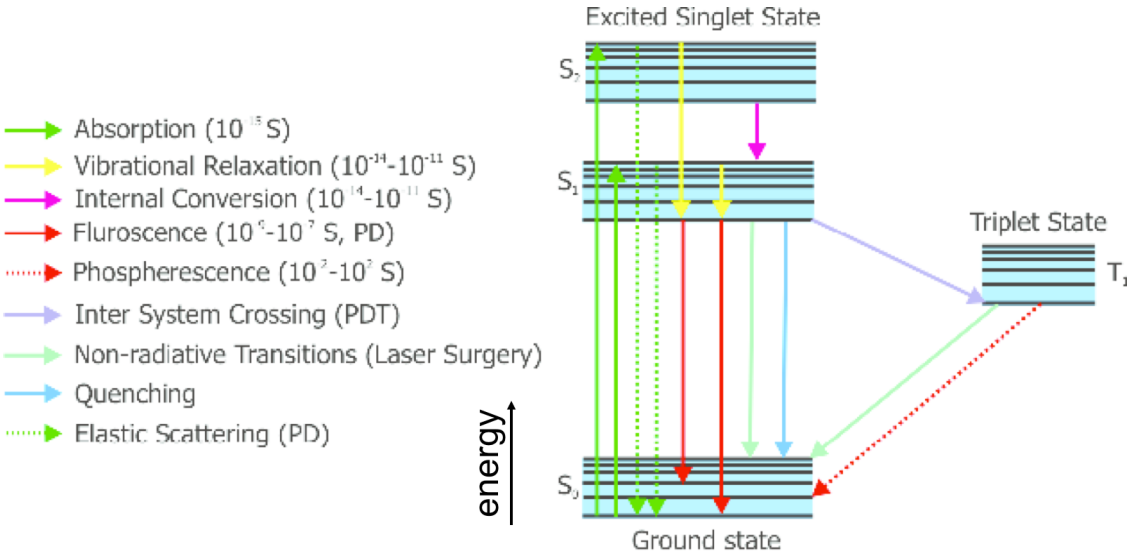

Figure 3.2: **Jablonski energy level diagram.** Some of possible absorption, emission and non-radiative transitions pathways are shown in this example fluorescent system. With this diagram, observed molecule characteristics like fluorescent emission, photoblinking and photobleaching can be explained. This figure is adapted with permission from [4].

Based on the Boltzman distribution, most molecules are populated at the lowest vibrational level of the ground state (S_0) at room temperature. During excitation and de-excitation processes, the delocalized electron cloud over the molecule's framework is perturbed. The perturbations are determined by a combination of (1) the probabilities of energy transitions, as well as (2) selection rules determined by the symmetry of the molecule orbital structures.

Let us look at transitions from left to right in figure 3.2. Upon the absorption of an incident photon of energy $h\mu$, the molecule is excited from the ground state to one of the vibrational levels of the singlet excited states (e.g., S_1, S_2). Due to the conservation of angular momentum, it cannot be excited to any triplet states. Since the molecule is at

a non-equilibrium state after the excitation, it will eventually dissipate the energy. The following transition can be either a radiative process like spontaneous or stimulated emission or non-radiative processes like internal conversion (between two different energy levels) or vibrational relaxation (within a single electronic energy level). Due to these two types of non-radiative internal energy loss, the wavelength of the emitted photon is always longer than the incident photon. Other non-radiative transitions can also happen when the excited molecules relax to the ground state related to either the molecule's intrinsic quantum yield or external quenching influence.

The intrinsic quantum yield (QY) of the radiation, Φ, represents the ratio of the number of photons emitted by the molecule compared to all absorbed photons. Since the decay rate shows the probability that each transition would occur, QY also indicates the probability that an excited molecule goes through radiative decay. Thus, we have

$$\Phi = \frac{\kappa_r}{\kappa_r + \kappa_n r}$$

where κ_r is the radiative rate and $\kappa_n r$ is the non-radiative rate related to the internal loss of the molecule.

This excitation/emission circle can go on indefinitely, generating continuous fluorescence signals, until the molecule undergoes an intersystem crossing process and ends up in a triplet state (T_1). The average triplet state lifetime is defined to be inversely proportional to the singlet-triplet transition probability. The decay (phosphorescence) from the triplet state is much longer than the fluorescent decay due to the forbidden transition between different spin multiplicities. During this time, the excitation/emission fluorescence cycle is broken, and the molecule remains in the 'dark' state. This temporal intermittency of fluorescence is called photoblinking. At some point, a fluorescent molecule becomes permanently dark, which is called a photobleaching process.

3.3 Single-Molecule Localization-Based Fluorescence Microscopy

Each transition mentioned in the previous section occurs at a different probability and along a preferred direction in the molecule's framework known as the transition dipole moment. As a matter of fact, the emission of a fluorescent molecule is comparable to the emission of a dipole and often considered equal, especially for simulation studies [70]. Thus, the amount of light collected is determined by the orientation of the emitter dipole and its alignment with respect to both the electric field of the illumination and the objective collection angle. The rotational motion of molecules changes the emission polarization, which can be detected as fluorescence anisotropy. Besides molecule rotation, other effects like coupling to optical nanoantennas can also introduce fluorescence anisotropy into the system. This will be discussed in detail in the next section and chapter 4.

When molecules are closely labeled, super-resolution imaging techniques are at hand for researchers to distinguish properties of single molecules, including fluorescence anisotropy. With a thorough understanding of how fluorescence anisotropy of molecule is affected by the environment like nearby optical nanoantennas and how to apply super-resolution imaging techniques for this type of study, we can better select and utilize molecules for a wide range of applications.

Besides techniques like STED and SIM, a collection of widefield imaging methods called single-molecule localization microscopy (SMLM), including PALM and STORM, is based on stochastic switching behavior of single-molecule fluorescence signal. PALM and STORM take advantage of the switching property of fluorescent probes. Fluorescent probes like quantum dots, fluorescence proteins, and organic dyes can switch between fluorescent and dark states at different acquisition frames. For each frame, only a subgroup of probes is detected. By careful chemical, physical or optical manipulation, neighboring molecules can be in different states (i.e., "on" and "off") during acquisition, and fluorophores with distances more significant than the diffraction limit can be resolved and localized by a single molecule

localization fitting. Consequently, a final super-resolution image can be reconstructed from the super-positions of all fluorophore locations detected by a stack of frames. The scheme of STORM/PALM is illustrated in figure 3.3.

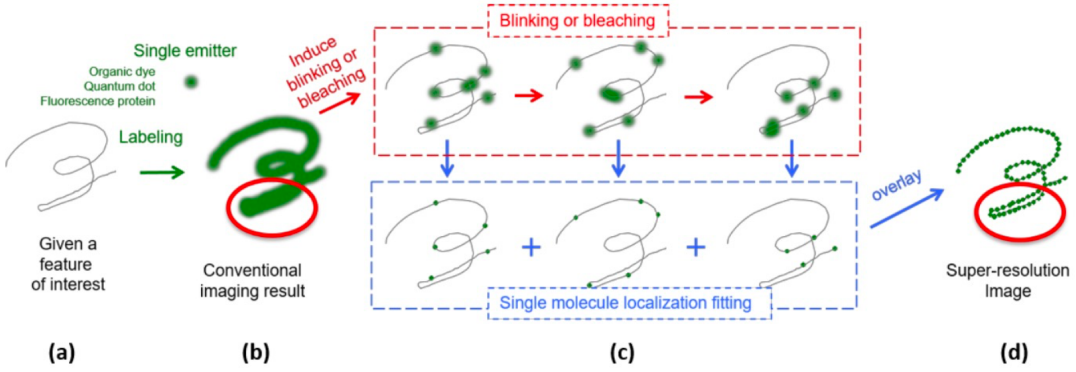

Figure 3.3: **Concept of single-molecule localization microscopy diagram.** The single molecule localization microscopy provides super-resolution capability to resolve feature of interest that is too small to be observed with conventional imaging technique. (a) Given a feature of interest, fluorophores like organic dyes, quantum dots or fluorescent proteins are used as labeling agents. (b) Each fluorophore is imaged as a diffraction spot. Due to the high labeling density, individual fluorophore is not resolvable. (c) Due to induced photoblinking or photobleaching, a small portion of fluorophores are fluorescent and captured at each acquisition. Each single molecule is fitted to a pre-defined function to find the location. (d) All the localization results are super-imposed together to form the final super-resolution imaging. This figure is adapted with permission from [5].

3.4 Plasmon-Enhanced Fluorescence Microscopy

Different effects can be observed when fluorescent molecules are introduced into a plasmonic system. Due to its interaction with the plasmonic structure, various effects can be observed [71]. Specifically, a plasmonic structure can trigger (1) absorption enhancement, (2) emission enhancement, and (3) fluorescence quenching to molecule's optical behaviors.

Absorption enhancement means that, before a saturated state, the molecule's fluorescence increases as the excitation field strength increases. If the field strength continues to increase, the fluorescence enhancement will finally reach a saturation point, after which will be no further absorption enhancement as the local field increases. With a fixed quantum yield, the emission enhancement of the molecule is expected to increase as a function of local field intensity as well. Meanwhile, there is another factor called the Purcell effect that needs to be considered as well, which explains the modification of spontaneous emission affected by the local environment of the molecule [72]. The enhancement of emission is a result of a plasmon's influence on the local density of states (LDOS) in the vicinity to the molecule [6,73,74]. More specifically, as we can see from figure 3.2 when the excited molecule relaxes to the ground state radiatively, the emitted photon enters one of the states available to it. The number of available states (the density of states) depends on the plasmonic structure and the photon's wavelength. The presence of a plasmonic nanostructure nearby has proven to increase the density of states for the emitted photon, providing extra plasmon modes for a photon to reside. This expansion in the density of states raises the probability of photon emission, reducing the excited state's lifetime and the possibility of the molecule's transition to the dark state. In order for this to work effectively, the plasmon resonance and molecule emission wavelength should match. Thus, during the same acquisition duration, molecules in a plasmonic system would appear to have higher quantum yield and are brighter compared to independent molecules [75].

A counter-effect to the absorption and emission enhancement is quenching, which refers

to effects that suppress the fluorescence emission. This could be due to the non-radiative direct energy transfer to the plasmonic structure surface at short distances. As shown in figure 3.4, as the gold nanosphere gets closer to the surface, the fluorescence response of the molecule fixed on the surface first rises then drops dramatically at a distance smaller than a few nanometers.

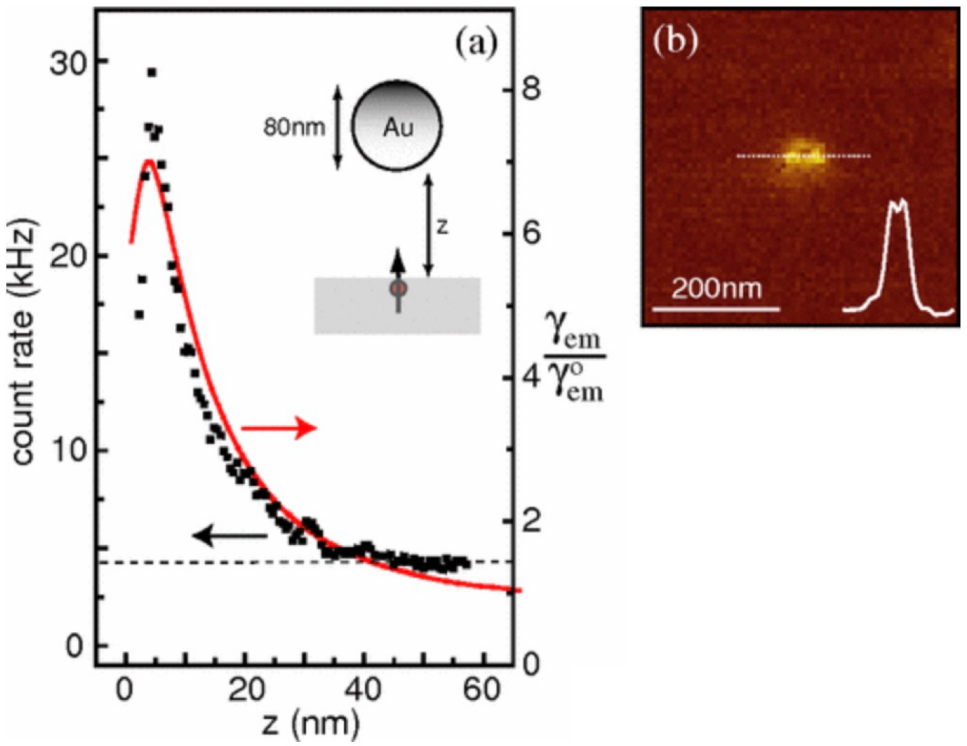

Figure 3.4: **Quenching effect caused by plasmon-molecule interaction.** (a) Change of fluorescence count rate as a function of particle-surface distance z. The molecule is vertically oriented. The experimental (black dots) and simulation (red curve) results are compared. The dashed line represents the background fluorescence level. (b) Fluorescence rate image of the molecule at $z \approx 2nm$. Fluorescence quenching is indicated by the dip in the center of the cross-section plot. This figure is adapted with permission from [6].

The absorption and emission enhancement greatly increase the observed fluorescence signal and benefit multiple applications, including chemical sensing and biosensing. Localization-

based super-resolution imaging techniques have been used to detect the plasmonic near-fields as well. Since the localization precision is inversely proportional to the number of photons collected, the enhancement would assist in mapping the plasmonic near-field with higher precision. Since surface plasmons are notably sensitive to the shape, size, and composition of the nanostructure as well as their surrounding environment, they can perform strong sensing responses for different applications. For instance, LSPR sensing can measure spectral shifts as a function of the local dielectric environment [76–78]. Moreover, a far-field excitation source coupled with plasmonics is a straightforward strategy for achieving sub-diffraction excitation volumes, so plasmonics and super-resolution imaging complement each other naturally well. Additionally, because plasmonic nanostructures usually have nanoscale dimensions, super-resolution imaging techniques are necessary to examine the properties of these structures. However, the physics behind the interaction between the plasmonic nanoantenna and fluorescent particles is not fully understood. Moreover, detrimental problems like quenching effects, emission anisotropy, and mislocalization make it challenging to apply super-resolution imaging techniques (especially localization-based methods) to plasmonics systems. We will discuss these problems in the next section as well as in chapter 4.

3.5 Plasmon-Induced Emitter Mislocalization and Mispolarization

When detecting near-fields of plasmonic nanostructures, emission intensity of fluorophore is usually used as the reporter of the field intensity for reasons mentioned in previous sections. For localization-based super-resolution imaging, the diffraction pattern of the single molecule is then fitted to a defined or calibrated model function to determine the location of the emitter. When imaging a point source of light with a typical optical microscope, the diffraction-limited pattern is an Airy disk, which has a central peak surrounded by a series of circular side bands. This pattern can be further approximated by a 2D Gaussian function

as the model function

$$I(x,y) = I_0 \exp\{-a \times k^2((x-x_0)^2 + (y-y_0)^2)\} + b \tag{3.1}$$

where $I(x,y)$ represents the measured fluorescence intensity across the (x,y) pixels, I_0 is the peak intensity that is proportional to the photon emission rate and acquisition duration, a is the numerical factor that indicates the width of the 2D Gaussian model function, k is the wave number, (x_0, y_0) is the fluorophore's coordinate, and b is the average background intensity per pixel. In a plasmonic system, this model fitting would fail, leading to errors in the calculated emitter positions. This is due to a combination of mechanisms including plamon-fluorophore coupling, image dipole scattering and far-field image super-position, and the effect of each mechanism on the final fitting inaccuracy has not been fully investigated.

As introduced in previous sections, the emission from the fluorophore can couple into plasmon modes of the nanostructure, and the observed fluorescence might originate from not only the fluorophore but also the plasmonic nanostructure. This is illustrated by researchers using different imaging methods. One example is that by looking at the emission from a single-molecule positioned on a silver nanoparticle dimer using polarized surface-enhanced Raman spectroscopy (SERS), the emission appears to be polarized along the long axis of the dimer instead of the molecule orientation (mispolarization), meaning that the plasmonic nanostructure does introduce anisotropy to the emission pattern by generating additional radiation projected to the far-field [79]. This extra radiation would significantly distort the diffraction pattern, and if the 2D Gaussian function is still used for localization, undoubtedly, there would be significant localization error. Another factor that distorts the emission pattern of the molecule is the formation of the image dipole in the plasmonic nanostructure. Specifically, an emitter can be considered a dipole. When it is placed close to the plasmonic nanostructure and excited, it can induce an image dipole, which can be regarded as a secondary fluorescent source 3.5. This additional source would not only create new radiation but also interfere with the radiation from the original dipole (emitter) [7]. De-

pending upon the original dipole orientation and its distance to the plasmonic nanostructure, the interference can be either constructively or destructively (figure 3.5a,b), and can shift the fitted emitter location either closer to or away from the true location (mislocalization) (3.5c,d). The inaccuracy in emitter localization is large enough to be ignored and needs to be characterized and understood in order to get the precise emitter location for near-field mapping.

Curly and co-workers also illustrate the mislocalization and mispolarization phenomenon from the strong light-matter interactions between fluorescent dyes and plasmonic nanostructures [8]. They discover that in addition to being rotated towards the nanorod's dominant surface plasmon mode, the emission polarization distribution also broadened due to both far-field interference and off-resonant coupling between the molecular dipole and the nanorod transverse plasmon mode. They also developed an analytical model to understand this complex interaction, and correct for the mislocalization and mispolarization using least-squares fit (figure 3.6a). Compared to traditional Gaussian fitting (figure 3.6b), this model-based method helps to determine the molecular polarization and location accurately without too much computation cost. This characterization and model development is essential to establish a thorough understanding of molecule-plasmon coupling. In the next chapter, we will discuss our exploration of a more complex plasmonic system and our method to correct mislocalization and mispolarization.

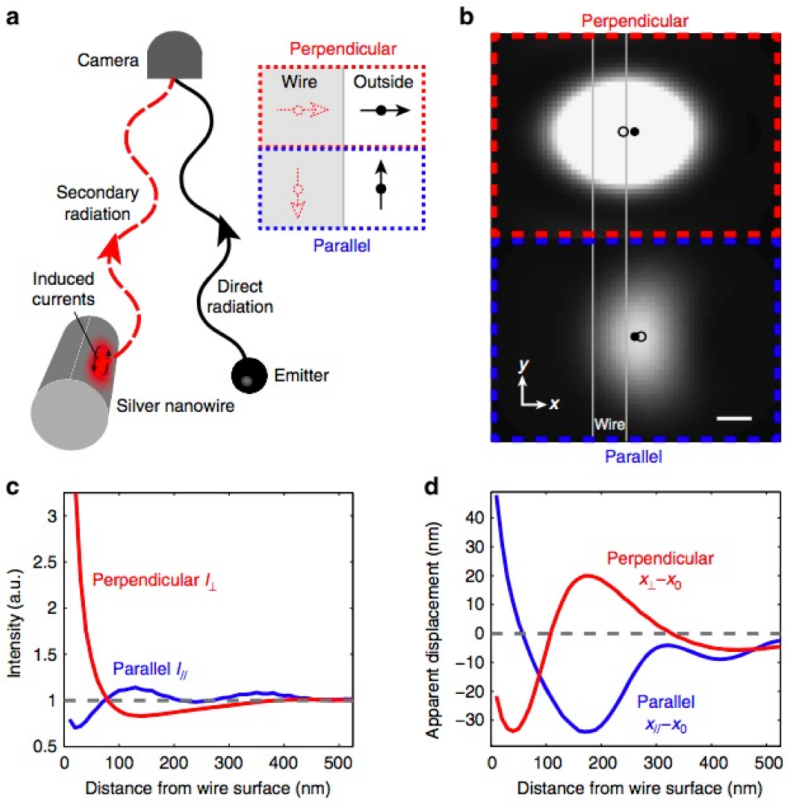

Figure 3.5: **Image-dipole interference.** (a) Illustration of interference between radiation from an emitter and an induced radiation from the silver nanowire. The emitter induces currents in the silver nanowire that radiate into the far field and interfere with the direct emitter radiation. The orientation of the image dipole is determined by the emitter dipole orientation (insert). (b) Calculated far-field diffraction spots from an isotropic emitter next to the silver nanowire with two different dipole orientations (perpendicular and parallel to the nanowire surface). The filled dots are real positions as simulation inputs, and the open dots are fitted positions. Scale bar: 100 nm. (c) Calculated intensity as a function of the distance of an isotropic emitter from the wire surface for the field polarized along two polarization directions. (d) The displacement of the diffraction spot position relative to the emitter position as a function of emitter distance from the wire surface for different emission polarizations. This figure is adapted with permission from [7].

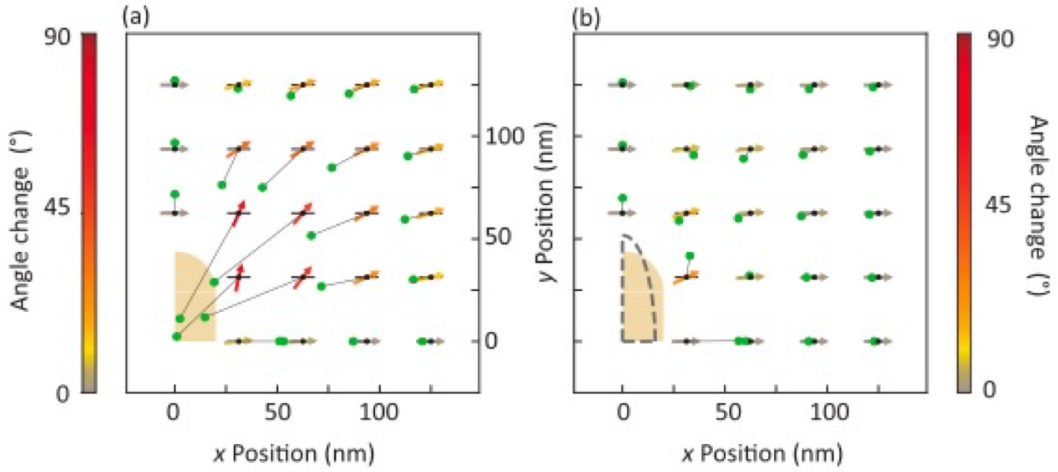

Figure 3.6: **2D Gaussian and analytical model fitting.** Comparison of the best fit results for dipole position (green) and polarization (colored arrows) determined in diffraction-limited images of simulated single-molecule dipoles (black dots) oriented parallel to the x-axis. (a) Gaussian localization of the total intensity paired with molecule orientation as would be determined by polarization-resolved microscopy. (b) Least-squares fit of the model-generated images to simulated images. The Gaussian fitting has more prominent inaccuracy. This figure is adapted with permission from [8].

CHAPTER 4

Super-Resolution imaging of plasmonic Near-fields: Overcoming Emitter Mislocalizations

Plasmonic nano-objects have shown great potential in enhancing biological and chemical sensing, light harvesting and energy transfer, and optical and quantum computing to name a few. Therefore, an extensive effort has been vested in optimizing plasmonic systems and exploiting their field enhancement properties. Super-resolution imaging with quantum dots (QDs) is a promising method to probe plasmonic near-fields, but is hindered by the distortion of the emission intensity and radiation pattern. Here we investigate the interaction between QDs and 'L-shaped' gold nanoantennas, and demonstrate both theoretically and experimentally that this strong interaction can induce polarization-dependent modifications to the apparent QD emission intensity, polarization and localization. Based on FDTD simulations and polarization-modulated single-molecule microscopy, we show that the displacement of the emitter's localization is due to the interference between the emitter and the induced dipole and can be up to 100 nm. We also discovered that the emission polarization can rotate towards the symmetry axis or one arm of the L-shape because of the scattering. Our results could assist in paving a pathway for higher precision plasmonic near-field mapping and its underlying applications.

4.1 Introduction

With the development of plasmonics-based devices, there is a growing need for detecting and characterizing plasmonic effects in extended nanosystems. Due to their ability to concentrate light to a small dimension and create enormous local-field enhancement, nanoscale plasmonic devices have provided novel ways of controlling light and have shown great potential in broad applications, including enhanced chemical sensing [14, 15], bio-sensing [16–18] and high-resolution bioimaging [19, 20]. In addition, integrated nanophotonic circuits combing the plasmonic and optical effects have shown great promise in manipulating optical information [11–13]. Thus, to better control and utilize plasmonic near-field effects, a thorough understanding of the relationship between plasmonic structures and their local fields is crucial for optimizing these devices' performance. Compared to imaging methods like near-field scanning optical microscopy (NSOM) [21–23] or electron energy loss spectroscopy [24, 25], super-resolution imaging has become more popular due to its ability to break the diffraction limit, image under ambient conditions, and provide high throughput imaging [66, 80, 81].

Recent studies have applied super-resolution fluorescent imaging with single emitters (e.g., dyes and quantum dots (QDs)) to probe plasmonic systems. In these studies, emitted fluorescence intensity from the emitter is used as a far-field reporter of the plasmonic near-field intensity [26,27,82,83]. However, due to the strong electromagnetic interaction between emitters and nearby plasmonic nanostructures, this technique is hindered by a complex mechanism. One major factor is the formation of a distorted point spread function (PSF) [84, 85]. Since an accurate super-resolution localization relies heavily on a stable, well-characterized PSF, this distortion introduces error in the field intensity mapping [86–88]. It has been demonstrated that the fitted centroid position moves away from the actual emitter location when the probe emission is coupled to a plasmonic antenna (e.g., nanorods [8], nanowire [7, 29, 89], and Yagi-Uda antennas [90]). This 'mislocalization' phenomenon may be originated from (1) super-position of the molecule emission and scattered radiation from

the plasmonic interface, (2) interference with the induced image dipole, and (3) near-field coupling [7, 85, 87, 91]. These plasmon-induced interactions may also redirect the single-molecule fluorescence polarization (mispolarization) [46, 79, 92, 93]. Moreover, because of effects like fluorescence enhancement and quenching, the intensity of fluorescence can vary non-monotonically with the field intensity, especially when the emitter is too close (¡30 nm) to the nanoantenna [27].

Despite intense interest and research activity, the interaction between nanoantennas and nearby molecules, as well as its influence on emitters' mislocalization and mispolarization, have not been completely understood. In this work, we select quantum dots (QDs) as the probe due to its degenerate excitation and emission dipole moments, and match their emission wavelength to be either on or off the plasmon resonance mode. We show theoretically and experimentally that this strong interaction can induce polarization-dependent changes to both the apparent emission intensity and position. We extend previous studies to plasmonic nanoantennas with more complicated structural features and demonstrate that shifts in the apparent emission localization and polarization are affected by a combination of factors under different conditions (e.g., emitter dipole location and orientation). Moreover, after optical measurements, we add a 'post mortem' scanning electron microscope (SEM) step to unveil the real position of QDs near plasmonic structures, and find out that the mislocalization can be up to 100 nm and mispolarization can be up to 30°. We isolate the effects from nanoantenna's two orthogonal arms and elucidate the mechanisms behind emission localization and polarization modification. We also propose a new sample fabrication method that implements dip-pen nanolithography (DPN) [94] to achieve single-molecule deposition close to nanoantennas with high precision and throughput. Our work can provide a cost-effective, high-accuracy solution for better super-resolved mapping of plasmonics near-fields. It opens doors for optimized and controlled plasmonic devices with great potential in a wide area of applications.

4.2 Results

4.2.1 Tunable Nanoantenna Sample Design

Previously published works developed models on specific structures like nanowires and nanorods, and used simulation results to correct the mislocalization detected in the experiment. To expand on these previous models and on the 'one-dimensional' antenna structures, and in order to gain better understanding on how near-field coupling and far-field interference would afect the degree of QD mislocalization and miapolarization in a more complex (2D) model system, we performed extensive finite domain time difference (FDTD) calculations to determine the ideal antenna structure and for our study (Figure 4.1(a)). With the help of these calculations, we converged to a 2D antenna design of an L-shaped gold nanostructure with a symmetry axis and a sharp corner, which are features that have not been carefully studied as of yet. The emitter at the inner corner of the L-shape can have simultaneous interactions with two arms. In this way, the coupling strength can be tuned by controlling the relative distance of QDs to each of the arm.

Since the scattering from the antenna interface is one significant contribution to the QD image distortion, the relationship between the L-shape dimensions and their optical response is explored. L-shaped nanoantenna with various dimensions exhibit different scattering spectrum (Figure 4.1(c)), and QDs with varying emission wavelengths can be selected to be on- or off-resonance with the plasmon resonance mode. As for our experimental setting, the structure with a configuration of 60 nm height, 250 nm arm length, and 100 nm arm width has a much stronger scattering at 800nm than 600nm, while vice versa for the (H 60nm, L 200nm, W 50nm) configuration. Thus, by tuning the L-shape dimensions and choosing different-size QDs to match/mismatch the plasmon resonance, we can explore the scattering effect on the QD localization accuracy. For instance, 800-nm emission QDs are excited with a wavelength off the plasmon resonance (642 nm) to excite the emitter only and limit the antenna background. In this way, we avoid fluorescence absorption enhancement and isolate

the coupling in QD emission for polarization-modulated studies.

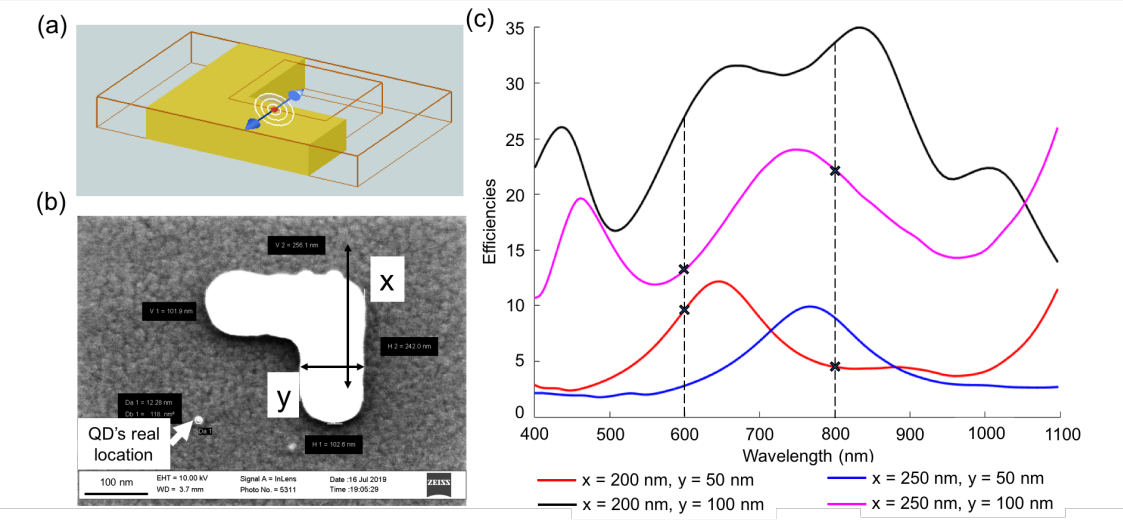

Figure 4.1: **L-shape dimensions and scattering cross-sections.** (a) Design for FDTD simulations with an L-shaped gold nanoantenna and a dipole source positioned nearby. (b) SEM image of the fabricated nanoantenna and QD. QD's real location measured from SEM can be fed-back to the simulation as input. (c) L-shaped Au nanostructures with different dimensions vary in the scattering cross-section at different wavelength. For a nanoantenna with a given dimensions, 800/600 nm emission QDs can be scattered strongly/weakly or weakly/strongly by the designed structure.

To construct a system with plasmonic structures with different dimensions and single-molecule QDs close to them, we employ a two-step lithography method (Figure 4.2). The first step defines the L-shaped plasmonic structure, and the second step sets the QD deposition boundaries. More specifically, nanoantennas with varying dimensions were first patterned onto an indium tin oxide (ITO)-coated glass coverslip with electron beam lithography. This conductive and transparent substrate prepares the sample for both optical and SEM measurements. The second lithographic step defines a pattern that prevents QD from accessing other areas of the coverslip surface, allowing QDs to deposit only near the inner corner of the antenna. Then, a drop of nano-molar QD solution is placed onto the coverslip

to produce a sparse distribution of the probes. QDs can move around the whole substrate surface through Brownian motions, and those that reach the pre-defined area can attach to the surface through chemical functionalization. The carboxylic acid functional group in QD ligands can interact with the ITO surface through a combination of weak electrostatic, hydrogen-bonding, and covalent bonding between the carboxylate and the indium defect sites [95]. By tuning the QD concentration and the area during the second lithographic step, we ensure that an individual unit only has a single plasmonic nanoantenna and a single QD nearby. This single QD and antenna pair is further verified by the SEM image (Figure 4.1(b)). The difference between the dimensions of the fabricated and simulated structures is negligible. However, this sample fabrication method requires precise alignment between two e-beam lithographic steps, making the success rate / yield of fabrication low. We also combine dip-pen nanolithography (DPN) method [94, 96] together with E-beam lithography to directly 'write' single QDs with higher precision (Figure 4.3). Compared to points accumulation for imaging in nanoscale topography (PAINT) methods that have been used for previous research which relies on the absorption and release of freely-diffusing probes at random locations on the sample surface [8], our method immobilizes QDs to sites close to the antenna with selective binding and can be only removed though specific washing steps. Instead of counting on the probe to stay in the field-of-view (FOV) long enough to emit enough photons (especially at low excitation power), we can keep QDs stationary with a well-defined dipole moment orientation throughout the whole acquisition for better PSF fitting and localization with high precision at multiple imaging conditions (e.g., excitation and emission polarization). The inter-antenna spacing is designed to be 5 µm to avoid interactions between plasmonic nanoantennas while keeping a reasonable measurement throughput. For each wide-field imaging run, images from up to 25 pairs of single antenna and QD can be collected. To ensure that emitters at different locations of the FOV share the same excitation intensity and polarization, the optical setup is first calibrated with free QDs at different polarizations. More details about the sample fabrication are provided in

the Methods section.

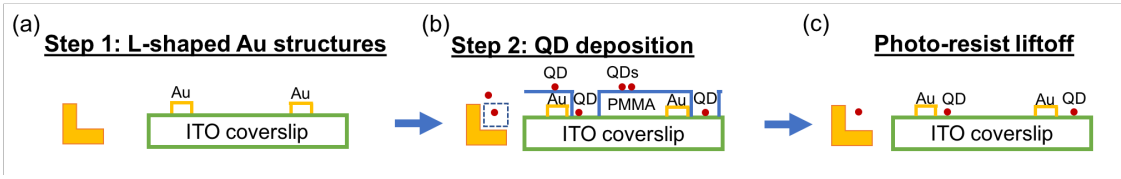

Figure 4.2: **2-step e-beam lithography sample fabrication procedures.** (a) For the first electron beam lithography step, L-shapes with different dimensions are patterned. (b) The pattern of the second lithography layer is aligned to the first layer and is composed of squares that are accessible to QDs. After removing the exposed photoresist, the ITO coverslip was soaked in the diluted QD solution. The carboxyl group in QD ligands can then bind to ITO and stay static on the coverslip surface. (c) The photoresist lift-off step washes the unexposed photoresist off the coverslip, taking away QDs that are not bound to the ITO surface. After rinsing and drying, the sample is ready for optical measurements.

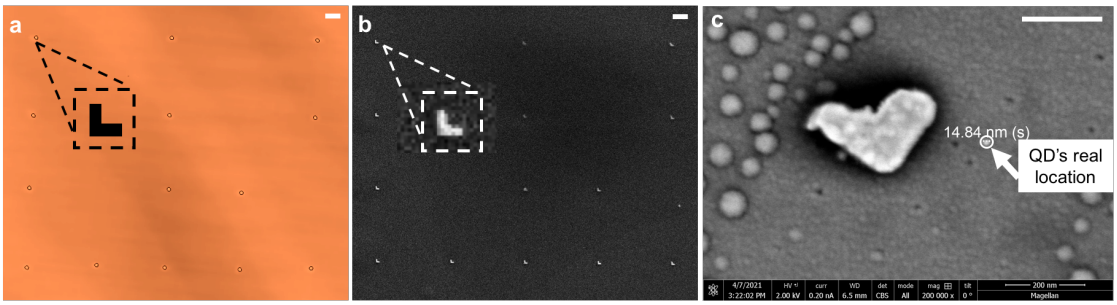

Figure 4.3: **Single-molecule (SM) QD deposition using DPN.** (a) DPN printing spots indicated by brown circles. (b) L-shaped gold nanostructures under SEM. The pattern imaged with DPN tip and SEM matches. (c) Zoom-in of one L-shape with SM QD nearby. DPN first scan through the target area to determine the printing pattern. Then, the tip is inked and move to the start point with careful alignment. The ink with QDs is carried and printed by the tip (red circles in (a)) at locations determined by the first scan. The same target area is later moved under SEM (b), to quantify the relative positions of QDs and nanostructures (c). Scale bar: 200 nm.

4.2.2 Polarization-Resolved Single-Molecule Localization-Based Microscopy

This section describes the experimental approach that controls and studies the interaction between the single-molecule emitter and the plasmonic antenna with super-resolution. We focus on three strategies to modulate and analyze the coupling between the fluorescent emitter and plasmonic nanoantenna: (i) modulate the polarization of the wide-field excitation laser; (ii) analyze the polarization of the QD emission pattern in the far-field; (iii) tune QD emission spectrum to be on- or off-plasmon resonance. As shown in Figure 4.4(a), the modulation approach (i) is achieved by adding a polarizer in the excitation pathway and (ii) by adding an analyzer in the emission pathway of the wide-field fluorescence microscopy. Both the polarizer and analyzer are mounted on rotating stages (Figure 4.4(b)). As the polarizer/analyzer rotates, the far-field images of QDs are acquired at different excitation and emission polarization combinations. The excitation is filtered out, and the emission fluorescence is collected. No noticeable sample drift was observed during the measurement duration.

For a QD without plasmonic structures nearby, the fluorescence emission increases linearly with the excitation up to around half of the saturation intensity [26]. However, depending on the spectral overlap of the QD emission and plasmon resonance, the intensity of fluorescence emitted from the QD-plasmon system is no longer linear with the excitation and strongly affected by whether the QD emission is on-resonance or off-resonance with the plasmon resonance mode [67]. More specifically, previous research has shown that, based on the emitter's location and emission spectra, the coupling strength between the emitter and the antenna fluctuates, causing shifts in the fitted location of the emitter [67]. As for the modulation approach (iii), we start with CdSe/ZnS QDs with an emission peak at around 800 nm. The results shown in the rest of this manuscript are generated based on this experimental setting, and QDs with an off-resonance emission or dual emissions like Mn^{+}-doped CdS QDs with simultaneous on- and off-resonance emissions can be used to further investigate the effect of spectral overlap on the amount of emission coupled into the far-field via

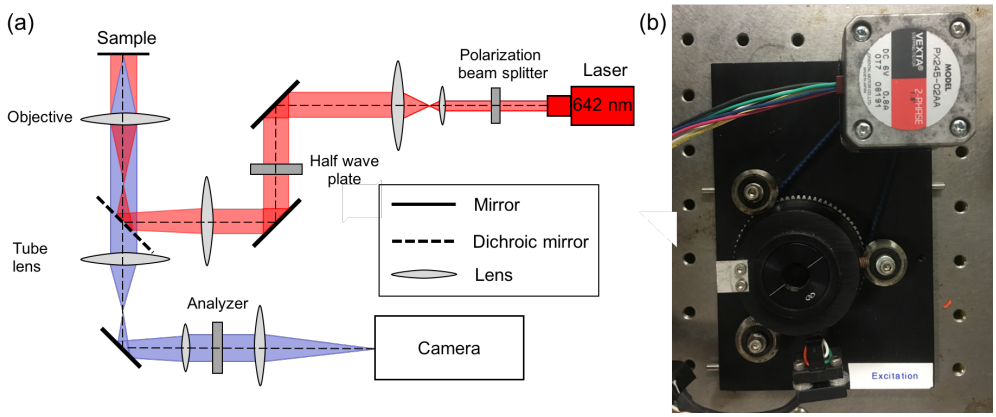

Figure 4.4: **Set-up for polarization-modulated super-resolution fluorescence imaging.** (a) Schematic diagram of the optical setup used for QD localization with excitation / emission polarization modulation. The half-wave plate in the excitation path works as a polarizer that rotates and controls the excitation polarization. The analyzer, on the other hand, selects a specific emission polarization. Both the polarizer and the analyzer are mounted on a rotating stage with 0.5° precision and controlled by the microcontroller Arduino. The stages are rotated between the optical measurements, and QD image at different excitation/emission polarization combinations are recorded. (b) The polarizer mounted on the rotating stage.

the plasmonic antenna and the shift in emitter localization.

For the polarization modulation experiment, we adopt a two-step measurement: (1) a measurement to index the apparent location of QDs together with extraction of local near-field intensity without the polarizer and analyzer, followed by (2) measurements with a modulated linearly polarized light at several different polarization angles. The imaging system with excitation only, emission only, and both polarization modulations together are first calibrated and characterized with sparsely spin-coated 800-nm emission QDs. Measurements are carried out on individual unit composed of one antenna and one QD with the polarizer and the analyzer rotate separately from 0° to 360° and stop every 45°. For each excitation and emission polarization combination, a wide-field fluorescence image is captured, gener-

ating 81 images in total for one full circle rotation (Figure 4.5). Afterwards, the centroid position of each diffraction spot is determined. There are multiple methods for extracting the centroid position of the probe. One recently introduced is using a basis of HermiteGaussian functions as a PSF model to fit abnormal, multilobed PSFs generated from a system with dye labels close to plasmonic nanowires [89]. Here, the multilobed PSF is not observed in our QD-antenna system. Instead, we start with a typical 2D Gaussian function to fit the far-field image, and apply the maximum likelihood estimation method (MLEM) to optimize this PSF to give us the best fit, returning an estimation of QD's apparent position [97]. Even though the degree of final localization precision is heavily dependent upon the number of photons collected and the fluorescence background level of the image, this fitting method has shown overall good performance for localizing QDs (or other emitting probes) in free space for both simulation and experimental results.

When the emission is coupled into a plasmonic antenna, it is re-directed and re-radiated into the far-field compared to the radiation from the emitter alone. Due to the strong electromagnetic coupling of the emitter to the nearby plasmonic structure, the far-field radiation pattern of the emitter will be distorted, introducing imprecision to the localization of single emitters during this fitting step. The final QD far-field images are affected by a combination of interactions, like scattering from the nanostructure surface, dielectric distortion of the emission, and Young's interference effect between the emitter and the image dipole [7, 29]. Thus, modulation and characterization of electromagnetic coupling strength between QDs and nearby metallic structures is crucial to understand and counteract mislocalization of QDs.

4.2.3 Mislocalization of QDs close to plasmonic structures

The fitted QD centers at different polarization combinations are compared to the center determined using the sum image of all polarizer and the analyzer polarization combinations. The spatial displacement is calculated as the difference between the two centers. The rotation

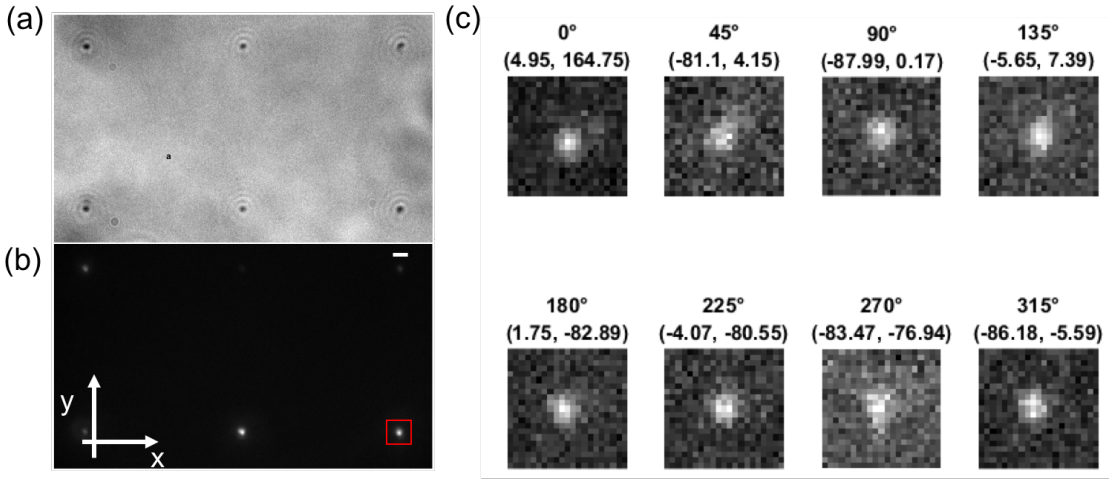

Figure 4.5: **QD images at different emission polarization.** (a) Bright-field image of nanostructure + QD. Since the size of the structure is below the diffraction limit, only the scattering light can be imaged without details of the structure. (b) Fluorescence image of QDs close to plasmonic structures. Different QD brightness may come from different coupling strength between the QD and the structure. Scale bar: 1 m. (c) Images of single-molecule QD with different analyzer polarizations and displacements (labeled at the top of each figure, displacements in nm unit). Since QDs have degenerate excitation dipoles moments, changing the excitation polarization on "free" QDs would not affect the image. With the changing emission polarization, the center of the QD images shift.

of the polarizer in the excitation path does not show impact on the emitter displacement since QDs have degenerate excitation dipoles. This result verifies the result discussed in [89] that the excitation polarization does not affect the PSF distortion. However, as the analyzer rotates, we observe clear shifts in apparent QD center positions (mislocalizations) at different emission polarization. As shown in Figure 4.6(a), displacement of the emitter in x (parallel) and y (perpendicular to the bottom arm of the L-shape) directions are plotted over one full circle of the analyzer rotation. To compensate for the discrepancy of photoblinking behaviors captured at different polarizations and its effect on the imaged fluorescence intensity, the final plot is the average over four full circles of the polarizer rotation. Photbleaching of QDs was

negligible, and the few cases where it did occur were omitted from the analysis pipeline. As expected, the shift of the emitter center positions in both x and y directions is periodic and repeats every 180° of the analyzer rotation (Figure 4.6). As the analyzer rotates, the shifts in the x- and y-axis vary and can be larger than 100 nm. After the optical measurement, the distance between the inner corner of the L-shaped nanoantenna and the QD for each unit is measured using SEM with the help of indexing markers patterned during the sample fabrication. This distance is regarded as the ground truth for the emitter's location and can be further used as the position of dipole source for the simulations (Figure 4.6(b)).

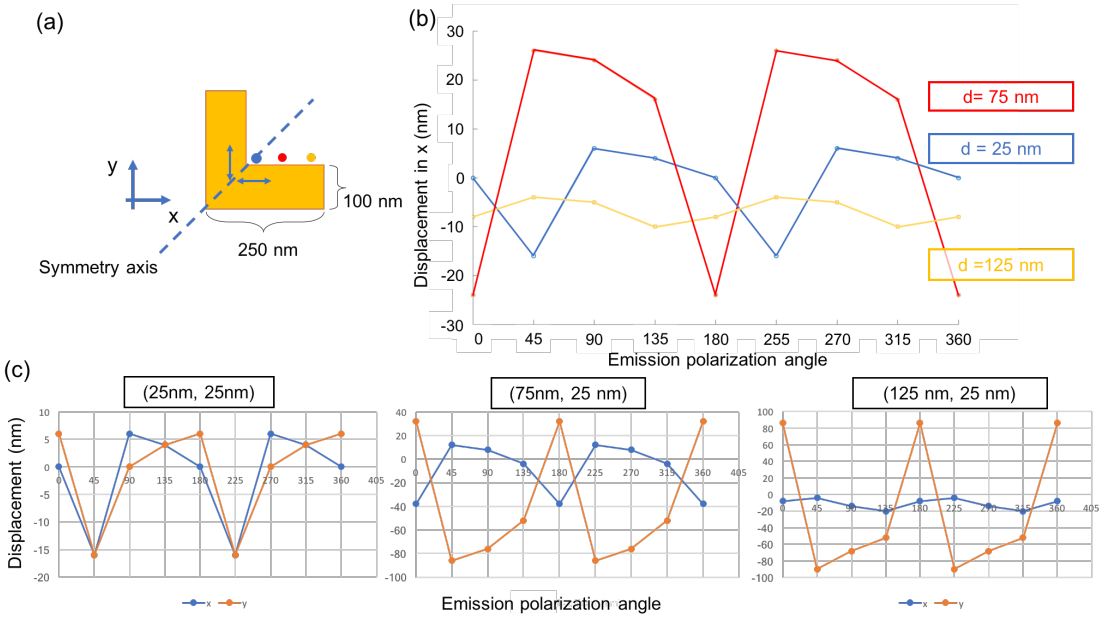

Figure 4.6: **Pattern matching to determine emitter's position.** Simulated (a) and experimentally measured (b) displacement are matched and the difference in the center location is the value of mislocalization. The change of mislocalization shares the same pattern as the simulation result. Based on the magnitude and direction of the displacement, the plots from the experiment can be compared with plots in the simulation collection, and patterns are matched using a least-squares model fit.

Next, a large set of FDTD simulations were performed to generate far-field images with

different conditions for both on- and off-resonance emitters close to metallic systems. Based on the mislocalization trend as the emitter moves away from the inner corner of the antenna (Figure 4.7(a-b)), a simple qualitative model can be adopted to understand the interaction between the emitter and the plasmonic antenna. In addition, this model can also be used to determine how the interaction strength can influence the level of mislocalization for emitters at different locations. For an L-shaped nanoantenna and QDs with on-resonance emission, the displacements are determined by superposition of dipole signals. Specifically, the system can be modeled as one quantum dot, which can be considered as a single dipole, interacting with two induced dipoles, each from one arm of the L-shape metallic structure. The observed far-field image is formed by the superposition and interference of radiation from the three dipoles in total. The left arm mainly changes the displacement in the x-direction (perpendicular to the left arm), while the bottom arm changes the displacement in the y-direction. Compared to other one-dimensional structures studied in previous works, one significant difference for this system is that the emitter is coupled at two directions simultaneously with different coupling strengths. When the emitter is located on the symmetry axis of the L-shape, the interactions with the two arms are identical, and the displacements in the x- and y-directions are very similar Figure 4.7(c)). As the emitter moves asymmetrically away from one arm (for example, the left arm), the displacement range in the x-direction would first increase and then decrease. For the specific position shown in Figure 4.7(c), when the emitter is away from the left arm (125 nm), its interaction with the left dipole is minimal so that its displacement in the x-direction is less than 20 nm. At the same time, its emission is still coupled to the bottom arm, making the maximum displacement in the y-direction to be almost 90nm. Meanwhile, the oscillation of displacement as the emitter moving away from one arm shows that besides the superposition of radiation from multiple dipoles, interference between them also plays an essential role in determining the final displacement. Depending on the relative phases between three dipoles, a constructive/destructive interference may move the fitted center closer to/further away from the interface [7]. For instance, if the dipole

(QD) is orientated parallel to the L-shape bottom arm, it interferes constructively with the induced dipole in the left arm and destructively with the one in the bottom arm. Thus, the mislocalization in the x-direction (0° emission polarization angle) fluctuates but stays negative for the measured distance range, which shares similar patterns as in Ref. [7]. Depending on how the QD is located and oriented in relation to the arm orientation, constructive or destructive interference may prevail.

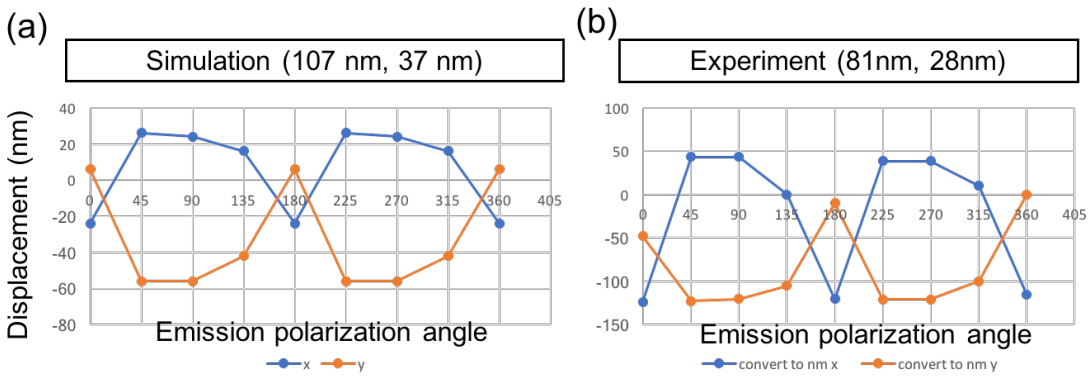

Figure 4.7: **Calculated displacement for emitters at different distance to the L-shaped nanoantennna.** (a) Cartoon demonstrating emitters at different locations that interact with two induced dipoles, each from one arm of the L-shape. The displacement in the x-direction for QDs positioned 25, 75 and 125 nm away from the left arm are plotted in (b). The colors of emitters correspond to plot colors. (c) Simulated mislocalizations of single-molecule QDs positioned at the inner corner with different distances to the L-shape. As the analyzer rotates from 0 to 360, the shifts in x and y axis vary, and can be as large as 100 nm. The displacement is caused mainly by the super-position of the radiations from one original dipole plus two induced dipoles, as well as the interference between the radiations. Emitter at 75 nm has the most notable fluctuation and the greatest absolute displacement. When the emitter too close (25 nm), besides super-position, destructively interference reduces the displacement in the x-direction. When it is far away from the interface, the displacement decays.

Ideally, if the simulation and experimental settings are matched, the magnitude of the polarization-dependent PSF distortion and emitter displacement can be mapped out around the plasmonic nanoantenna. This mapping can be utilized to help deduce the actual emitter position from the distorted PSF by measuring the relative shifts. Meanwhile, the experimental results can be further fed back to simulations in order to improve the predictive power. In the end, the SEM step can be abandoned, and the real emitter position can be obtained purely from matching the experimental and simulation displacement plots. However, the sample preparation method requires high alignment precision between two lithography steps, and has proven to be challenging with respect to closing the loop of (1) nanostructures fabricated with designed dimensions, (2) QDs are positioned close to nanostructures, (3) QDs stay fluorescent during the optical measurement, and (4) real locations of QDs are accessible using SEM. Currently, the 'post mortem' step with SEM to find the real position of the emitter has not been successful, so we are not able to include the actual position of the emitter in iterations that 'close the loop'. Instead, we generate a library of simulated images and plots, and match the displacement pattern from the experiment to the simulation result using a least-squares model fit (Figure 4.6). The dipole source position input from the simulation is then used as the 'real' position of the emitter when we see the change of displacement share the same pattern. A proposal for an alternative method for sample preparation using dip-pen nanolithography (DPN) is presented in the discussion section below.

4.2.4 Detection of Plasmon-Induced Emission Polarization Rotation

In addition to the substantial modification that QD-antenna interaction has on apparent QD localizations, we found that QD-nanoantenna interaction also strongly influences the polarization of the emitted light from this system (mispolarization). Previous studies have reported that the fluorescence emission rate and polarization can be re-directed depending on the design of the antenna (e.g., Yagi-Uda antenna or nanorod) [8, 90]. The discussion below focuses on a more complex antenna shape, L-shape, and explores the change in polarization

that results from plasmon-coupled emission. By measuring the emission polarization of a single-molecule QD coupled to an individual plasmonic nanoantenna, we reveal that QD's emission polarization can be significantly rotated depending on the emitter's position. Far-filed images for QDs with different dipole orientations and emission wavelengths at various positions next to the antenna (H 60 nm, L 200 nm, W 50 nm) are calculated using the same simulation settings as described in previous sections. To quantify the rotation of the emission polarization, we define the apparent emission polarization (θ_{app}) of each emitter by comparing the total intensity of images collected at two perpendicular directions:

$$\theta_{app} = \arctan \sqrt{\frac{I_{\updownarrow}}{I_{\leftrightarrow}}} \tag{4.1}$$

where $I_{\leftrightarrow}$ and $I_{\updownarrow}$ are intensities collected at directions parallel and perpendicular to the bottom arm of the L-shape, respectively. The bottom arm and left arm are aligned to the x-axis and y-axis of a Cartesian coordinate system, respectively. Intensities are always positive and the arctangent function maps the apparent emission polarization into the first quadrant (0° - 90°). The 2D projection of the emission polarization at the image plane can be collected with a polarization-resolved optical set-up shown in the previous section. Theoretically, a free single-molecule QD at the image plane can be considered as a dipole source, whose emission polarization is determined solely by its dipole orientation. However, when interacting with the plasmonic antenna nearby, a combination of near-field coupling, superposition, and interference with the nanoantenna far-field emission would introduce mislocalization and mispolarization, which hinders us from abstracting the actual plasmonic near-field intensity [7, 29, 85–87, 91]. Moreover, when a high numerical-aperture (NA) objective lens is used during image acquisitions, it has been reported that the cross-talk between different polarization channels would deviate the calculated θ_{app} [8]. This issue can be resolved by calibrating the imaging system using a control sample with free QDs randomly positioned on the coverslip for simulations or experiments. In this way, the relationship between the expected and the calculated θ_{app} can be mapped and used to correct the measurements.

Since the L-shape metallic structure can be considered as two nanorods symmetrical

connected, the rotation of the apparent polarization angle is dependent on the position and orientation of the emitter with respect to the symmetry axis. Table 1 shows a compilation of the calculated mispolarization of 800-nm emission QDs under different conditions. The large rotation for 0° and 90°-oriented dipoles is mainly contributed by the superposition of the induced localized surface plasmons (LSPs) modes. Radiation from the bottom arm increases $I_{\leftrightarrow}$, while that from the left arm increases $I_{\updownarrow}$. If the scattered radiation intensities from two arms are equal, the detected apparent emission polarization is expected to be 45. For instance, for emitters positioned on the symmetry axis (e.g., (25 nm, 25nm) away from the inner corner of the L-shape, the interaction between the emitter and two arms is equal. Therefore, both 0 and 90-oriented dipoles are rotated towards 45° while keeping 45° dipole orientation unchanged (Table 4.9 and Figure 4.8(a)). The degree of rotation for 0° and 90°-orientations is symmetrical as expected. As the emitter moving away from both arms along the symmetry axis ((75, 75 nm)), the induced radiation from both arms decreases, causing less rotation of the detected θ_{app} towards 45. When the emitter is off the symmetry axis, depending on its distance to two arms, all three dipole orientations are 'mispolarized'. When QD moves away from the left arm (e.g., (75, 25 nm) and (125, 25 nm)), the interaction between them decreases. A higher $I_{\leftrightarrow}$ of the image is due to more dominant emission from the bottom arm. In this regard, θ_{app} rotates more towards 0° for both 0° and 90° dipole orientations. The total signal intensity collected at the 90° dipole orientation is also much higher (2x) than at 0°. Conversely, for QDs further away from the bottom arm, θ_{app} is closer to 90° because of the superposition of the induced LSP emission at the left arm with the QD emission.

The similarity between the θ_{app} and the antenna scattering spectrum further verifies our hypothesis. In Figure 4.8(a), the relationships between θ_{app} and emission wavelength of the emitter positioned at (25, 25 nm) are plotted for three different dipole orientations. Theoretically, since the emitter is positioned on the symmetry axis, it has identical types of interaction with both arms. Thus, the 0°- and 90°-oriented dipoles are mispolarized towards

the symmetry axis while 45°-oriented keeps unchanged as demonstrated. The greatest rotation is achieved at around the plasmon resonance peak, meaning that the on-resonance emission has a stronger scattering from both interfaces, rotating the apparent emission polarization more towards 45°. However, the difference between the spectrum of θ_{app} and scattering efficiency (Figure 4.8(b)) like double peaks and peak center shift indicates that even though the scattering plays a major role in the mispolarization, there exist other factors that determines the final degree of rotation (e.g., interference between the QD and induced dipole emission). The two spectra diverge after around 800 nm, meaning that the same theoretical explanation might not be applicable for the infrared region. More investigation is needed to characterize other possible mechanisms.

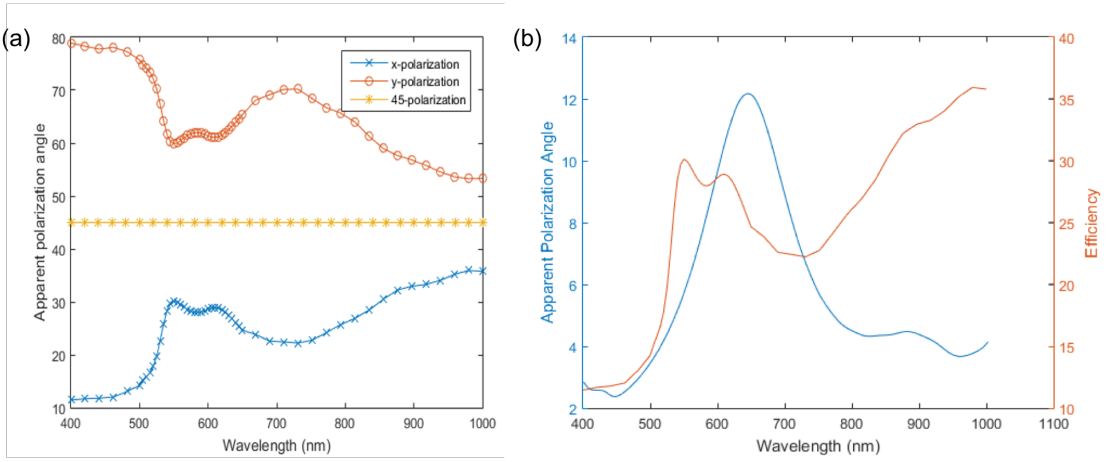

Figure 4.8: **Plasmon-induced rotation of the QD emission polarization.** (a) Calculated spectrum of rotation of apparent polarization angle for QD positioned at the inner corner with distance (25 nm, 25 nm) to the L-shape (L 200 nm, W 50 nm). For emitter positioned on the symmetry axis, since its interaction with two arms are identical, the apparent polarization is expected to rotate towards the axis direction. (b) Comparison of the θ_{app} (for the x-direction) and plasmon resonance spectrum. The polarization angle spectrum shares similar pattern as the scattering cross-section under 800 nm, meaning that the scattering from the interfaces of two arms play an essential role in polarization rotation within the visible light spectrum.

Position (nm) / Dipole orientation (°)	(25, 25)	(75, 75)	(75, 25)	(125, 25)	(25, 75)	w/o antenna
0	24.97	15.75	16.17	6.26	26.09	5.74
45	45.00	45.00	49.26	52.19	40.74	45.00
90	60.71	74.25	63.90	61.56	73.83	84.26

Figure 4.9: **Mispolarization table.** Calculated apparent emission polarization for different dipole orientations.

4.3 Conclusion

In summary, we have demonstrated that the near-field interaction between a plasmonic structure and a nearby emitter is dependent on the emitter's relative position, emission polarization, and emission wavelength and can induce significant mislocalization and mispolarization during emitter's far-field detection and analysis. By isolating effects from the L-shaped nanoantenna's two arms at two orthogonal polarization directions, our study elucidates the mechanisms underlying modification of far-field emission polarization and localization in a QD-antenna system. Notably, we have confirmed that the strong interaction between the emitter and the nanoscale plasmonic structure can introduce substantial error to emitter localization. The apparent emission polarization can also measure the interaction strength. The emission polarization rotates towards the symmetry axis when the emitter is located on the axis. Depending on which arm is closer to the emitter, the emission polarization rotates towards either the left or bottom arm of L-shape. By employing FDTD simulations and a polarization-resolved single-molecule localization-based method, we have revealed that the displacement of the emitter's localization originates mainly from the interference between the emitter and induced dipole emissions. In contrast, the superposition of the emitter and scattered radiation plays a more critical role in the emission polarization rotation. Even though we focused on a specific example, a similar analysis pipeline can be applied to study

a more complex system (e.g., a metallic or dielectric nanoantenna whose shape contains sharp and rounded corners).

This topic can be further extended both in theory and application. In theory, an analytical model to quantitatively understand this QD-antenna system can be constructed and used to predict the true plasmonic near-fields. The effect of near-field coupling, far-field superposition, and interference can be implemented into the model and correct for the mislocalization and mispolarization. This model would provide a practical method that benefits many applications that rely on measuring field strengths with high precision, ranging from biology to high-speed integrated circuits to optical quantum computing. As for application, more simulated and polarization-modulated fluorescence images can be collected using other plasmonic structures, which help connect the emitter mislocalization at different emission polarizations to the shape of the plasmonic nanoantenna and emitter's distance to it. This information can be fed to a machine learning model (e.g., a convolutional neural network, CNN) to solve the inverse problem of predicting the plasmonic structure based on the far-field images. The L-shape will be one of the base structures for the model, and together with other base structures like nanowires and nanodisks, the whole contour of the structure can be determined by combining base structures.

4.4 Methods

4.4.1 FDTD simulation and QD image generation

The Finite-difference time-domain (FDTD) technique is a widely-used method that calculates grid-based electric and magnetic fields using Maxwell's equations. By making an approximation for the time derivative component of Maxwell's equations, FDTD provides a way to model complex periodic structures. More specifically, in FDTD, all the derivatives in Ampere's and Faraday's laws are replaced with finite differences, and space and time are discretized. The future fields in a finite step of time ($\triangle t$) can be calculated based on a set

of updating equations which express them by known past fields. Maxwell's equations are solved iteratively between magnetic and electric fields for every Yee grid point that contains material-related information [98]. For each unit cell in the Yee lattice, an $\hat{E}$ component is positioned at the center, surrounded by $\hat{H}$ components so that each $\hat{E}$ is located midway between a pair of $\hat{H}$ components (e.g., $\hat{E_z}$ (normal to the faces of the plane) is in the midway between $\hat{H_x}$ and $\hat{H_y}$ (the edges of the plane)). Then, the leap-frog approach is applied to solve for the partial spatial derivatives [98]. Here assigning correct permittivity and permeability to each electric and magnetic field component is crucial to map precise electromagnetic wave interaction structures.

In this work, FDTD simulations were performed using a free and open-source software package called Meep. Two types of simulations are carried out: (a) spectrum of scattering and absorption cross-sections of L-shaped nanoantennas using direct plane wave illuminations, and (b) electromagnetic near-field mapping of the QD-antenna system and image generation with a far-field projection. For all calculations, we assumed a background refractive index of 1 to mimic the dry sample condition in air. A glass substrate layer with a refraction index equal to 1.52 is positioned below the plasmonic nanoantenna. The dielectric function of gold was obtained from Johnson and Christy [99].

For (a), the L-shaped plasmonic antennas with different dimensions (60 nm height, 250 nm or 200 nm arm length, 100 nm or 50 nm arm width) are positioned on a glass substrate and illuminated by a spectrally broad light source that spans between 400 nm and 1000 nm. The light source is the super-position of total-field scattered-field" light sources with three different polarizations, and the responses are added together to create the final spectrum. The spectral response of the antenna, including scattering, absorption and excitation cross-sections, of the antenna are collected and calculated through the corresponding monitor, separately 4.10. More specifically, the scattering monitor is located outside of the light source 'box' and collects only light scattered by the antenna, while the absorption monitor is inside the box and collects both illumination and scattering. The negative power transferred

though the monitor is the absorption of the antenna.

For (b), we consider QDs as dipole sources and simulated the radiation patterns of dipoles oriented perpendicular and parallel with respect to each arm of the L-shape and along the symmetry axis. To match or mismatch with the plasmon resonance peak, dipole source with either a 600 nm or 800 nm emission are positioned close to the inner corner of the nanoantenna. A full range of QD distances to the L-shape inner corner and L-shape with different dimensions are also calculated. The dipole source orientation is assumed to be fixed under experimental conditions. A monitor is set up below the nanoantenna and QD to measure the electric fields of the near field. The collection angles that fall outside the NA of the objective lens are filtered out. The far-field projection and image generation are then calculated using a chirped-z transformation in MATLAB. The radiation of the isotropic emitter is calculated by adding together the images of the dipole source perpendicular and parallel to the antenna arm. This image can then be fitted with a 2D Gaussian function to determine the emitter's apparent location and compared with the input location of the simulation. All relevant data, codes for simulations and data analysis are available from authors on request.

4.4.2 Sample fabrication

L-shaped nanoscale plasmonic features are constructed using electron-beam (e-beam) lithography. In e-beam lithography, a focused electron beam is controlled to scan and draw predefined shapes on a surface with electron-sensitive films (photo-resists). Based on the property of the photo-resist, its solubility in the developing solution can either increase or decrease after the exposure to the electron beam. With the help of this technique, features with a few nanometer dimensions can be directly patterned onto the substrate without masks.

Samples were fabricated on ITO coated glass coverslips (Nanocs). First, the coverslip is cleaned by a rinse with acetone, isopropanol and DI water in sequence. A thin film (180 nm) of poly(methyl methacrylate) (PMMA) is then spin-coated onto the clean coverslip and

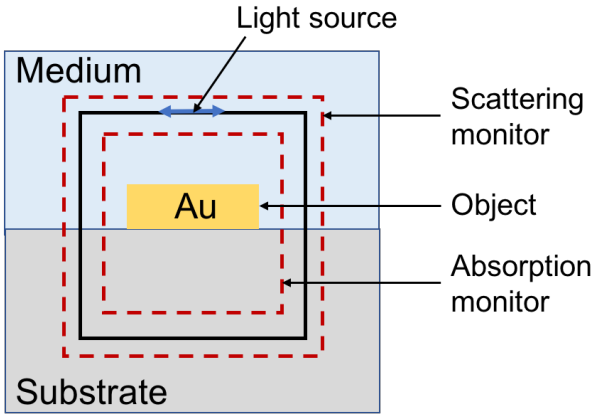

Figure 4.10: **Diagram of FDTD simulation geometry.** This cartoon shows the 2D layout of the geometry input for the FDTD simulation for antenna spectra response. The object (yellow) is positioned on top of the substrate (grey) surrounded by the medium (light blue). The black lines are the area of the total-field scattered-field light source with the blue arrow as the propagation direction. The absorption and scattering monitors (orange0 are placed at different positions relative to the light source in order to collect the corresponding radiation.

baked in preparation for the pattern writing. L-shapes with various dimensions and markers are patterned into the photoresist using the electron beam lithography (first layer). The pattern is developed in a MIBK/IPA 1:3 solution, followed by a plasma etching step to create sharp edges and improve metal adhesion to the surface. A layer of gold (60 nm) is then deposited using an electron beam evaporator (CHA) with a wetting layer of titanium (1 nm). After the lift-off step in acetone, gold on areas without electron beam exposure are removed, leaving only L-shaped antennas on the coverslip. A similar sample preparation step is carried for the second layer of electron beam lithography. For this layer, the instrument can automatically align the markers of two layers and pattern a 200-nm square next to each L-shape. After removing the exposed photoresist, the ITO coverslip was soaked in the diluted QD solution (1 m of Qdot™ 800 ITK™ Carboxyl Quantum Dots solution) for 60 min, followed by the photoresist lift-off, rinsing and drying.

4.4.3 Optical measurements

The samples were illuminated using a 642-nm laser diode source (Coherent) using an inverted microscope with a 100x oil-immersion objective (NA 1.49, Nikon). The excitation is filtered using a dichroic and an 800-nm long-pass filter. The excitation and emission polarizations are controlled through the polarizer and analyzer, respectively. Both the polarizer and analyzer are mounted on separate rotating stages controlled by Arduino, and QD images at different excitation/emission polarization combinations are recorded. Fluorescence was collected by an electron-multiplying charge-coupled device (EMCCD) camera with an extra set of lenses to increase the magnification further. The sample is mounted onto the sample stage and waited long enough until no apparent drift is observed. In each field-of-view (FOV), at least 25 QD-antenna units can be measured simultaneously. For each FOV, images are taken over four complete rotations of the polarizer (from 0° to 360° with 45° intervals). Later, the same FOV can be imaged using SEM with the help of patterned markers, and the true location of QDs can be compared with the measured locations.

4.4.4 Dip-pen Nanolithography (DPN)

As mentioned in previous sections, the current sample fabrication method requires precise alignment between two lithography steps to deposit QDs close to plasmonic structures, making the success rate reasonably low. A better approach that adopts the dip-pen nanolithography (DPN) method collaboratively with E-beam lithography has been carried out to directly 'write' single QDs with high precision (Figure 4.3). During DPN, an AFM tip first scans the sample to obtain the metallic landscape. The tip then moves away to dip into the QD ink, then moves directly back to the desired location for QD deposition. To guarantee single molecules rather than clusters of QDs, the concentration of QD solutions and dwell time during the print must be controlled [94, 96]. Compared with our previous method, this scanning probe techniques replace the original random distribution of emitters

with direct placement, leading to a much higher success rate. With the help of this approach, the relationship between QDs position, local plasmonic field intensity, and the mislocalization/mispolarization can be unveiled with an improved success rate and throughput. Thus, a better fundamental understanding of the coupling effects in plasmonic nanostructures can be constructed, which offers a promising route to improve the accuracy of near-field probing and sensing applications.

CHAPTER 5

PySOFI: an open source python package for SOFI

Super-resolution optical fluctuation imaging (SOFI) is a highly democratizable technique to provide optical super-resolution (SR) without requirement for sophisticated instrumentation. An open source package for SOFI algorithm is needed to support not only the utilization of SOFI algorithm, but also the community adoption and participation in SOFI algorithm further development. In this work, we developed *PySOFI*, an open source python package for SOFI analysis that offers the flexibility to test, modify and improve the algorithm. We provide a complete documentation for the package and a list of Jupyter Notebooks to demonstrate the package utilization. We discuss the architecture of *PySOFI*, illustrate how to use each functional module, and demonstrate how to extend the *PySOFI* package with additional modules. We expect *PySOFI* to facilitate efficient adoption, testing, modification, dissemination and prototyping of new SOFI-related algorithms.

5.1 Introduction

Super-resolution optical fluctuation imaging (SOFI) [68] is a widely used optical super-resolution method applicable for a broad range of conditions, where sophisticated control on the instrument and sample preparations are not required. It has attracted a growing community of active practitioners and developers over a decade. The advancements utilizing this technology include innovations in blinking dyes and fluorescent proteins, sample preparation [100–104], illumination schemes, experiment designs, data processing methods [5, 10, 69, 105–110], and integration with other methods [111–116]. With n^{th} order cumu-

lant analysis, the theoretical resolution improvement of SOFI is $\frac{1}{\sqrt{n}}$. This limit increases to $\frac{1}{n}$ when combined with deconvolution, presenting a great potential for further advancements for SOFI [68].

Our previous work have identified imperfections in high-order SOFI cumulants (e.g., cusp-artifacts [9]) due to the mixing of positive and negative virtual brightness of emitters. We introduced the concept of *virtual emitters* to interpret the physical meaning of SOFI cumulants, and identified the origin of such artifacts to be the adjacent negative and positive *virtual emitters* presented in the high-order SOFI cumulant image [9]. We also demonstrated how the validity of one of the most widely used SOFI processing method, bSOFI is negatively impacted [105].

We believe an insightful and thorough understanding of the method is crucial to ensure solid advancements in both SOFI and SOFI-relevant innovations. However, for new investigators without prior experience with SOFI analysis, there is often a steep learning curve to fully understand, modify, and extend the existing open-source packages [105, 117]. The existing SOFI analysis routines are implemented in either ImageJ or MATLAB. ImageJ requires professional programming skills if customization and modifications are required, while MATLAB requires a paid license. Such limitations present a even bigger challenge for new investigators as well as those who are interested in joining the SOFI community, but prefer not to use the existing packages blindly.

Here we present *PySOFI*, an open source package for SOFI analysis implemented in Python. Benefited from the active open-source community and the abundance of free learning materials for Python, *PySOFI* offers an easy option for investigators interested in adopting the SOFI algorithm. *PySOFI* focuses on engaging the community and is designed to be simple, modular, and highly customizable. *PySOFI* is hosted on GitHub to facilitate utilization, improvements, and continuous maintenance by the interested users and developers. A collection of examples is provided in the form of Jupyter Notebooks.

One can use *PySOFI* to explore and characterize SOFI analysis, validate the results

from the prior studies, and gain insights through exploration. *PySOFI* is also useful for prototyping and development of SOFI-related methods. Similar Jupyter Notebooks can be adapted for any new methods. In this way, the reproducibility of the results can be improved and application of the new method can promoted. We expect *PySOFI* to appeal to both beginners and experts by facilitating innovations where modification and extensions are required, and to further promote the scientific advancements among scientists interested in SOFI.

The rest of the manuscript is organized as follows. Section 2 provides an overview of the *PySOFI* package. Section 3 discusses the *PySOFI* software architecture design and analysis pipeline. Section 4 provides examples of SOFI analysis using *PySOFI*. Section 5 summarizes the work and discusses future directions.

5.2 *PySOFI* overview

We designed a straightforward architecture for the *PySOFI* package. As shown in (figure 5.1), *PySOFI* contains eight independent function modules (in the `functions` folder) and one data class (`PysofiData`). A detailed description of *PySOFI* is available in our online documentation. To get started with the installation, the user can follow this page.

The following modules are implemented to facilitate the *PySOFI* analysis pipeline. The `reconstruction.py` module provides capabilities for SOFI moments and cumulants calculations [68], as well as bleaching correction for a TIFF movie.

The `finterp.py` module provides Fourier interpolation on a TIFF stack, which is a necessary step for fSOFI alike analysis [106]. `filtering.py`, `deconvsk.py`, and `ldrc.py` constitute a collection of modules relevant to SOFI 2.0 [10] analysis. Specifically, the `filtering.py` module is for pixel-wise noise filtering along the time axis, the `deconvsk.py` module is for shrinking kernel deconvolution (DeconvSK) [5], and the `ldrc.py` is for local dynamic range compression (*ldrc*) of images with a large dynamic range of pixel values [5]. Additionally,

the `moca.py` module provides capabilities for multi-order cumulant analysis (MOCA). The `masks.py` module is used to generate Gaussian kernels, and the `visualization.py` module provides visualization options using an interactive visualization package `bokeh`. The data class module (`PysofiData`) is encapsulated in the `pysofi.py` file. The input parameters from the users, the raw data, and the intermediate results are bundled in the `PysofiData` object as attributes, and the processing steps as methods. The processing steps are implemented as function modules, and imported and used in the data class module.

In summary, the specific functions are implemented in the function modules, while `PysofiData` serves the purpose of organizing the data processing workflow.

***PySOFI* modules**

Data class	pysofi.py	Defines the main data class called "PysofiData"
Function modules	reconstruction.py	Contains tools for cumulant and moment reconstruction.
	finterp.py	Contains tools for Fourier interpolation on *.tiff stacks for fSOFI processing.
	filtering.py	Contains tools for noise filtration along the time axis.
	deconvsk.py	Contains tools for shrinking kernal deconvolution (DeconvSK).
	ldrc.py	Contains tools for local dyanmic range compression of images.
	visualization.py	Contains tools for visualization of the results.
	moca.py	Contains tools for Multi Order Cumulant Analysis (MOCA).
	masks.py	Contains tools for generating Gaussian kernels.

Figure 5.1: ***PySOFI* modules.** *PySOFI* contains one data class and eight function modules. Detailed descriptions are available in the online documentation for *PySOFI*.

Figure (5.2) provides the data-flow diagram that demonstrate the connections (arrows) between different processing steps (green squares) and different types of data (purple ovals). Three collections of SOFI analysis routines are implemented in the `PysofiData` class, including the "Shared Processes" that contains the traditional SOFI analysis steps [68], the "SOFI 2.0" collection that contains the routines for SOFI 2.0 processing [10] and the "MOCA" collection that enables multi-order cumulant analysis (MOCA) [5]. In the "Shared Processes" block, the processing steps including bleaching correction (BC), Fourier interpolation (FI), and moment and cumulant calculations can be performed in various sequences (green ar-

rows). In the "SOFI 2.0" block, one can perform noise filtering, deconvolution (DeconvSK), and local dynamic range compression (ldrc) on the image. The "MOCA" collection can be used to estimate the blinking statistics distribution (ρ-map) and brightness distribution (ϵ-map). In the data processing workflow, one can save and load the intermediate results for each processing step (purple arrows). This feature allows for break-point resumption in the analysis workflow, which is useful when one needs to inspect the results in the analysis workflow at each step. For example, in the "Shared Processes" collection, the intermediate results (purple ovals) can be saved as separate new TIFF files or stored as attributes in the `PysofiData` class object, and then passed to another processing step (purple arrow).

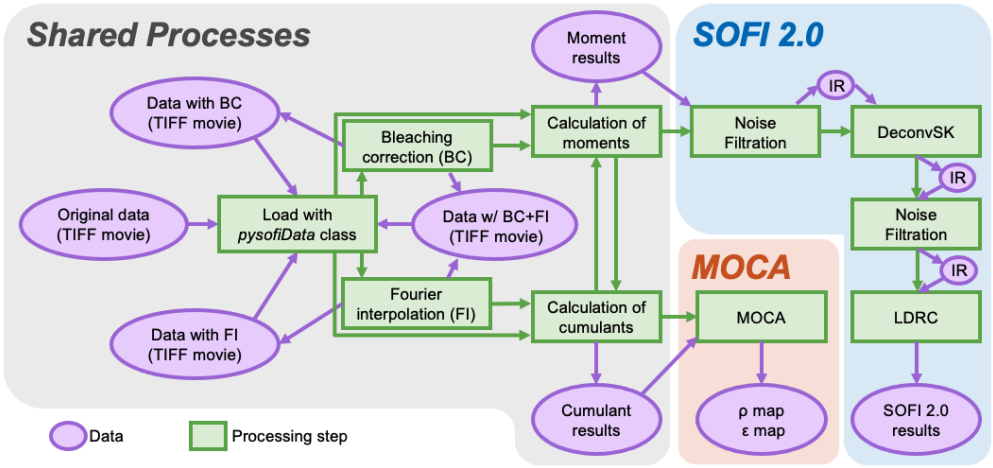

Figure 5.2: **Data-flow diagram for *PySOFI*.** Three collections of SOFI analysis routines are implemented in *PySOFI* as depicted in the diagram: Shared Processes, SOFI 2.0 analysis, and MOCA analysis. Green squares represent data processing steps with functionalities labeled for each step. The purple ovals represent the data types as labeled in the diagram. Intermediate results are abbreviated as "IR". The green arrow represents the direction of the data flow between different steps, and the purple oval represents input and output data types at different processing steps.

In general, we adopted a simple architecture for *PySOFI* with a collection of independent function modules and only one class module (the data class). The functions are imported and

used inside the data class across different methods as needed, therefore the implementation is flexible with minimum repetition of codes. The function modules can be implemented, modified, and tested independently, ensuring flexibility and convenience for maintenance. Extending the package can be done by implementing additional function modules. It can be used as a standalone process, or be integrated into the data processing workflow through the `PysofiData` class. Note that the "MOCA" collection is an implementation example that extends *PySOFI* package in a modular fashion. The investigators also have the flexibility to disseminate the *PySOFI* package and construct their own data processing workflow (similar to the `PysofiData` class).

5.3 Implementation of SOFI analysis using *PySOFI*

We provide a collection of Jupyter Notebooks (outlined in Figure 5.3) as examples for *PySOFI* implementations and applications. The prefix (E#) of each filename is used as a reference to each notebook in the following text for simplicity. We present example *PySOFI* analysis steps (E1 to E7), visualization of the result with combined color-map and transparency-map (E8), and the effect of data acquisition length on SOFI reconstruction performance (E9, E10). We also demonstrate characterization of cusp-artifacts (E11 and E12) and SOFI 2.0 analysis (E13). The analysis processes are integrated through the `PysofiData` class for all the notebooks except for the demonstration of noise filtration (E2).

In the text below, we provide brief descriptions of E1 to E6. The detailed description and examples are provided in the Jupyter Notebooks in the online Github repository.

5.3.1 Moment and cumulant reconstructions (E1)

Traditionally, SOFI achieves resolution enhancement by computing different orders of cumulants of optical signal fluctuations in time. The theoretical resolution enhancement for SOFI is $1/\sqrt{n}$ fold for the n^{th} order SOFI cumulant. Once combined with deconvolution,

Examples for *pysofi* analysis (Jupyter Notebooks)

Group	Notebook Name	Data
Processing steps demonstration	E1_MomentCumulantReconstructions	Block1.tif (live cell imaging)
	E2_NoiseFiltration	Block1.tif - Block20.tif (live cell imaging)
	E3_ShrinkingKernelDeconvolution	Block10.tif (live cell imaging)
	E4_LDRCMethod	Block1.tif (live cell imaging)
	E5_FourierInterpolation	Block10.tif (live cell imaging)
	E6_BleachingCorrection	Bleach_SlowVaryingRho_frame2000_Emi51.tif (simulation)
	E7_MOCA	3Emitters_frame5000_Emi3_close.tif (simulation) SlowVaryingRho_frame2000_Emi51.tif (simulation) RndomCurves_frame15000_rho04.tif (simulation)
Analysis explorations	E8_ReconstructionConvergence_SampleAnalysis	nobleach_frame20000_3.tif (simulation)
	E9_ReconstructionConvergence	frame1000_10000.npy frame11000_15000.npy frame16000_20000.npy (generated in E8)
	E10_ResultVisualization	RndomCurves_frame15000_rho04.tif (simulation)
Cusp-artifacts demonstrations	E11_CuspArtifactsDemo1_3Emitters	3Emitters_frame5000_Emi3_close.tif (simulation)
	E12_CuspArtifactsDemo2_SlowVaryingRho	SlowVaryingRho_frame2000_Emi51.tif (simulation)
SOFI 2.0 demonstration	E13_PysofiExample_LiveCellActinFilaments	Block1.tif - Block20.tif (live cell imaging)

Figure 5.3: **Jupyter notebook examples for *PySOFI*.** We provide 13 *PySOFI* demonstrations as Jupyter Notebooks which can be categorized into to 4 Groups (first column). The filenames (second column) indicates the focus of each Jupyter Notebook. The relevant data sets (third column) are shared on figshare. Brief descriptions of some notebooks (E1 to E8) are provided in the relevant section (fourth column). The theory behind E9 to E13 are not included in this manuscript but the relevant concepts are discussed in [9] and [10]. The notebooks are the *PySOFI* implementations of the relevant methods to support the utilization of them. In particular, in E11, we show the general guidelines for performing SOFI 2.0 analysis on live-cell fluorescence imaging results using *PySOFI*.

the theoretical resolution enhancement can increase to $1/n$.

To obtain the n^{th} order SOFI cumulant, one way is to construct the n^{th} order cumulant as a polynomial consists of moments from the first order to the n^{th} order, as shown in the previous work [68]. Another way, which is used by *PySOFI*, is to construct the following recursive relation: $Cum_n = G_n - \sum_{i=1}^{n-1} C_{n-1}^{i} \cdot Cum_{n-i} \cdot G_i$, where Cum_n represents the n^{th}

order cumulant, G_n represents the n^{th} order moment, and C_N^M means the number of combinations of "N choose M". Regarding the moment calculations, *PySOFI* support calculations of moments directly from the time series of each pixel. The moments can be also calculated as a reconstruction from a series of cumulants as used in our previous study [10].

The calculation of cumulants and moments are the fundamental processing elements in the SOFI analysis. The `PysofiData` class organizes the analysis workflow and can be used to calculate both moments and cumulants. Essentially, the relevant function modules are imported and integrated in the `PysofiData` to support such analysis. For example, the following scripts would calculate the 4^{th} order moment and cumulant of the specified TIFF stack named `Block1.tif` through the `PysofiData` class:

```
# load data into PysofiData object
filepath = '../sampledata'
filename = 'Block1.tif'
d = pysofi.PysofiData(filepath, filename)
# calculate the 4th order moment image
m_im = d.moment_image(order=4)
# calculate the 4th order cumulant image
k_set = d.cumulants_images(highest_order=4)
```

We can also directly import the function module, `reconstruction.py`, to perform the relevant calculations. This option is designed to support dissemination of the *PySOFI* package to facilitate independent analysis, which is often useful when developing new methods built upon SOFI analysis. The following scripts demonstrate how to perform such analysis with moment and cumulant calculations up to 4^{th} order:

```
# import the relevant function modules,
# and define the path and name for the data.
from functions import reconstruction as rec
```

```
filepath = '../sampledata'
filename = 'Block1.tif'
# calculate the 4th order moment image
m_set = rec.calc_moments(filepath, filename, highest_order=4)
# calculate the 4th order cumulant image
k_set = rec.calc_cumulants_from_moments(m_set)
```

More detailed demonstrations are available in the corresponding Jupyter Notebook (E1).

Temporal Noise Filtering (E2)

Temporal noise filtering is fundamental in the image processing for fluorescence microscopy, especially in scenarios where continuous and prolonged live cell imaging is desired where the excitation power is maintained at a low level to minimize photo toxicity and photo-bleaching. The lower excitation power often results in reduced signal to noise ratio. Traditional noise filtering is performed with a spatial filter where each image for every given time instance is spatially filtered independently. However, because noise filtering in the spatial spectrum domain is equivalent to a convolution operation of the image with the kernel corresponds to the inverse Fourier transform of the low-pass filter, it is conceivable that the spatial noise filtering would reduce the spatial resolution. On the other hand, to achieve a super-resolution movie, we are focusing on the sample conditions where the semi-static assumption is valid, which requires slow dynamics in the sample and the temporal noise filtering has been proven useful [10]. This is because slow dynamics ensures that the signal of interest exists in the low frequency domain while the noise is populated in the high frequency domain in the time axis, therefore the temporal spectrum filtering can be effective. Additionally, because this filtering is performed along the time axis, the spatial resolution is not directly influenced.

We have implemented such temporal noise filtering in *PySOFI* as a function module `filtering.py`. It is useful when analyzing multiple TIFF stacks corresponding to consec-

utive time-blocks. In such scenario, the feature is assumed to be semi-static within each individual time block, and the corresponding TIFF stack is analyzed independently. We can perform the temporal noise filtering on the results across all the time blocks to further enhance the image quality.

For example, we can perform the temporal noise filtering on the 6^{th} order moment images calculated from 20 blocks of TIFF stacks (each contains 200 frames) using the following scripts:

```
# First, we define the list of TIFF stacks
# that corresponds to 20 different time blocks of a movie:
filenum = 20
filepath = '../sampledata'
filenames = ['Block' + str(i+1) + '.tif' for i in range(filenum)]
# Second, we perform the sixth order moment calculations for all the blocks
dset = {}; m_set = {}
for filename in filenames:
    dset[filename] = pysofi.PysofiData(filepath, filename)
    m_set[filename] = dset[filename].moment_image(order=6, finterp=False)
# Third, we generate a noise filter as a 1-Dimensional Guasisan profile:
nf = masks.gauss1d_mask(shape = (1,21), sigma = 2)
# Last, we perfrom the time-axis noise filtering
m_filtered_set = filtering.noise_filter1d(dset, m_set, nf,
                                          return_option=True,
                                          return_type='dict')
```

The results from the temporal noise filtering are stored as a dictionary in the `m_filtered_set`, where keys for elements are file names for each block of TIFF images, and values are the corresponding filtered images. The filtered images are also updated to each `PysofiData`

objects as a `PysofiData.filtered` attribute. More detailed demonstrations are available in the corresponding Jupyter Notebook (E2).

5.3.2 Shrinking kernel deconvolution - DeconvSK (E3)

With the help of high-order SOFI analysis, the point spread function (PSF) of the optical system can be estimated [69], and deconvolution can be used to further enhance the image resolution by a factor of $\sqrt{n}$ for n^{th} order SOFI cumulant [69]. In SOFI 2.0 [5, 10], we developed and applied the shrinking kernel deconvolution (DeconvSK) method to SOFI images. The principle of deconvSK is that for a system with a Gaussian PSF, the estimated convolution kernel can be decomposed into a series of smaller Gaussian kernels. We design the series in a way to include only one parameter, and form a series of Gaussian kernels with decreasing width. More specifically, denote the system PSF (2D Gaussian function) as U, we have

$$U^{\frac{\lambda}{\lambda-1}} \otimes U^{\frac{\lambda^2}{\lambda-1}} \otimes \cdots \otimes U^{\frac{\lambda^n}{\lambda-1}} \propto U \tag{5.1}$$

where λ is an empirical parameter between 1 and 2 that determines the exponent, $\otimes$ represents the convolution operation, and $\propto$ represents the proportionality. In this way, we can decompose the overall deconvolution task into a series of lighter deconvolution tasks.

In *PySOFI*, DeconvSK is implemented in the function module *deconvsk.py* as well as in the `PysofiData.deconvsk()` method. `DeconvSK` requires two different input parameters, the λ in equation 5.1 can be set to be between 1 to 2. The width of the overall PSF with Gaussian approximation can be obtained from the cross-cumulant analysis [69] or directly estimated from the instrument configurations. The DeconvSK processing can be performed with the following commands through a `PysofiData` object:

```
# load data into a PysofiData object
filepath = '../sampledata'
filename = 'Block10.tif'
```

```
# Define an overall Gaussian PSF with estimated sigma value
deconv_psf = masks.gauss2d_mask(shape=(51, 51), sigma=2)
d = pysofi.PysofiData(filepath, filename)
# perfrom the shrinking kernel deconvolution through the PysofiData object
d.deconvsk(est_psf=deconv_psf, input_im=d.average_image(),
           deconv_lambda=1.5, deconv_iter=20)
```

We can also use DeconvSK in *PySOFI* directly through the *deconvsk.py* module:

```
#  take the average image of the TIFF stack
im2 = d.ave;
# import the deconvsk module
from functions import deconvsk as deconv
# perform the shrinking kernel deconvolution analysis
deconv_im2 = deconv.deconvsk(deconv_psf, im2, deconv_lambda, deconv_iter)
```

Figure 5.4 shows the deconvolution results on the relevant dataset used in our prior publication [10], we can see that the deconvolved results shows much more detailed structures as compared to the image without deconvolution. More detailed demonstrations are available in the corresponding Jupyter Notebook (E3).

5.3.3 Local dynamic range compression (*ldrc*) (E4)

One of the key challenges for high order SOFI cumulant calculations is the high dynamic range (HDR) of pixel intensities [68]. The HDR issue also exists in the high order moment images [10]. To mitigate such issues, We have developed the 'local dynamic range compression (*ldrc*)' method in our prior studies [10] and implemented it in the *PySOFI* package.

The *ldrc* algorithm rescales pixel intensities of a given image based on a reference image. First, a reference image with the same feature but a more confined dynamic range is defined

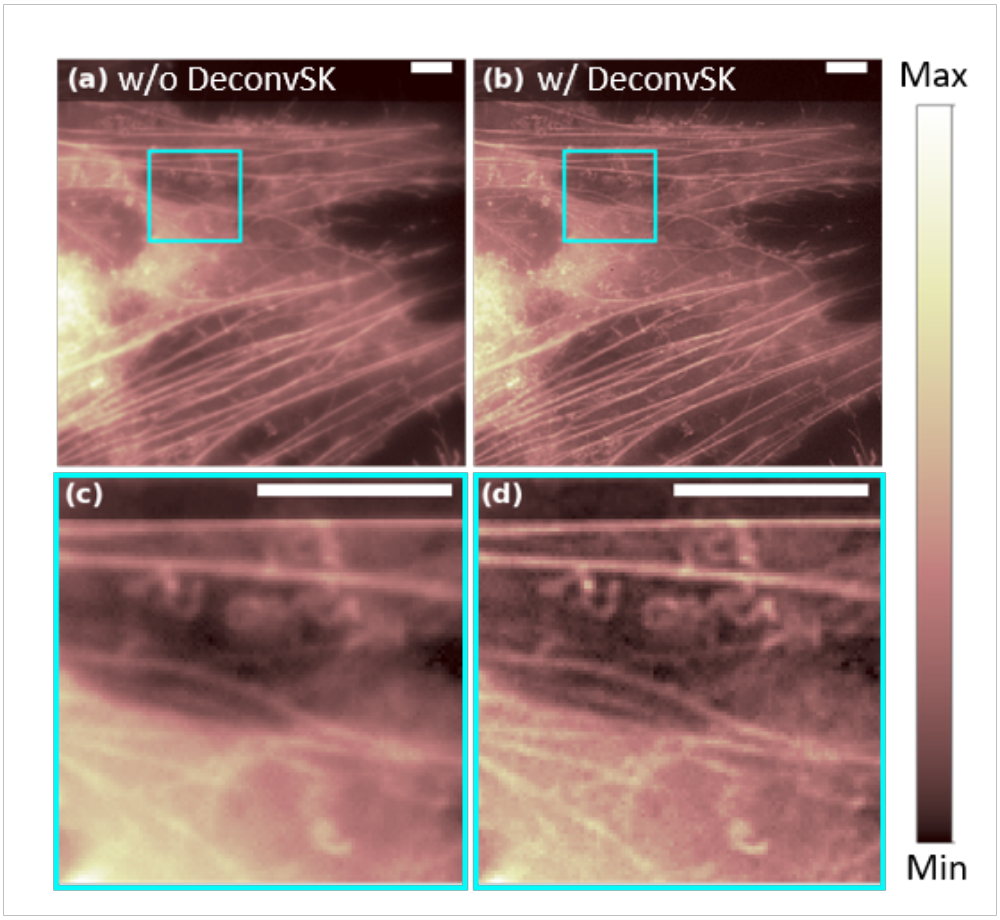

Figure 5.4: **DeconvSK demonstration.** Experimental demonstration of shrinking kernel deconvolution algorithm on HeLa cells transfected with Dronpa-C12 fused to β-Actin. Live cells were imaged with 30 ms frame integration and 200 frames in total. (a) Average widefield fluorescence image. (b) Average image after DeconvSK. (c) A zoom-in box of (a). (d) A zoom-in box of (b). Scale bars: $8\mu m$.

(e.g., the average image, the second-order moment or cumulant SOFI image). The compression is performed locally in a small window that scans across the image with a stride of 1 pixel. In each window, the pixel intensities of the original image are linearly re-scaled to share the same dynamic range as the reference window [10]. The final value of each pixel is the average of the corresponding re-scaled values of them across all windows covering it.

In *PySOFI*, *ldrc* is implemented in the function module ldrc.py and integrated in the `PysofiData.ldrc()` method. The following scripts will calculate the 6^{th} order moment (*m6*) and the average image (*mean*), and perform *ldrc* on *m6* using *mean* as the reference:

```
# first, import the two relevant function modules, reconstruction and ldrc
from functions import reconstruction as r
from functions import ldrc
# define the path and file name of the data file.
filepath = '../sampledata'
filename = 'Block1.tif'
# calculate the 6-th order moment (m6) and the average iamge (mean)
m6 = r.calc_moment_im(filepath, filename, order=6, frames=[0,50])
mean = r.average_image(filepath, filename)
# compress the dynamic range of m6 with reference to mean using ldrc
ldrc_im = ldrc.ldrc(mask_im=mean, input_im=m6,
                    order=6, window_size=[20, 20])
```

We can also perform the *ldrc* processing directly through the `PysofiData.ldrc()` method using the following script:

```
# load data into PysofiData object
filepath = '../sampledata'
filename = 'Block1.tif'
# load teh data into a PysofiData class object
d = pysofi.PysofiData(filepath, filename)
# calculate moments
d.moment_image(order=6, finterp=False)
# perfrom ldrc
d.ldrc(mask_im=d.ave, input_im=d.moments_set[6],
```

```
order=6, window_size=[20, 20])
```

Note that the direct *ldrc* processing on *m6* often yields visually non-optimal results (as shown in the relevant Jupyter Notebook (E3)), while the benefits are shown as a processing step in the SOFI 2.0 pipeline. In Figure 5.5, we compare the the partially processed SOFI 2.0 image (6^{th} order moment image with noise filtering and deconvolution but without *ldrc*) and the final SOFI 2.0 image (with *ldrc*). We can see that the information of the feature in the image are not lost without *ldrc*, but the feature are imperceptible due to the HDR issue. On the other hand, *ldrc* mitigates the HDR issue and provide an image where the dim features are shown more clearly. More detailed demonstrations are available in the corresponding Jupyter Notebook (E4).

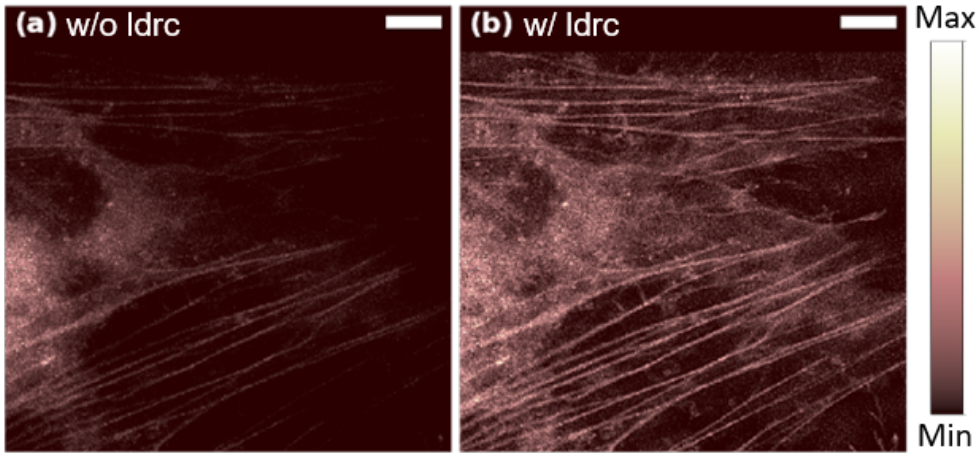

Figure 5.5: **ldrc demonstration.** Experimental demonstration of *ldrc* algorithm on HeLa cells transfected with Dronpa-C12 fused to β-Actin. Both images are processed using 6^{th} order moment, noise filtering and deconvolution, and obtained during the SOFI 2.0 analysis pipeline, before (a) and after (b) the *ldrc* step. Scale bars: $8\mu m$.

5.3.4 Fourier interpolation (E5)

Fourier interpolation stochastic optical fluctuation imaging (fSOFI) solves the finite pixelation problem of SOFI by adding virtual pixels using Fourier transforms [106]. We have implemented the Fourier interpolation method in *PySOFI* to integrate the fSOFI analysis as an optional processing step. In our implementation, for the forward Fourier Transform, the Fourier transformation matrix was created with a size the same as the input image. We created the inverse Fourier transformation matrix to include the extra interpolation position coordinates, and omitted the "zero-padding" step in the Fourier space to avoid burdening the computation.With the Fourier interpolation, the input image/video is 'projected' onto a more refined grid with finer pixel size.

In *PySOFI*, Fourier interpolation is implemented in the function module finterp.py and integrated in the `PysofiData.finterp_tiffstack()` method. We can perform the Fourier interpolation and save the output as as a series of .tiff stacks. For example, the following scripts will calculate the 2- and 4- fold Fourier interpolation of the initial 100 frames from the example data set *block10.tiff*, and save the interpolated images into two .tiff stacks: `block10_InterpNum2.tiff` and `block10_InterpNum4.tiff` respectively.

```
# import the relevant tools
from functions import pysofi
# load data into PysofiData object
filepath = '../sampledata'
filename = 'Block10.tif'
d = pysofi.PysofiData(filepath, filename)
# calculte the Fourier interpolation
d.finterp_tiffstack(interp_num_lst=[2,4], frames=[0,100],
                    save_option=True, return_option=False)
```

We can also perform the Fourier interpolation by using the `finterp.py` module as shown

below:

```
# import the relevant tools
import tifffile as tiff
from functions import finterp
# load a single image from the relevant data file
filepath = '../sampledata'
filename = 'Block10.tif'
im = tiff.imread(filepath + '/' + filename, key=15) # read a frame
# perform Fourier interpolation
finterp_im2 = finterp.fourier_interp_array(im, [10])
# perform a 10-fold interpolation in the image.
```

Figure 5.6 demonstrates the performance of the Fourier interpolation. Based on the Nyquist-Shannon sampling theorem [118,119], we recommend setting the interpolation factor at least two times the highest order for moment-/cumulant reconstructions. For instance, if we plan to start the SOFI 2.0 pipeline with the 6^{th} order moment image, we should pass `interp_num_lst = [12]` to `d.finterp_tiffstack`. However, in practice, depending on the dimension and length of the input file, Fourier interpolation might consume large processing memory and time. If computation resources are limited, we recommend saving the interpolated image stack as tiff files firs tinstead of returning them, and then process the new file. Besides `d.finterp_tiffstack`, another option to include Fourier interpolation in the SOFI processing pipeline is to pass (`finterp = True`) and a interpolation factor (`interp_num=6`) when calculating the moment/cumulant reconstructions (see section 3.4).

More detailed demonstrations are available in the corresponding Jupyter Notebook (E5).

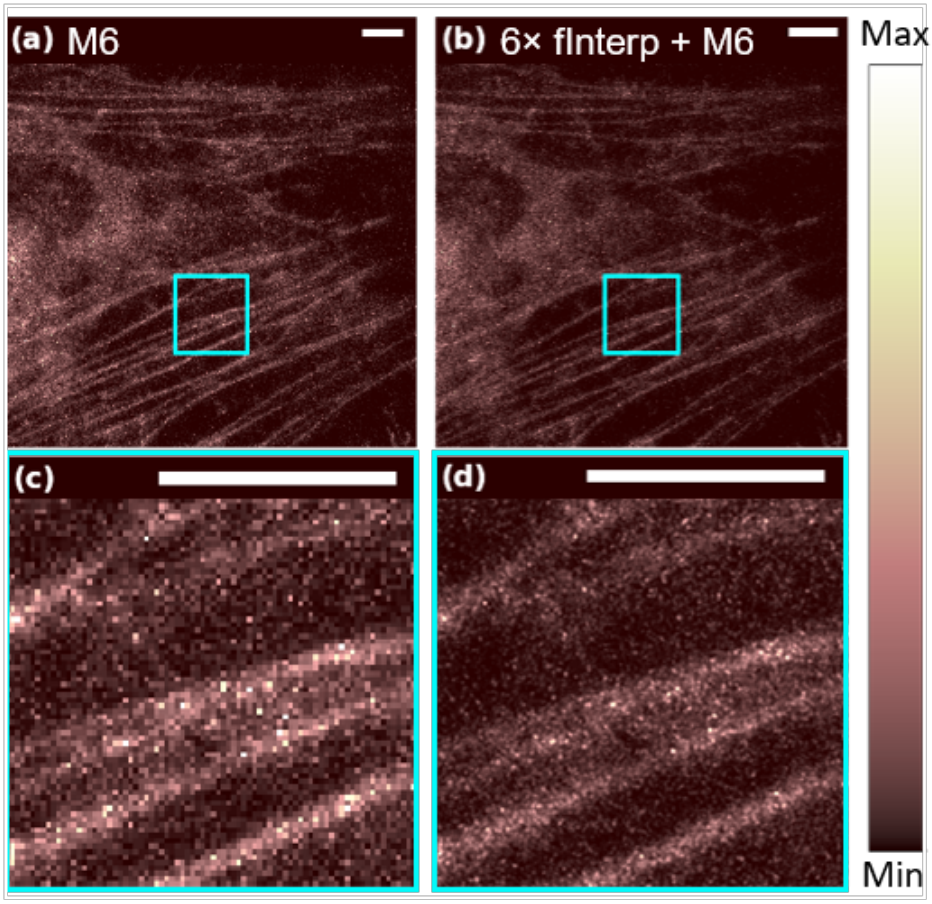

Figure 5.6: **Fourier interpolation demonstration.** Experimental demonstration of Fourier interpolation algorithm on HeLa cells transfected with Dronpa-C12 fused to β-Actin. (a) The 6^{th} order moment-reconstructed image of the original wide-field acquisition. (b) The 6^{th} order moment image after the Fourier interpolation. ldrc is performed on both (a) and (b) to compress the dynamic range of the reconstruction. (c) A zoom-in box of (a). (d) A zoom-in box of (d). Scale bars: $8\mu m$.

5.3.5 Bleaching correction (E6)

Photobleaching of fluorescent probes is a general concern for super-resolution imaging analysis methods. As for SOFI, photobleaching can cause errors in virtual brightness displayed in moment or cumulant images [9]. Photobleaching leads to the loss of the fluorescence signal,

which is mathematically equivalent as if the fluorophore is switched to a prolonged "off" state, degrading the quality of SOFI results. Therefore, a bleaching correction is critical.

PySOFI employs a bleaching correction technique [10] that divides the whole video into shorter blocks based on the total signal intensity, $I(t)$, where t is the time index, and $I(t)$ is the summation of all the pixel values of the image at time index t. The individual blocks are processed independently and combined subsequently to form a SOFI movie. First, the time series of the total signal intensity is smoothened to obtain a monotonically decreasing curve as an estimation of the bleaching profile of the movie. Then, based on the signal evolution over time, the sizes of the shorter blocks are determined so that the fractional signal decrease within each block (characterized by the bleaching correction factor, f_{bc}) is identical [10]. The final SOFI moment/cumulant images with bleaching correction are the average of those calculated from individual blocks. Fig. 5.7 shows that with the help of bleaching correction, the virtual brightness distribution and the photophysical properties (7c, 7f) are successfully restored, yielding similar values as compared to the simulated case without bleaching (7b).

PySOFI offers two ways for bleaching correction. One way is through the `PysofiData` class as shown below:

```
# import the relevant tools
from functions import pysofi
# load data into PysofiData object
filepath = '../sampledata'
filename_bleach = 'Bleach_SlowVaryingRho_frame2000_Emi51.tif'
# load the dataset with bleaching into a PysofiData class object d_bleach
d_bleach = pysofi.PysofiData(filepath, filename_bleach)
# calculate the sofi cumulants with bleach correction
k_set_bleach_corrected = d_bleach.cumulants_images(highest_order=7,
                                                   bleach_correction=True,
```

```
                                                    smooth_kernel=251,
                                                    fbc=0.04)
```

We can also directly import the relevant function module `reconstruction.py` and perform bleaching correction as shown below:

```
# improt the function module and define the path and file name of the dataset
from functions import reconstruction as r
filepath = '../sampledata/simulations'
filename_bleach = 'Bleach_SlowVaryingRho_frame2000_Emi51.tif'
# perform bleaching correction on the designated dataset.
r.correct_bleaching(filepath, filename_bleach, fbc=0.04, smooth_kernel=251,
                    save_option=True, return_option=False)
```

In this example, we applied bleaching correction to a TIFF stack, and the bleaching corrected movie is saved as a separate TIFF stack with the string "_bc" appended to the original file name.

More detailed demonstrations are available in the corresponding Jupyter Notebook (E6).

5.3.6 Result visualization (E10)

We provide some simple visualiztion options in `pysofi` including display an image, adjust the contrast for the image, and display multiple images for comparison, and display an image with user defined transparency map. `Bokeh` is used to offer interactive visualization for the display.

In this section, we discuss result display options supported by *pysofi*. Before using the functionalities, import the module with `from functions import visualization as vis`. The purpose of each function and sample scripts in this module are explained in detail below.

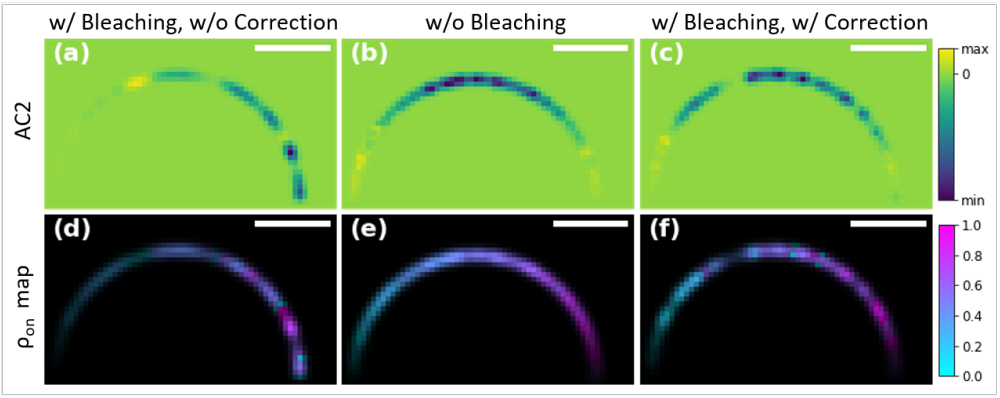

Figure 5.7: **Bleaching correction demonstration on a simulation data.** The fourth-order cumulant image (a-c) and multi-order cumulant analysis (MOCA) (d-f) is performed on a simulated video. A semicircle is populated with emitters with on-time ratios ranging from 0.01 (left) to 0.99 (right) with around 0.02 intervals. For emitters with photobleaching but without a bleaching correction step, the reconstructed pixel intensities (a) and emitters on-time ratio estimation (d) are far off from the true values (b, e), while the bleaching correction restores the information (c, f). Scale bars: $1.4\mu m$.

5.3.6.1 Interactive visualization with `Bokeh`

pysofi contains a visualization module using `Bokeh`, which renders its graphics using HTML [120]. We recommend `Bokeh` for for creating custom interactive visualizations with easy zoom in/out, check pixel values and change field-of-view either on a single image or on multiple images simultaneously. The following functions are included in *pysofi* using `Bokeh`.

- `bokeh_visualization` - plot a single grayscale image.

```
vis.bokeh_visualization(d.get_frame(0), palette='pink',
                        save_option=False, imshow_same=True)
```

This command plots the first frame of the `Pysofi` object `d` with the colormap set to

'pink'. By default, the Bokeh image is set to render inline in the Jupyter Notebook. We can change the parameter `save_option=True` to render it in a static HTML file and save the file as well. The default y-axis direction in `Bokeh` is flipped compared to `matplotlib.pyplot.imshow`. By passing `imshow_same=True`, we can make the two plotting modalities align with each other.

- `bokeh_visualization_mult` - plot multiple grayscale images side-by-side.

```
vis.bokeh_visualization_mult([d.get_frame(0), d.average_image()],
                             title_lst=['Frame #1', 'Average image'])
```

  Using this command, we can show the first frame and the average image of `d` together that share simultaneous tool transformation, such as zooming in and translation. We can assign the image title for individual images using the parameter `title_lst`. Parameters including `palette`, `save_option` and `imshow_same` can also be passed to this function.

- `bokeh_visualization_rgba` - plot a single RGBA image. This function can help the user check the image before being saved as a .jpg or .avi file (see example below).

Note that when the image is too large (more than 1500 * 1500 pixels), users are likely to come across an error using `Bokeh`. In this case, we recommend using `matplotlib.pyplot.imshow` instead.

5.3.6.2 Contrast adjustment

To better visualize images from fluorescence microscopy (especially live-cell results), the user has the option to adjust display contrast using `enhance_contrast(im, display_contrast)`, where `im` is the input image and `display_contrast` is a constant that multiplies all pixel values. The image with adjusted contrast can be plotted with `bokeh_visualization_rgba` or saved in a .png/.avi file:

```
en_im = v.enhance_contrast(d.save, display_contrast=1.4)
v.bokeh_visualization_rgba(en_im)
```

5.3.6.3 Image visualization with a transparency map

After extracting emitters' photo-physical information (e.g., on-time ratio, brightness) using MOCA (see section 4), we recommend color-coding the features and adjusting the pixel intensity based on a transparency map. For instance, one can set the colormap for the on-time ratio image to 'pink' and use the second-order moment reconstruction as the transparency map through element-wise multiplication. Such processing can be achieved with `add_transmap(im, trans_map, cmap)` in *pysofi*, where `im` is the input grayscale image whose intensity represents a photo-physical parameter (e.g., on-time ratio) that need to be color-coded, `trans_map` is the transparency map that determines the pixel values of the color-coded image, and `cmap` is the colormap. As for visualizing MOCA results, we recommend using the second-order SOFI image as the transparency map because it has moderate dynamic range expansion, improved resolution, and reduced background. Note that the input and transparency image should share the same dimensions. Users can select the built-in colormaps accessible via `matplotlib.cm.get_cmap`, or set up their own colormap as a three-column array of RGB triplets.

5.4 Implementation of multi-order cumulant analysis (MOCA)

This section describes multi-order cumulant analysis (MOCA) in *PySOFI*. The implementation is intended as an independent function module (*moca.py*) in the `functions` folder, providing an example for *PySOFI* extension.

MOCA characterizes and quantifies the photophysical properties of SOFI results [5]. It combines multiple orders of SOFI cumulants to construct a global fitting problem, and solves for the on-time ratio and on-state brightness for each pixel. A detailed description of

MOCA can be found in [5]. In brief, MOCA is composed of two analysis steps. The first step is to estimate the PSF from the cross-correlation analysis. In the second step, MOCA reformulates multiple orders of cumulants and construct a global fitting problem to solve for the on-time ratio and on-state brightness. We briefly introduce the two analysis steps for MOCA below.

5.4.1 PSF estimation from SOFI auto-/cross-cumulants

The n^{th}-order SOFI auto-cumulants ($AC_n(\vec{r})$) are images where the value of a pixel at location $\vec{r}$ is the cumulant value calculated from a single-pixel corresponding to the same position in the input data. Cross-cumulants ($XC_n(\vec{r})$) are images where a pixel at position $\vec{r}$ is calculated based on the cross-cumulants of a group of different pixels whose geometric center is located at the image pixel position $\vec{r}$. Intrinsically, the choice of the group of pixels used to calculate a SOFI-XC_n pixel can either be n distinct pixels or less than n pixels where a subset of the pixels can be used more than once [69]. By combining different orders of SOFI-AC_n and different orders of SOFI-XC_n with different choices of pixel combinations, one can achieve a robust estimation of the PSF through a global fitting.

We start with the mathematical expression of the n^{th}-order SOFI auto-cumulants AC_n and SOFI cross-cumulants XC_n (with all the time lags equal to 0):

$$\begin{aligned} AC_n(\vec{r}) &= \sum_{k=1}^{N} U^n(\vec{r} - \vec{r_k})\epsilon_k^n\omega_{k,n} \\ XC_n(\vec{r_1}, \vec{r_2}, ..., \vec{r_n}) &= \exp\left(- \frac{\sum_{i=1}^{n}\sum_{j=i+1}^{n}(\vec{r_i} - \vec{r_j})^2}{2\sigma^2 n} \right) \sum_{k=1}^{N} U^n(\vec{r_{gc}} - \vec{r_k})\epsilon_k^n\omega_{k,n}, \end{aligned} \tag{5.2}$$

where k is the emitter index, ϵ_k is the brightness of on-state of emitter k and ω_k is the n^{th} order cumulant of the blinking profile of the k^{th} emitter. U is the PSF of the optical system that can be assumed as a 2D Gaussian function $U(\vec{r}) = \exp\left(-\frac{r^2}{2\sigma^2}\right)$ (we consider 2D images here). $\vec{r_{gc}}$ is the geometric center of set of pixels used for the cross-cumulant calculations, for which we have $\vec{r_{gc}} = \frac{1}{n}(\vec{r_1}, \vec{r_2}, ..., \vec{r_n})$. If we carefully choose the set of pixels to have geometric

center located at $\vec{r}$, we would have the following:

$$\frac{XC_n(\vec{r}_1, \vec{r}_2, ..., \vec{r}_n)}{AC_n(\vec{r})} = \exp\left(- \frac{\sum_{i=1}^{n} \sum_{j=i+1}^{n} (\vec{r}_i - \vec{r}_j)^2}{2\sigma^2 n} \right),$$
$$\text{where } (\vec{r}_1, \vec{r}_2, ..., \vec{r}_n) \text{ are selected such that: } \frac{1}{n} \sum_{i=1}^{n} \vec{r}_i = \vec{r}. \tag{5.3}$$

We define $\xi = \sqrt{\frac{\sum_{i=1}^{n} \sum_{j=i+1}^{n} (\vec{r}_i - \vec{r}_j)^2}{n}}$ to simplify the notation into the following:

$$\frac{XC_n(\vec{r}_1, \vec{r}_2, ..., \vec{r}_n)}{AC_n(\vec{r})} = \exp\left(- \frac{\xi^2}{2\sigma^2} \right), \tag{5.4}$$

where XC_n and AC_n are computed from the imaging data, and ξ can be calculated based on the choices of the pixel combinations. The only unknown is σ that characterizes the size of PSF. In this case, multiple pixel combinations can be selected to create different $\frac{XC_n}{AC_n}$ and ξ^2 values, and a global fitting can then be applied to estimate the PSF (σ). We demonstrate with $n = 2$ in this manuscript, but the principle applies to any order and can be implemented when necessary. Details of the global fitting approach are explained in chapter 7 of [5].

5.4.2 Local parameter mapping from MOCA

Assume that the spatial variance of the photophysical properties of the fluorophores are small enough to be invariant within the range of the spatial resolution of the lowest order cumulant used [9], n^{th}-order SOFI auto-cumulants can be simplified by removing the emitter indices and expressing the relevant physical quantities as spatial variables:

$$AC_n(\vec{r}) = \Big(L(\vec{r}) \otimes U(\vec{r})^n \Big) \varepsilon(\vec{r})^n \omega_n(\vec{r}), \tag{5.5}$$

where $U(\vec{r})$ is the PSF, $U^n(\vec{r})$ is the virtual PSF for n^{th} order SOFI images, and $\otimes$ indicates spatial convolution operator. $L(\vec{r})$ encodes the location information of emitters, for which we have $L(\vec{r}) = 1$ if there is an emitter at location $\vec{r}$, and $L(\vec{r}) = 0$ otherwise. ϵ_k and $\omega_{k,n}$ in equation 5.2 are assumed to have small spatial variations where emitter brightness and blinking statistics are primarily dependent on the emitters' local environment (such as

PH level or oxygen level). Thus, in equation 5.5 we replace the notation of ϵ_k into $\varepsilon(\vec{r})$ that describes the summation of the on-time brightness of emitters at $\vec{r}$. Similarly, $\omega_{k,n}$ is replaced as $\omega_n(\vec{r})$ to describe the blinking statistics of emitters at $\vec{r}$. Note that $\omega_{k,n}$ is a polynomial function of the on-time ratio ρ_{on} (shown in equation 4.2 in [9]). With the reformatted equation 5.5, $\epsilon(\vec{r})$ and $\omega_n(\vec{r})$ encode the physical properties of the emitters as an environment-dependent spatial variable.

We can then define a new quantity, X_n, to connect multiple orders of SOFI auto-cumulants by convolving both sides of equation 5.5 with $U^{\frac{2n}{n-2}}$ followed by dividing with AC_2:

$$X_n = \frac{AC_n \otimes U^{\frac{2n}{n-2}}}{AC_2} = \frac{\varepsilon^n \omega_n \left(L \otimes U^2\right)}{AC_2} = \varepsilon^{n-2}\frac{\omega_n}{\omega_2}, \tag{5.6}$$

Specifically, the numerical values of X_n can be calculated from different orders of auto-cumulants. Meanwhile, as shown in equation 5.6, we know that X_n is a function of ε and ρ_{on} (because ω_n is a function of ρ_{on}). Therefore, we can calculate various orders of X_n to obtain an equation system for which the only unknown variables are ε and ρ_{on}, and any regression method that solves a polynomial equation system with 2 unknown variables can solve for the spatial variables ε and ρ_{on}.

Here we solve the equation system by reformatting equation 5.6 further:

$$\frac{1}{\varepsilon} = \left(\frac{1}{X_i} f(\rho_{on}, \ldots, \rho_{on}^{i+2})\right)^{i+2}, \tag{5.7}$$

which describes a curve in a 2D coordinate system with axes $\frac{1}{\varepsilon}$ and ρ_{on}. We calculate auto-cumulants up to the 7^{th} order, and use $X_3 \sim X_7$ (five equations, five curves) to find the global optimal solution for $\frac{1}{\varepsilon}$ and ρ_{on}. Note that ρ_{on} (x-axis) is naturally bounded between 0 to 1, and ε is naturally positive so $\frac{1}{\varepsilon}$ (y-axis) is bounded between 0 and 1, therefore we have a bounded 2D space to search for the optimum solution.

Ideally, the common crossing point of multiple curves presented by the equation system would be the solution. But due to numerical errors and imperfections of the model, the five curves wouldn't have a common crossing point. In our implementation, we first define a

quantity $D(\rho_{on})$ as the sum of mutual distances square of $\frac{1}{\varepsilon}$ (y-axis) among the points on all the curves at each ρ_{on} value, which can characterize the dispersion of those points. We sweep through the ρ_{on} values (x-axis) to calculate $D(\rho_{on})$, and determine the final solution of ρ_{on} to be the one that yields the smallest $D(\rho_{on})$ value. The final solution of $\frac{1}{\varepsilon}$ is determined by the average of the y-coordinates among all the identified crossing points. We fit such equation system for every pixel to map $\rho_{on}(\vec{r})$ and $\varepsilon(\vec{r})$ values to obtain the spatial distribution of the photo-physical properties of the emitters.

5.4.3 Use MOCA with *PySOFI* (E7)

MOCA is implemented as an extension module supported by existing *PySOFI* modules and functions. Here, MOCA methods are imported as the `moca.py` module directly as shown below:

```
# define path and parameters
filepath = '../sampledata/simulations'
filename = '3Emitters_frame5000_Emi3_close.tif'
frames = [0, 1000]
tauSeries = [0, 0, 0, 0, 0, 0, 0]
psf_dim = (301, 301)
res = 1000
# use the moca module to perform the moca analysis
ac, rho_ma, eps_map = moca.moca(filename, filepath, tauSeries,
                                frames, psf_dim, res)
```

To demonstrate the performance of MOCA under a complex condition, we created a simulated data set with 18 curves randomly decorated with blinking emitters. The ρ value of each curve is selected among 0,3, 0.5 and 0.7 (six curves for each ρ value). Among six curves with the same ρ value, two of them are 2 times brighter than the other four. As shown in

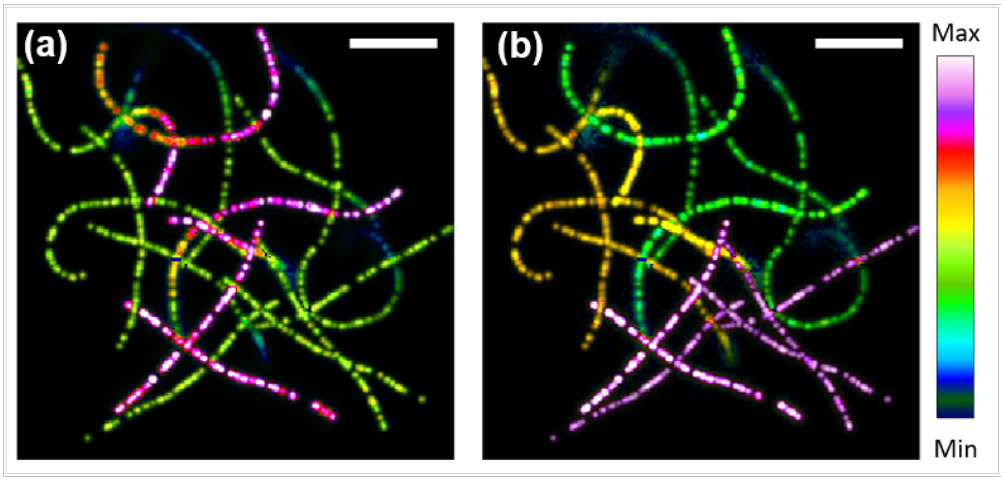

Figure 5.8: MOCA demonstration on simulated filaments. Simulated crossing filaments with different ρ's are generated. There are three ρ's, 0.3, 0.5 and 0.7, and for each ρ, there are six curves. MOCA estimates the on-time ratio and brightness of emitters precisely even at the intersections. Scale bar: $7\mu m$.

figure 5.8, MOCA successfully recovered different on-time ratio and emitter brightness under various conditions (e.g., intersections of filaments with emitters with different photophysical properties.

More examples are available in the corresponding Jupyter Notebook (E7).

5.5 Discussion

In this work, we developed *PySOFI*, an open source python package for SOFI analyses. *PySOFI* contains the essential functionalities for conventional SOFI analysis as well as several derivative methods [5, 9, 10, 106].

PySOFI adopts a simple architecture, where all the data processing steps are implemented as independent function modules, and only one class module (the data class `PysofiData`) is used to manage the data processing workflow. The functions can be tested independently and used in different processing pipelines. A fast prototype on new analysis can be achieved

by disseminating and reorganizing the processing step. Like the example of MOCA as a *PySOFI* extension module in section 4, one can implement additional processing steps as independent python functions with the help of existing *PySOFI* functions. New functions can be used as standalone modules, or can be integrated into the `PysofiData` class to support the new analysis pipeline. New classes can be constructed for different analysis pipelines as well.

We adopted Sphinx to manage the *PySOFI* documentation, which is available as an online documentation to facilitate community usage. Additionally, each processing element of the analysing pipeline are demonstrated in individual Jupyter Notebooks. In each notebook, we also provide instructions on how to tune processing variables and explore input data. *PySOFI* is housed on GitHub as an open source repository, any interested individuals can learn, inspect, validate and contribute to the package. The user interactions on GitHub (e.g., fork, create pull requests, and report issues) engage the community communications. We expect *PySOFI* to benefit general SOFI users for existing SOFI analysis, as well as developers and new investigators interested in developing new SOFI-relevant analysis method.

5.6 Data Availability

The data for this project is partially available on the project repository, and partially available on figshare.

CHAPTER 6

Characterization of fluorescent protein Dronpa-C12

6.1 Introduction

Fluorescent protein with photoinduced switching properties is one of the most attractive fluorophores to realize super-resolution imaging in sub-cellular systems with dynamic processes [121–123]. Intensive research has been conducted to find photochromic substances that switch readily and persistently at the atomic level. One great candidate of fluorescent protein that has been widely recognized is the green fluorescent protein (GFP). The photoswitching behaviors of GFPs and GFP-like proteins qualify them to single-molecule biosensing and super-resolution imaging, enabling detection of fast dynamics in live cells [124–127].

Recently, one reversibly photoswitchable fluorescent protein called Dronpa has gained particular interest due to its fast response to light and a significant number of switching events at the single-molecule level compared to other GFP mutants [128,129]. From ensemble spectroscopy, Habuchi and co-workers find that Dronpa converts to a dim protonated form on intense radiation at 488 nm and returns to the bright deprotonated state when exposed to weak light at 405 nm. Thus, by controlling the intensity of 488- and 405-nm lights, the photoswitching of Dronpa can be driven and repeated more than 100 times with high response speed (in milliseconds) [129]. Based on results from the ensemble and single-molecule measurements, they also developed a detailed photophysical model that describes interconversion between different states quantitatively.

The Miawaki lab has developed another mutant with even more photoswitching cycles to enable longer optical measurement duration. This mutant of Dronpa, Dronpa-C12, appears to have lower fluorescence intensity at the bright state while can support more extended imaging before photo-bleaching. To better take advantage of fluorescent proteins like Dronpa-C12, it is crucial to conduct a detailed characterization of their photophysical properties. In this chapter, the dependence of photophysical parameters of the fluorescent protein Dronpa-C12 on the intensities of the illumination in the solution, immobilized on the surface and in transiently-transfected live cells, are studied. The blinking and photobleaching/photoswitching rates as functions of excitation-only (488 nm) and excitation- (488 nm) and photoswitching- (405 nm) lasers with varying intensities are extracted both at the single-molecule and the ensemble level. Rates in these three different environments are compared. With all the parameters in hand, detailed Jablonski diagrams and rate-equation models can be constructed for future applications.

6.2 Experimental Procedures

6.2.1 Plasmid Construction and Protein Production.

The sequence of Dronpa-C12 is fused into vector pRSFDuet-1 along with 6xHis-tag using PCR and Gibson assembly. Then, the plasmid is transformed into BL21 competent E. coli cells, cultured, and induced with isopropylthio-beta-D-galactopyranoside (IPTG). The proteins are then affinity-purified using cobalt agarose beads (Gold Biotechnology). Gibson assembly is also used to fuse these proteins to live-cell organelles (β-actin) for live cell photophysical characterization. For live-cell studies, we use two different cell lines that are used for the study of lung cancer, human bronchial epithelial cells (HBECs) and adenocarcinomic human alveolar basal epithelial cells (A549). The cells used in this study are transfected with the plasmid fused with sequence of Dronpa-C12-β-actin.

6.2.2 Sample Preparation

A list of characterization options is shown in figure 6.1. The properties of Dronpa-C12 fluorescent proteins are characterized for their photoblinking and photobleaching parameters both *in vitro* and in live cells. To mimic the live cell environment, different methods to immobilize fluorescent proteins *in vitro* were carried out. Since it is difficult to extract single-molecule blinking properties in live cells, our strategy is to compare the bleaching behaviors of Dronpa-C12 under different *in vitro* preparation methods, and select the one that has the closet performance compared to that in live cells. Then, we will repeat that chosen method, and by controlling the concentration of the fluorescent protein solution, we can carry out blinking measurements on single-molecule level.

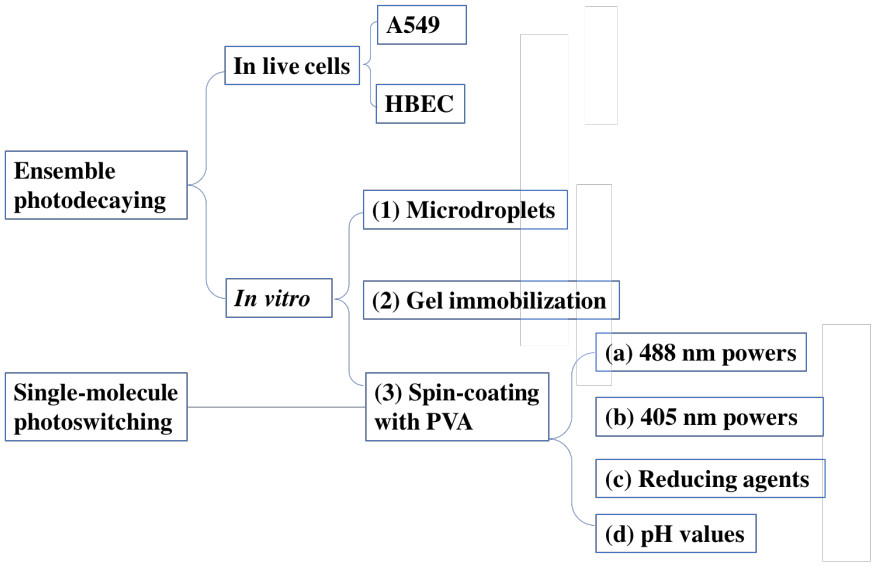

Figure 6.1: Sample preparation options for Dronpa-C12 characterization both *in vitro* and in live cells.

(1) Microdroplets: The glass coverslips are first cleaned by washing with acetone and 70% ethanol for 3 minutes, rinse with DI water, and leave to dry by air. Prepare a stock dilution of the purified protein with an optical density around 0.1 in phosphate buffered saline (PBS) solution, containing 0.1% bovine serum albumin (BSA). Prepare another solution of 1:1

mixture of 1-octanol and PBS and mix vigorously. When the phase separation is complete, transfer $45\mu l$ 1-octanol from the top phase and $5\mu l$ fluorescent protein solution into a new microfuge tube to form the emulsion. Invert the tube a few times and tap the tube until there exists uniform "bubble"-like droplets. Sonicate the tube for 30-40s until the solution gets cloudy, then transfer the mixture onto the center of one clean coverslip. Cover with another coverslip to form a 'sandwitch' sample with evenly distributed microdroplets with varying diameters. Wait 10-15 minutes before the optical measurements for microdroplets to settle down on the coverslip. In general, larger bubbles are at the center of the coverslip., and only in the bubbles can we detect the fluorescence signals.

(2) Gel immobilization: The gel preparation steps are the same are for typical gel electrophoresis experiments. However, instead of pouring the gel into a gel cassette, 'micro gel pad' are formed on a clean glass coverslip. Afterwards, a droplet of diluted fluorescent protein solution is put down onto the gel surface. Wait for fluorescent proteins to slightly diffuse into the gel and buffer solution to evaporate, then cover another coverslip onto the gel, and flip the sample for optical measurements.

(2) Spin-coat: For both ensemble and single-molecule level *in vitro* characterization of Dronpa-C12, purified protein are immobilized in the polymer matrix in various concentrations, and then deposited on the glass coverslip for imaging. The candidates for the polymers are poly(vinyl alcohol) (PVA), poly(ether imide) (PEI) and ploy(ethylene glycol) (PEG). It has been demonstrated that the glass transition temperature T_g of the polymer is related to the rigidity of the polymer and the photophysical behaviors of the fluorophores that trapped in the polymer matrix [130]. In this case, we choose three types of polymers that differ in T_g. PVA has relatively high Tg (353K) [131] and is more rigid; PEI's T_g is smaller (217K) [132] and is much softer than PVA; while PEG is the lowest in T_g (207K) [133] and the softest. The ensemble decaying rates of the fluorescent proteins immobilized in three polymer matrices are compared, and the polymer that has the rate closest to the decaying rate of that in the live cells will be determined.

6.2.3 Fluorescence Microscopy

Samples were mounted on an inverted microscope equipped with a ×100 oil immersion objective lens (OLYMPUS UPLANSAPO, numerical aperture 1.4). The fluorescent protein will be excited by 488 nm laser (cube-488-50c, Coherent, Santa Clara, CA) and re-excited by 405 nm laser (MDL-III-405, Opto Engine, Midvale, UT). Two laser beams were combined using a 432 nm long pass filter. The light path is designed for convertible wide-field and total internal reflection fluorescence (TIRF) imaging (figure). An Electron Multiplying CCD (EMCCD) camera (iXon, ANDOR) is operated for both ensemble and single-molecule imaging. EM Gain was set to 300 for amplification of weak signal, and the exposure time to 30 ms. The detection path is equipped with an additional pair of lens to achieve an overall magnification of ×140x. For ensemble measurements, the change of total fluorescence intensity over acquisition time is plotted and fitted to exponential decaying functions to determine the photobleaching lifetimes. For single-molecule photoblinking measurements, analysis workflow consists of localizing a single molecule in the image series, calculating the integrated fluorescence intensity from the diffraction limited spot corresponding to the molecule in each image of the series, and plotting the integrated intensity as a function of time. For both ensemble and single-molecule conditions, we will study how (a) excitation power, (b) re-activation power, (c) reducing agents, and (d) local pH values would affect the photophysical properties of fluorescent proteins (figure 6.1).

6.3 Characterization of Dronpa-C12 ensemble photo-decaying

For live-cell imaging, a 488-nm laser ($126 W/cm^2$) is used to excite the fluorescent protein. Total fluorescence intensity as a function of time is plotted and fitted with bi-exponential decay

$$I = p_1 * e^{-k_1 t} + p_2 * e^{-k_2 t}$$

where k_1 and k_2 are decaying rates, and p_1 and p_2 are the corresponding initial quantities. Both types of live cells show similar photo-decaying lifetimes. However, the overall fluorescence intensity of A549 cells is lower than HBEC cells, which is due to lower labeling efficiency of A549 cells.

Among different samples for *in vitro* measurements, ensemble photo-decaying behaviors of Dronpa-C12 vary broadly. Specifically, when fluorescent proteins are in microdroplets or immobilized by gel, they decay mono-exponentially (figure 6.2a,b). When fluorescent proteins are spin-coated onto the coverslip in the PVA matrix, the decaying behavior of Dronpa-C12 is more consistent. More importantly, PVA created an environment that Dronpa-C12 can decay bi-exponentially with similar lifetime as in live cells (figure 6.2c,d). This may be due to that different rigidities of different materials make the speed of conformational changes of fluorescent protein different [134], and the rigidity of PVA matrix matches that of the live-cell environment. Thus, further study on the influence of local environment and laser intensities on the ensemble photodecay and single-molecule photoswitching of Dronpa-C12 was carried out using this method.

Since the intensities of excitation and re-activation lasers and parameters of local environment like pH values and oxygen concentration may influence the photodecaying behavior of this fluorescent protein, it is essential to characterize the photophysical response of Dronpa-C12 first, and see whether it can be controlled with powers of both excitation of re-activation lasers. Previous research has shown that high oxygen level can normally accelerate the photobleaching process, and reducing agents help to prolong the photodecaying lifetimes. In our study, adding the reducing agent dithiothreitol (DTT) directly to the protein solution does not slow down the photodecaying, while spincoating another layer of DTT-PVA onto the protein-PVA layer can increase the lifetimes. To study the effect of the pH value of the solution, Dronpa-C12 in PVA-PBS solutions with a pH value of 6.5, 7.0, 7.5, 8.0, 8.5, 9.0 or 10.0 are prepared and spin-coated onto the coverslip. As we can see from figure 6.3, two rates change almost simultaneously and both reach the peak at pH = 8.0. After character-

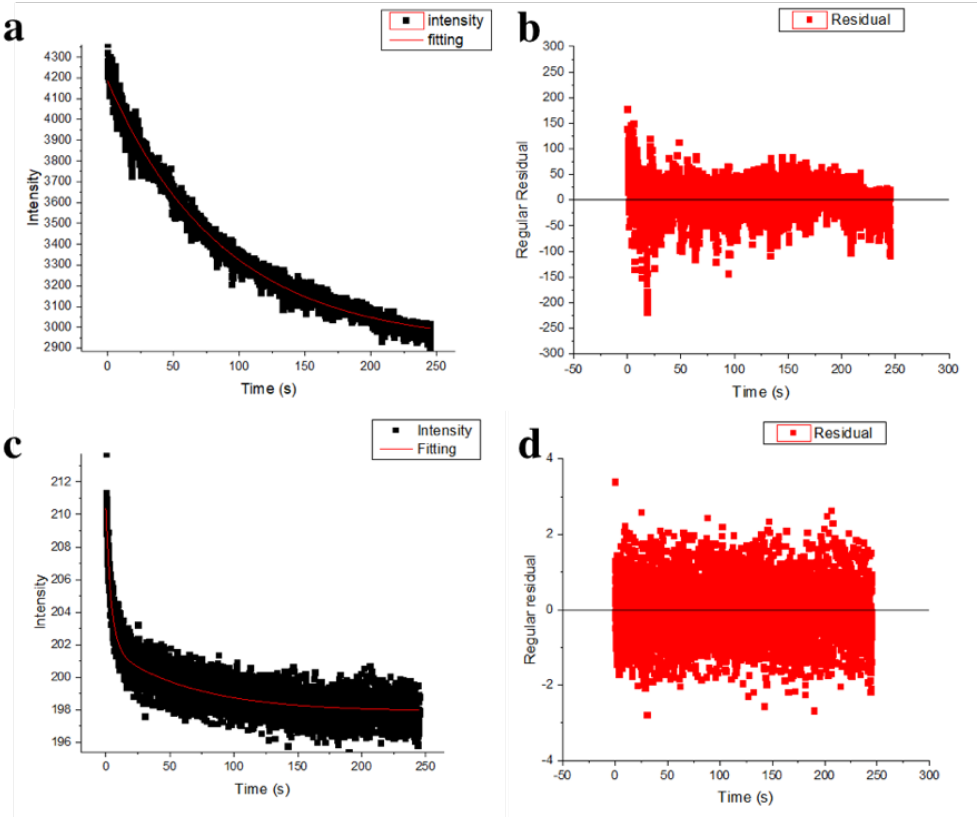

Figure 6.2: **Photo-decaying behavior of Dronpa-C12 under different conditions.** (a) Change of total signal intensity of each frame over acquisition time for the condition of Dronpa-C12 in microdroplets. The black dots are real measurements and the red curve is the fitting of mono-exponential decay. (b) Residual of the mono-exponential decay fitting in (a). (c) Change of total signal intensity of each frame over acquisition time for the condition of Dronpa-C12 in spin-coated PVA matrix. The black dots are real measurements and the red curve is the fitting of bi-exponential decay. (d) Residual of the bi-exponential decay fitting in (c).

ization, this information of rates versus pH values can be further utilized for studying the environment in live cells and how pH value changes during a specific dynamic process.

The excitation power has adverse effect on two photodecaying rates. As demonstrated in figure 6.4a,b, when the power is relatively low, k_1 increases as excitation power increases,

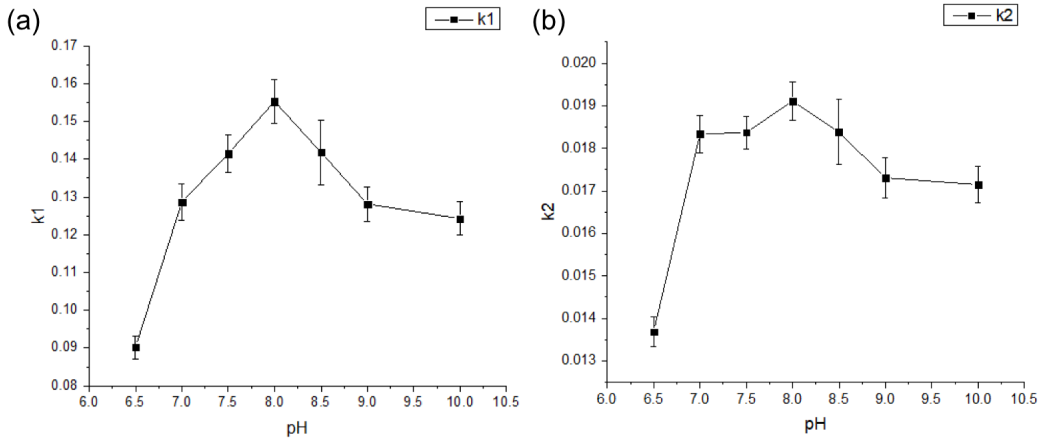

Figure 6.3: **Change of photo-decaying rates over different pH values.** The photo-decaying curves are fitted with bi-exponential decay functions, and the change of rates over pH values are plotted. Two rates have a simultaneous change as the pH value increases, and both reach the peak at around pH = 8.0.

meaning that fluorescent proteins stay at the "bright" state shorter. However, if the power keeps increasing, k_1 will reversely decrease and then remains a constant. In this process, k_2 decreases monotonically. This is because that when the intensity is too high, the system reaches a "stable" state quickly after starting pumping Dronpa-C12. The triplet state is fully occupied, avoiding more proteins to go to triplet state, and thus, dark state. A 405-nm illumination can re-activate fluorescent proteins to the bright state from the dark state. The addition of re-activation laser can greatly increase the lifetimes of Dronpa-C12. A low power of 405 nm (1% of power of 488 nm) is sufficient to decrease the photodecaying rates, while too high power of 405 nm may shorten the lifetime intensely (still longer than without re-activation) because it can also excite the protein, which goes to the dark state afterwards. As shown in figure 6.4c,d when the excitation power is low ($11W/cm^2$), as the re-activation power increases, k_1 and k_2 both increase.

In summary, reducing agent like DTT can prolong the photoblinking period if prepared

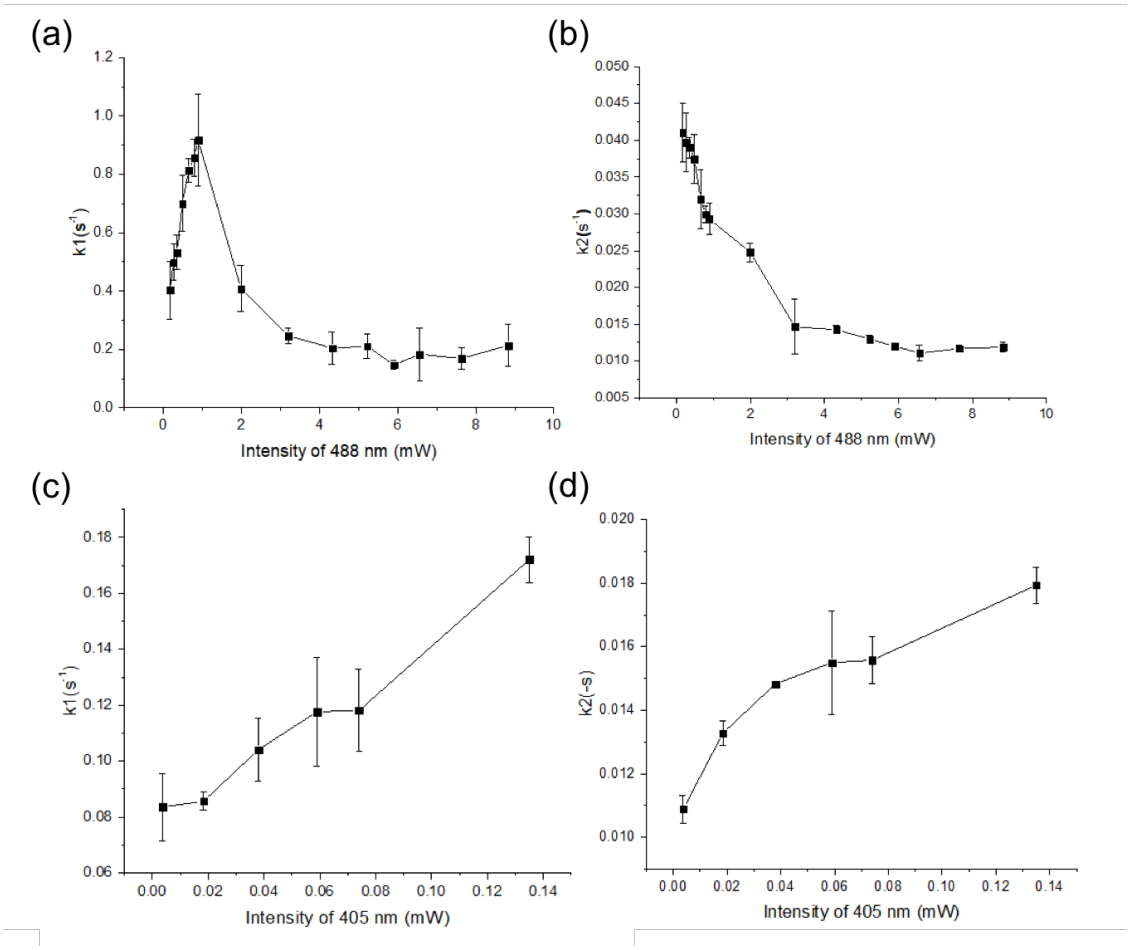

Figure 6.4: **Change of photo-decaying rates over different illumination powers.** By changing either the excitation (488 nm, (a,b)) or re-activation (405 nm, (c,d)) illumination individually, the change of two of rates over the corresponding illumination power are plotted. As for the excitation illumination, two rates do not change simultaneously. k_1 first increases then decreases (a), while k_2 has a monotonic increase as the excitation power increases. Both rates reach a plateau (stable value) at high excitation power. The addition of the re-activation illumination can greatly prolong the blinking duration and reduce the photo-decaying rates (c,d). Both rates keeps increasing as the power increases.

properly; pH values can control the photodecaying rates at around 8.0 where the quantum yield is highest, while Dronpa-C12 decays fastest; the change of the excitation and

re-activation powers can have a mixed effect on the response of the fluorescent protein.

6.4 Characterization of Dronpa-C12 SM photo-switching

Single-molecule (SM) photoswitching properties of fluorescent proteins are essential for the great performance of super-resolution imaging techniques like PALM and STORM. It is of special importance for SOFI analysis (chapter 5) because the algorithm is dependent on cumulant-related on-time ratio of the emitters [135]. A uniform sign (positive or negative) of on-time ratio may greatly reduce the artifacts of SOFI-processed images, and enhance the performance of higher-order SOFI. Thus, if the on-time ratio can be controlled with the excitation and re-activation lasers, we can build a feedback controller to actively tune it while a video is taken.

The on-time ratio (ρ) of the emitter is defined as

$$\rho = \frac{\tau_{on}}{\tau_{on} + \tau_{off}}$$

where τ_{on} and τ_{off} are the lifetime of the fluorescent protein in the bright and dark state, respectively. By tuning the concentration of the Dronpa-C12 solution for the spin-coating, we are able to achieve a diluted condition that single molecules are well separated on the coverslip and are resolvable for individual analysis. The general workflow for single-molecule blinking analysis is (1) accumulate all frames to get a total image of all emitters, (2) find and localize all single-molecule emitters, (3) crop out single emitters with squares and monitor and fluorescence intensity change throughout the whole acquisition, (4) find on- and off-state lifetimes of each single-molecule emitter from the time trace, and (5) calculate the on-time ratio based on the lifetimes. The change of lifetimes and on-time ratios over different illumination powers are shown in figure 6.5. The data was taken long enough for statistically significance. When the intensity of excitation laser increases, both on-time and off-time increases (figure 6.5a). On-time and off-time fluctuate reversely along a similar mean value when re-activation power increase (figure 6.5c). However, there is no apparent connection

between the illumination powers and $\rho$of Dronpa-C12 (figure 6.5b,d). Moreover, on-time-ratio fluctuates in a small range, which makes them impossible to be controlled for artifacts reduction for SOFI higher-order calculations. This might be due to that the change of lasers intensities are too little.

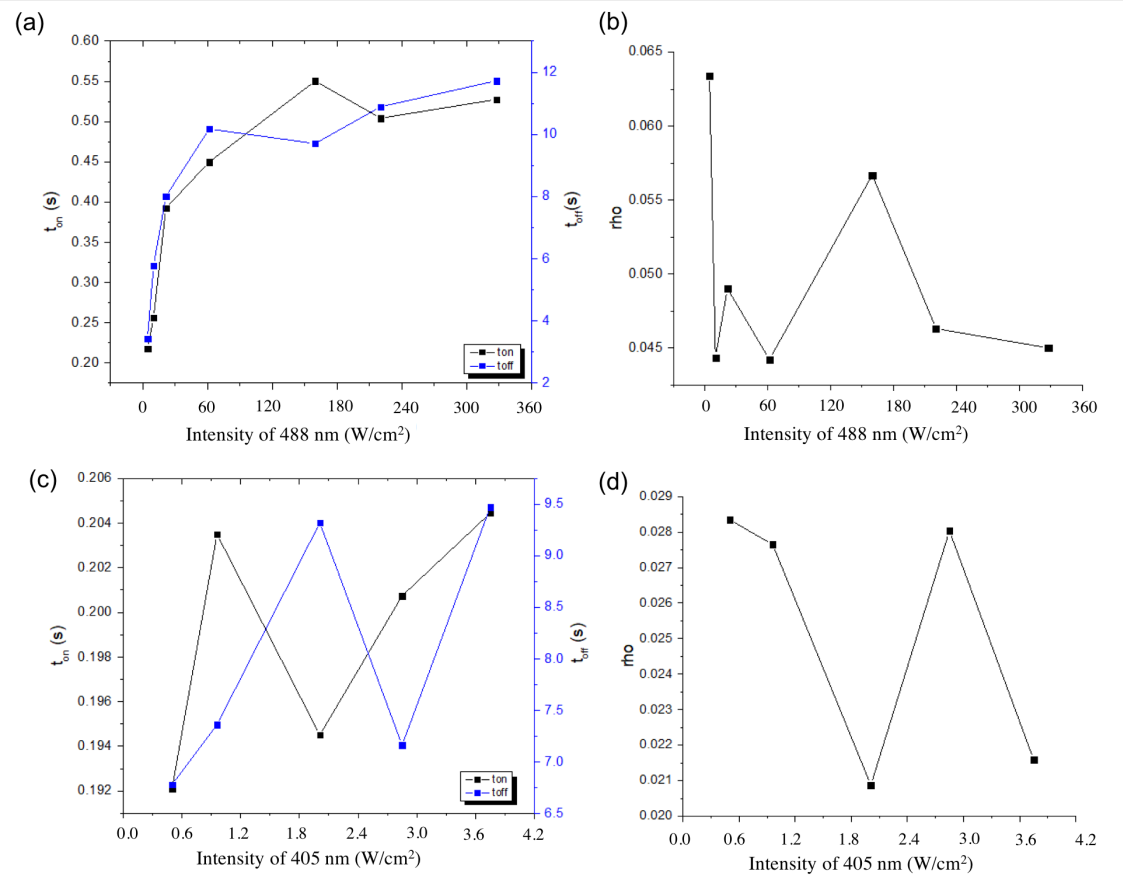

Figure 6.5: **Change of on-time ratio over different illumination powers.** By changing either the excitation (488 nm, (a,b)) or re-activation (405 nm, (c,d)) illumination individually, the change of on-time, off-time and ρ over the corresponding illumination power are plotted. Both on-time and off-time increase when the excitation power increases (a). However, we do not see clear trend for ρ (b). When the excitation power is fixed and the re-activation power increases, on-time and off-time fluctuate reversely along a similar mean value (c). The on-time ratio ρ fluctuates as well (d).

6.5 Conclusion

In this chapter, we explore the photophysical properties of a specific fluorescent protein, Dronpa-C12, at both ensemble and single-molecule level. The photo-decaying and photo-switching rates of Dronpa-C12 vary when the outside environment changes. Specifically, adding the reducing agent in a proper way and control the pH value of the local environment would prolong the blinking duration and slow down the photo-bleaching. Excitation and re-activation illumination intensities have a complex effect on both the bleaching rates and blinking rates of Dronpa-C12. our next step is to build up a robust model to explain the photophysical behaviors of Dronpa-C12. Fluorescence fluctuation spectroscopy will be used to detect the states of the fluorophore and their transition rates, and the connection between the different states and ensemble photodecaying behavior will be explored.

CHAPTER 7

Conclusion

The purpose of this dissertation is to understand and develop approaches for better plasmon-enhanced super-resolution imaging. Super-resolution imaging can be significantly improved by plasmon-enhanced single-molecule fluorescence imaging. In order to control and utilize plasmon enhancements for various applications, a better understanding of the light-matter interaction between plasmonic nanostructures and single-molecule emitters is needed. Meanwhile, a more accessible, user-friendly image processing tool can benefit the whole super-resolution community with image analysis experts and general users. A normalized emitter characterization workflow needs to be established as well before adopting any new fluorescent probes to monitor local field intensity or other local environment components. In this dissertation, these three topics are covered.

The basics of plasmonics and super-resolution fluorescence imaging are introduced in chapter 2 and chapter 3, respectively. In chapter 4, a home-built single-molecule polarization-resolved microscope is used to understand how the emission polarization and localization of single emitters (quantum dots) change upon interaction with a complex plasmonic nanoantenna contribution of different interaction types are explored. Single-molecule experiments and FDTD simulations demonstrate the fluorescence anisotropy and emission polarization rotation as the emitter moves closer to the plasmonic nanostructure. The mislocalization can be more than 100 nm, and the mispolarization can be 15 degrees. This inaccuracy would introduce significant error in plasmonic local field sensing using super-resolution fluorescence microscopy without a calibration and correction step. For a plasmonic nanoantenna with a

symmetrical structure (e.g., "L" shape with two identical arms), the extent of the mislocalization and mispolarization is determined by the emitter position relative to the symmetry axis of the structure. With a better understanding of the QD-plasmon interaction, the next step is to build an analytical model to understand the complex plasmonic system and use the model to predict the plasmonic near-fields. This would provide a practical method for plasmonic near-field mapping with higher precision. Moreover, at the end of this chapter, I also proposed a new sample preparation scheme combining nanofabrication and dip-pen nanolithography. Using this new method, single-molecule QDs can be positioned next to plasmonic nanoantennas with higher precision and throughput. This research topic can also be extended to help solve the inverse problem that predicts the plasmonic structure based on electromagnetic field mapping. An extensive collection of data can be generated using the proposed sample preparation method, connecting the mislocalization and mispolarization with the shape of the plasmonic structure and emitter's distance to it, and using these data to construct a machine learning model. L-shape will be one of the base structures for the model. Together with other base structures like nanowires and nanodisks, the whole contour of the structure can be determined by combining base structures.

Chapter 5 gives a thorough introduction on how the open-source *PySOFI* package is constructed and how to perform different SOFI analysis components using *PySOFI*. The *PySOFI* package adopts a simple architecture, where all the data processing steps are implemented as independent function modules, and only one class module is used to manage the data processing workflow. In this way, a fast prototype on new analysis can be achieved by disseminating and reorganizing the processing step. Moreover, the theory of two new image processing methods, local dynamic range compression (ldrc) and multi-order cumulant analysis (MOCA), are explained in detail. With these two new methods, the SOFI 2.0 analysis pipeline is able to help researchers capture fast cellular dynamics using SOFI without a sophisticated optical setup.

In chapter 6, a workflow of characterizing the photophysical properties of a fluorophore

is demonstrated. The change of photo-decaying and photo-switching rates as functions of parameters affected by the local environment are explored. The fluorophore shows a photo-decaying pattern of bi-exponential decay. Four parameters are studied, including oxygen level, pH value, the excitation illumination intensity, and the re-activation illumination intensity, and both rates show sensitive responses to the change of parameters. The relationship between photophysical properties and the local environment can be further used as an indicator of sub-cellular environmental change during dynamic processes.

I expect to see more work exploring the application of plamon-enhanced super-resolution imaging. Meanwhile, the topic of overcoming the mislocalization and mispolarization in fluorescence imaging-based plasmonic near-field mapping will be an ongoing research topic. Instead of using fluorescence intensity as the local field indicator, I expect to see exploration on using other photophysocal parameters (e.g., on-time ratio) of the fluorophore. I hope that the open-source, community-engaging *PySOFI* would attract more researchers to use SOFI for customized super-resolution image analysis.

REFERENCES

[1] Chao Zhan, Xue-Jiao Chen, Jun Yi, Jian-Feng Li, De-Yin Wu, and Zhong-Qun Tian. From plasmon-enhanced molecular spectroscopy to plasmon-mediated chemical reactions. *Nature Reviews Chemistry*, 2(9):216–230, 2018.

[2] Stefan A Maier et al. *Plasmonics: fundamentals and applications*, volume 1. Springer, 2007.

[3] Rupert F Oulton, Volker J Sorger, Thomas Zentgraf, Ren-Min Ma, Christopher Gladden, Lun Dai, Guy Bartal, and Xiang Zhang. Plasmon lasers at deep subwavelength scale. *Nature*, 461(7264):629–632, 2009.

[4] Mallia J Rupananda and N Subhash. *Photodiagnosis of Oral Malignancy using Laser-Induced Fluorescence and Diffuse Reflectance Spectroscopy*. PhD thesis, Cochin University of Science & Technology, 2008.

[5] Xiyu Yi. *Super resolution of Optical Fluctuation Imaging 2.0 (SOFI-2.0): Towards fast super resolved imaging of live cells*. University of California, Los Angeles, 2017.

[6] Pascal Anger, Palash Bharadwaj, and Lukas Novotny. Enhancement and quenching of single-molecule fluorescence. *Physical review letters*, 96(11):113002, 2006.

[7] Chad Ropp, Zachary Cummins, Sanghee Nah, John T Fourkas, Benjamin Shapiro, and Edo Waks. Nanoscale probing of image-dipole interactions in a metallic nanostructure. *Nature communications*, 6(1):1–8, 2015.

[8] Tiancheng Zuo, Harrison J Goldwyn, Benjamin P Isaacoff, David J Masiello, and Julie S Biteen. Rotation of single-molecule emission polarization by plasmonic nanorods. *The journal of physical chemistry letters*, 10(17):5047–5054, 2019.

[9] Xiyu Yi and Shimon Weiss. Cusp-artifacts in high order superresolution optical fluctuation imaging. *Biomedical optics express*, 11(2):554–570, 2020.

[10] Xiyu Yi, Sungho Son, Ryoko Ando, Atsushi Miyawaki, and Shimon Weiss. Moments reconstruction and local dynamic range compression of high order superresolution optical fluctuation imaging. *Biomedical optics express*, 10(5):2430–2445, 2019.

[11] Nader Engheta, Alessandro Salandrino, and Andrea Alu. Circuit elements at optical frequencies: nanoinductors, nanocapacitors, and nanoresistors. *Physical Review Letters*, 95(9):095504, 2005.

[12] Xin Guo, Min Qiu, Jiming Bao, Benjamin J Wiley, Qing Yang, Xining Zhang, Yaoguang Ma, Huakang Yu, and Limin Tong. Direct coupling of plasmonic and photonic nanowires for hybrid nanophotonic components and circuits. *Nano letters*, 9(12):4515–4519, 2009.

[13] Alexey V Krasavin, Sukanya Randhawa, Jean-Sebastien Bouillard, Jan Renger, Romain Quidant, and Anatoly V Zayats. Optically-programmable nonlinear photonic component for dielectric-loaded plasmonic circuitry. *Optics express*, 19(25):25222–25229, 2011.

[14] Andreas Tittl, Harald Giessen, and Na Liu. Plasmonic gas and chemical sensing. *Nanophotonics*, 3(3):157–180, 2014.

[15] Tuan Vo-Dinh, Andrew M Fales, Guy D Griffin, Christopher G Khoury, Yang Liu, Hoan Ngo, Stephen J Norton, Janna K Register, Hsin-Neng Wang, and Hsiangkuo Yuan. Plasmonic nanoprobes: from chemical sensing to medical diagnostics and therapy. *Nanoscale*, 5(21):10127–10140, 2013.

[16] Chanda Ranjit Yonzon, Eunhee Jeoung, Shengli Zou, George C Schatz, Milan Mrksich, and Richard P Van Duyne. A comparative analysis of localized and propagating surface plasmon resonance sensors: the binding of concanavalin a to a monosaccharide functionalized self-assembled monolayer. *Journal of the American Chemical Society*, 126(39):12669–12676, 2004.

[17] Robert Elghanian, James J Storhoff, Robert C Mucic, Robert L Letsinger, and Chad A Mirkin. Selective colorimetric detection of polynucleotides based on the distance-dependent optical properties of gold nanoparticles. *Science*, 277(5329):1078–1081, 1997.

[18] Aditi Das, Jing Zhao, George C Schatz, Stephen G Sligar, and Richard P Van Duyne. Screening of type i and ii drug binding to human cytochrome p450-3a4 in nanodiscs by localized surface plasmon resonance spectroscopy. *Analytical chemistry*, 81(10):3754–3759, 2009.

[19] Tuan Vo-Dinh, Hsin-Neng Wang, and Jonathan Scaffidi. Plasmonic nanoprobes for sers biosensing and bioimaging. *Journal of biophotonics*, 3(1-2):89–102, 2010.

[20] Seungah Lee, Yucheng Sun, Yingying Cao, and Seong Ho Kang. Plasmonic nanostructure-based bioimaging and detection techniques at the single-cell level. *TrAC Trends in Analytical Chemistry*, 117:58–68, 2019.

[21] Shutaro Onishi, Keiichiro Matsuishi, Jun Oi, Takuya Harada, Miyuki Kusaba, Kenichi Hirosawa, and Fumihiko Kannari. Spatiotemporal control of femtosecond plasmon using plasmon response functions measured by near-field scanning optical microscopy (nsom). *Optics express*, 21(22):26631–26641, 2013.

[22] Ziliang Ye, Shuang Zhang, Yuan Wang, Yong-Shik Park, Thomas Zentgraf, Guy Bartal, Xiaobo Yin, and Xiang Zhang. Mapping the near-field dynamics in plasmon-induced transparency. *Physical Review B*, 86(15):155148, 2012.

[23] Cheryl M Harris. Product review: shedding light on nsom, 2003.

[24] Michel Bosman, Vicki J Keast, Masashi Watanabe, Abbas I Maaroof, and Michael B Cortie. Mapping surface plasmons at the nanometre scale with an electron beam. *Nanotechnology*, 18(16):165505, 2007.

[25] Jaysen Nelayah, Mathieu Kociak, Odile Stéphan, F Javier García de Abajo, Marcel Tencé, Luc Henrard, Dario Taverna, Isabel Pastoriza-Santos, Luis M Liz-Marzán, and Christian Colliex. Mapping surface plasmons on a single metallic nanoparticle. *Nature Physics*, 3(5):348–353, 2007.

[26] Hu Cang, Anna Labno, Changgui Lu, Xiaobo Yin, Ming Liu, Christopher Gladden, Yongmin Liu, and Xiang Zhang. Probing the electromagnetic field of a 15-nanometre hotspot by single molecule imaging. *Nature*, 469(7330):385–388, 2011.

[27] Bing Fu, Jessica D Flynn, Benjamin P Isaacoff, David J Rowland, and Julie S Biteen. Super-resolving the distance-dependent plasmon-enhanced fluorescence of single dye and fluorescent protein molecules. *The Journal of Physical Chemistry C*, 119(33):19350–19358, 2015.

[28] Eric Betzig, George H Patterson, Rachid Sougrat, O Wolf Lindwasser, Scott Olenych, Juan S Bonifacino, Michael W Davidson, Jennifer Lippincott-Schwartz, and Harald F Hess. Imaging intracellular fluorescent proteins at nanometer resolution. *Science*, 313(5793):1642–1645, 2006.

[29] Chad Ropp, Zachary Cummins, Sanghee Nah, John T Fourkas, Benjamin Shapiro, and Edo Waks. Nanoscale imaging and spontaneous emission control with a single nano-positioned quantum dot. *Nature Communications*, 4(1):1–8, 2013.

[30] Mattin Urbieta, Marc Barbry, Yao Zhang, Peter Koval, Daniel Sánchez-Portal, Nerea Zabala, and Javier Aizpurua. Atomic-scale lightning rod effect in plasmonic picocavities: A classical view to a quantum effect. *ACS nano*, 12(1):585–595, 2018.

[31] Alberto Martín-Jiménez, Antonio I Fernández-Domínguez, Koen Lauwaet, Daniel Granados, Rodolfo Miranda, Francisco J García-Vidal, and Roberto Otero. Unveiling the radiative local density of optical states of a plasmonic nanocavity by stm. *Nature communications*, 11(1):1–8, 2020.

[32] Ekmel Ozbay. Plasmonics: merging photonics and electronics at nanoscale dimensions. *science*, 311(5758):189–193, 2006.

[33] Stefan A Maier, Pieter G Kik, Harry A Atwater, Sheffer Meltzer, Elad Harel, Bruce E Koel, and Ari AG Requicha. Local detection of electromagnetic energy transport below the diffraction limit in metal nanoparticle plasmon waveguides. *Nature materials*, 2(4):229–232, 2003.

[34] William L Barnes, Alain Dereux, and Thomas W Ebbesen. Surface plasmon subwavelength optics. *nature*, 424(6950):824–830, 2003.

[35] Christy L Haynes and Richard P Van Duyne. Dichroic optical properties of extended nanostructures fabricated using angle-resolved nanosphere lithography. *Nano Letters*, 3(7):939–943, 2003.

[36] Henri J Lezec, A Degiron, E Devaux, RA Linke, L Martin-Moreno, FJ Garcia-Vidal, and TW Ebbesen. Beaming light from a subwavelength aperture. *science*, 297(5582):820–822, 2002.

[37] S Wedge, JAE Wasey, William L Barnes, and I Sage. Coupled surface plasmon-polariton mediated photoluminescencefrom a top-emitting organic light-emitting structure. *Applied Physics Letters*, 85(2):182–184, 2004.

[38] Pm Andrew and WL Barnes. Energy transfer across a metal film mediated by surface plasmon polaritons. *Science*, 306(5698):1002–1005, 2004.

[39] George C Schatz and Richard P Van Duyne. Handbook of vibrational spectroscopy. *New York: Wiley*, 1:759, 2002.

[40] Amanda J Haes and Richard P Van Duyne. A unified view of propagating and localized surface plasmon resonance biosensors. *Analytical and bioanalytical chemistry*, 379(7):920–930, 2004.

[41] Jennifer M Brockman, Bryce P Nelson, and Robert M Corn. Surface plasmon resonance imaging measurements of ultrathin organic films. *Annual review of physical chemistry*, 51(1):41–63, 2000.

[42] Bruno Pettinger, Bin Ren, Gennaro Picardi, Rolf Schuster, and Gerhard Ertl. Nanoscale probing of adsorbed species by tip-enhanced raman spectroscopy. *Physical review letters*, 92(9):096101, 2004.

[43] Mark W Knight, Nicholas S King, Lifei Liu, Henry O Everitt, Peter Nordlander, and Naomi J Halas. Aluminum for plasmonics. *ACS nano*, 8(1):834–840, 2014.

[44] George H Chan, Jing Zhao, Erin M Hicks, George C Schatz, and Richard P Van Duyne. Plasmonic properties of copper nanoparticles fabricated by nanosphere lithography. *Nano letters*, 7(7):1947–1952, 2007.

[45] Amanda J Haes, Christy L Haynes, Adam D McFarland, George C Schatz, Richard P Van Duyne, and Shengli Zou. Plasmonic materials for surface-enhanced sensing and spectroscopy. *MRS bulletin*, 30(5):368–375, 2005.

[46] Sergey I Bozhevolnyi. Plasmonic nano-guides and circuits. In *Plasmonics and Metamaterials*, page MWD3. Optical Society of America, 2008.

[47] Prashant Nagpal, Nathan C Lindquist, Sang-Hyun Oh, and David J Norris. Ultrasmooth patterned metals for plasmonics and metamaterials. *Science*, 325(5940):594–597, 2009.

[48] Xi Gao, Jin Hui Shi, Xiaopeng Shen, Hui Feng Ma, Wei Xiang Jiang, Lianming Li, and Tie Jun Cui. Ultrathin dual-band surface plasmonic polariton waveguide and frequency splitter in microwave frequencies. *Applied Physics Letters*, 102(15):151912, 2013.

[49] G Lerosey, DFP Pile, P Matheu, G Bartal, and X Zhang. Controlling the phase and amplitude of plasmon sources at a subwavelength scale. *Nano letters*, 9(1):327–331, 2009.

[50] Zheyu Fang, Junyi Cai, Zhongbo Yan, Peter Nordlander, Naomi J Halas, and Xing Zhu. Removing a wedge from a metallic nanodisk reveals a fano resonance. *Nano letters*, 11(10):4475–4479, 2011.

[51] Terukazu Kosako, Yutaka Kadoya, and Holger F Hofmann. Directional control of light by a nano-optical yagi–uda antenna. *Nature Photonics*, 4(5):312–315, 2010.

[52] Junxi Zhang, Lide Zhang, and Wei Xu. Surface plasmon polaritons: physics and applications. *Journal of Physics D: Applied Physics*, 45(11):113001, 2012.

[53] Marie Richard-Lacroix and Volker Deckert. Direct molecular-level near-field plasmon and temperature assessment in a single plasmonic hotspot. *Light: Science & Applications*, 9(1):1–13, 2020.

[54] Masud Mansuripur, Armis R Zakharian, A Lesuffleur, Sang-Hyun Oh, RJ Jones, NC Lindquist, Hyungsoon Im, A Kobyakov, and JV Moloney. Plasmonic nanostructures for optical data storage. *Optics Express*, 17(16):14001–14014, 2009.

[55] Francisco J Rodríguez-Fortuño, Giuseppe Marino, Pavel Ginzburg, Daniel O'Connor, Alejandro Martínez, Gregory A Wurtz, and Anatoly V Zayats. Near-field interference for the unidirectional excitation of electromagnetic guided modes. *Science*, 340(6130):328–330, 2013.

[56] Daniel O'Connor and Anatoly V Zayats. The third plasmonic revolution. *Nature nanotechnology*, 5(7):482–483, 2010.

[57] Frédéric Goettmann, Audrey Moores, Cédric Boissière, Pascal Le Floch, and Clément Sanchez. A selective chemical sensor based on the plasmonic response of phosphinine-stabilized gold nanoparticles hosted on periodically organized mesoporous silica thin layers. *Small*, 1(6):636–639, 2005.

[58] Christophe Caucheteur, Tuan Guo, and Jacques Albert. Review of plasmonic fiber optic biochemical sensors: improving the limit of detection. *Analytical and bioanalytical chemistry*, 407(14):3883–3897, 2015.

[59] Yeşeren Saylan, Semra Akgönüllü, and Adil Denizli. Plasmonic sensors for monitoring biological and chemical threat agents. *Biosensors*, 10(10):142, 2020.

[60] Tahir Iqbal and Sumera Afsheen. One dimensional plasmonic grating: high sensitive biosensor. *Plasmonics*, 12(1):19–25, 2017.

[61] Grace M Hwang, Lin Pang, Elaine H Mullen, and Yeshaiahu Fainman. Plasmonic sensing of biological analytes through nanoholes. *IEEE sensors journal*, 8(12):2074–2079, 2008.

[62] Mohammad Al Mahfuz, Md Aslam Mollah, Moriom Rojy Momota, Alok Kumar Paul, Al Masud, Sanjida Akter, and Md Rabiul Hasan. Highly sensitive photonic crystal fiber plasmonic biosensor: Design and analysis. *Optical Materials*, 90:315–321, 2019.

[63] Feng Hao, Yannick Sonnefraud, Pol Van Dorpe, Stefan A Maier, Naomi J Halas, and Peter Nordlander. Symmetry breaking in plasmonic nanocavities: subradiant lspr sensing and a tunable fano resonance. *Nano letters*, 8(11):3983–3988, 2008.

[64] Jacob Khurgin, Wei-Yi Tsai, Din Ping Tsai, and Greg Sun. Landau damping and limit to field confinement and enhancement in plasmonic dimers. *Acs Photonics*, 4(11):2871–2880, 2017.

[65] Stefan W Hell and Jan Wichmann. Breaking the diffraction resolution limit by stimulated emission: stimulated-emission-depletion fluorescence microscopy. *Optics letters*, 19(11):780–782, 1994.

[66] Michael J Rust, Mark Bates, and Xiaowei Zhuang. Sub-diffraction-limit imaging by stochastic optical reconstruction microscopy (storm). *Nature methods*, 3(10):793–796, 2006.

[67] David L Mack, Emiliano Cortés, Vincenzo Giannini, Peter Török, Tyler Roschuk, and Stefan A Maier. Decoupling absorption and emission processes in super-resolution localization of emitters in a plasmonic hotspot. *Nature communications*, 8(1):1–10, 2017.

[68] Thomas Dertinger, Ryan Colyer, Gopal Iyer, Shimon Weiss, and Jörg Enderlein. Fast, background-free, 3d super-resolution optical fluctuation imaging (sofi). *Proceedings of the National Academy of Sciences*, 106(52):22287–22292, 2009.

[69] Thomas Dertinger, Ryan Colyer, Robert Vogel, Jörg Enderlein, and Shimon Weiss. Achieving increased resolution and more pixels with superresolution optical fluctuation imaging (sofi). *Optics express*, 18(18):18875–18885, 2010.

[70] Joseph R Lakowicz. *Principles of fluorescence spectroscopy*. Springer science & business media, 2013.

[71] Daniel Darvill, Anthony Centeno, and Fang Xie. Plasmonic fluorescence enhancement by metal nanostructures: shaping the future of bionanotechnology. *Physical Chemistry Chemical Physics*, 15(38):15709–15726, 2013.

[72] Edward M Purcell, Henry Cutler Torrey, and Robert V Pound. Resonance absorption by nuclear magnetic moments in a solid. *Physical review*, 69(1-2):37, 1946.

[73] Vincenzo Giannini, Antonio I Fernández-Domínguez, Susannah C Heck, and Stefan A Maier. Plasmonic nanoantennas: fundamentals and their use in controlling the radiative properties of nanoemitters. *Chemical reviews*, 111(6):3888–3912, 2011.

[74] Johannes Gutmann, Hans Zappe, and Jan Christoph Goldschmidt. Quantitative modeling of fluorescent emission in photonic crystals. *Physical Review B*, 88(20):205118, 2013.

[75] OL Muskens, V Giannini, José A Sánchez-Gil, and J Gómez Rivas. Strong enhancement of the radiative decay rate of emitters by single plasmonic nanoantennas. *Nano letters*, 7(9):2871–2875, 2007.

[76] Katherine A Willets and Richard P Van Duyne. Localized surface plasmon resonance spectroscopy and sensing. *Annu. Rev. Phys. Chem.*, 58:267–297, 2007.

[77] Kathryn M Mayer and Jason H Hafner. Localized surface plasmon resonance sensors. *Chemical reviews*, 111(6):3828–3857, 2011.

[78] Jeffrey N Anker, W Paige Hall, Olga Lyandres, Nilam C Shah, Jing Zhao, and Richard P Van Duyne. Biosensing with plasmonic nanosensors. *Nanoscience and Technology: A Collection of Reviews from Nature Journals*, pages 308–319, 2010.

[79] Timur Shegai, Zhipeng Li, Tali Dadosh, Zhenyu Zhang, Hongxing Xu, and Gilad Haran. Managing light polarization via plasmon–molecule interactions within an asymmetric metal nanoparticle trimer. *Proceedings of the National Academy of Sciences*, 105(43):16448–16453, 2008.

[80] Hari Shroff, Helen White, and Eric Betzig. Photoactivated localization microscopy (palm) of adhesion complexes. *Current protocols in cell biology*, 58(1):4–21, 2013.

[81] Mark Bates, Bo Huang, Graham T Dempsey, and Xiaowei Zhuang. Multicolor super-resolution imaging with photo-switchable fluorescent probes. *Science*, 317(5845):1749–1753, 2007.

[82] Hongzhen Lin, Silvia P Centeno, Liang Su, Bart Kenens, Susana Rocha, Michel Sliwa, Johan Hofkens, and Hiroshi Uji-i. Mapping of surface-enhanced fluorescence on metal nanoparticles using super-resolution photoactivation localization microscopy. *ChemPhysChem*, 13(4):973–981, 2012.

[83] Katherine A Willets. Super-resolution imaging of interactions between molecules and plasmonic nanostructures. *Physical Chemistry Chemical Physics*, 15(15):5345–5354, 2013.

[84] TH Taminiau, FD Stefani, Franciscus B Segerink, and NF Van Hulst. Optical antennas direct single-molecule emission. *Nature photonics*, 2(4):234–237, 2008.

[85] Liang Su, Haifeng Yuan, Gang Lu, Susana Rocha, Michel Orrit, Johan Hofkens, and Hiroshi Uji-i. Super-resolution localization and defocused fluorescence microscopy on resonantly coupled single-molecule, single-nanorod hybrids. *ACS nano*, 10(2):2455–2466, 2016.

[86] Mario Raab, Carolin Vietz, Fernando Daniel Stefani, Guillermo Pedro Acuna, and Philip Tinnefeld. Shifting molecular localization by plasmonic coupling in a single-molecule mirage. *Nature communications*, 8(1):1–6, 2017.

[87] Harrison J Goldwyn, Kevin C Smith, Jacob A Busche, and David J Masiello. Mislocalization in plasmon-enhanced single-molecule fluorescence microscopy as a dynamical young's interferometer. *ACS Photonics*, 5(8):3141–3151, 2018.

[88] Esther A Wertz, Benjamin P Isaacoff, and Julie S Biteen. Wavelength-dependent super-resolution images of dye molecules coupled to plasmonic nanotriangles. *Acs Photonics*, 3(10):1733–1740, 2016.

[89] Rashad Baiyasi, Seyyed Ali Hosseini Jebeli, Qingfeng Zhang, Liang Su, Johan Hofkens, Hiroshi Uji-i, Stephan Link, and Christy F Landes. Psf distortion in dye–plasmonic nanomaterial interactions: Friend or foe? *Acs Photonics*, 6(3):699–708, 2019.

[90] Alberto G Curto, Giorgio Volpe, Tim H Taminiau, Mark P Kreuzer, Romain Quidant, and Niek F van Hulst. Unidirectional emission of a quantum dot coupled to a nanoantenna. *Science*, 329(5994):930–933, 2010.

[91] Esther Wertz, Benjamin P Isaacoff, Jessica D Flynn, and Julie S Biteen. Single-molecule super-resolution microscopy reveals how light couples to a plasmonic nanoantenna on the nanometer scale. *Nano letters*, 15(4):2662–2670, 2015.

[92] Tim H Taminiau, Fernando D Stefani, and Niek F van Hulst. Enhanced directional excitation and emission of single emitters by a nano-optical yagi-uda antenna. *Optics express*, 16(14):10858–10866, 2008.

[93] Mengxin Ren, Mo Chen, Wei Wu, Lihui Zhang, Junku Liu, Biao Pi, Xinzheng Zhang, Qunqing Li, Shoushan Fan, and Jingjun Xu. Linearly polarized light emission from quantum dots with plasmonic nanoantenna arrays. *Nano letters*, 15(5):2951–2957, 2015.

[94] Farah Dawood, Jun Wang, Peter A Schulze, Chris J Sheehan, Matthew R Buck, Allison M Dennis, Somak Majumder, Sachi Krishnamurthy, Matthew Ticknor, Isabelle Staude, et al. The role of liquid ink transport in the direct placement of quantum dot emitters onto sub-micrometer antennas by dip-pen nanolithography. *Small*, 14(31):1801503, 2018.

[95] Marta Cerruti, Crissy Rhodes, Mark Losego, Alina Efremenko, Jon-Paul Maria, Daniel Fischer, Stefan Franzen, and Jan Genzer. Influence of indium–tin oxide surface structure on the ordering and coverage of carboxylic acid and thiol monolayers. *Journal of Physics D: Applied Physics*, 40(14):4212, 2007.

[96] H Abudayyeh, A Blake, A Bräuer, D Liran, B Lubotzky, S Majumder, J Hollingsworth, M Fleischer, and R Rapaport. Highly efficient and pure single photon streams at room-temperature by deterministic nano positioning of quantum emitters. In *CLEO: Applications and Technology*, pages AM1S–7. Optical Society of America, 2021.

[97] Kim I Mortensen, L Stirling Churchman, James A Spudich, and Henrik Flyvbjerg. Optimized localization analysis for single-molecule tracking and super-resolution microscopy. *Nature methods*, 7(5):377–381, 2010.

[98] John B Schneider. Understanding the finite-difference time-domain method. *School of electrical engineering and computer science Washington State University*, 28, 2010.

[99] Peter B Johnson and R-WJPrB Christy. Optical constants of the noble metals. *Physical review B*, 6(12):4370, 1972.

[100] Kristin Grußmayer, Tomas Lukes, Theo Lasser, and Aleksandra Radenovic. Self-blinking dyes unlock high-order and multiplane super-resolution optical fluctuation imaging. *ACS nano*, 14(7):9156–9165, 2020.

[101] S Duwé, W Vandenberg, and P Dedecker. Live-cell monochromatic dual-label sub-diffraction microscopy by mt-pcsofi. *Chemical Communications*, 53(53):7242–7245, 2017.

[102] Benjamien Moeyaert and Peter Dedecker. Pcsofi as a smart label-based superresolution microscopy technique. In *Photoswitching Proteins*, pages 261–276. Springer, 2014.

[103] Sam Duwé, Benjamien Moeyaert, and Peter Dedecker. Diffraction-unlimited fluorescence microscopy of living biological samples using pcsofi. *Current protocols in chemical biology*, 7(1):27–41, 2015.

[104] Peter Dedecker, Gary CH Mo, and Jin Zhang. Widely accessible method for super-resolution fluorescence imaging of living systems. *Biophysical Journal*, 104(2):535a, 2013.

[105] Stefan Geissbuehler, Noelia L Bocchio, Claudio Dellagiacoma, Corinne Berclaz, Marcel Leutenegger, and Theo Lasser. Mapping molecular statistics with balanced super-resolution optical fluctuation imaging (bsofi). *Optical Nanoscopy*, 1(1):1–7, 2012.

[106] Simon C Stein, Anja Huss, Dirk Hähnel, Ingo Gregor, and Jörg Enderlein. Fourier interpolation stochastic optical fluctuation imaging. *Optics express*, 23(12):16154–16163, 2015.

[107] S Vlasenko, AB Mikhalychev, IL Karuseichyk, DA Lyakhov, Dominik L Michels, and D Mogilevtsev. Optimal correlation order in superresolution optical fluctuation microscopy. *Physical Review A*, 102(6):063507, 2020.

[108] Dario Cevoli, Raffaele Vitale, Wim Vandenberg, Siewert Hugelier, Robin Van den Eynde, Peter Dedecker, and Cyril Ruckebusch. Design of experiments for the optimization of sofi super-resolution microscopy imaging. *Biomedical Optics Express*, 12(5):2617–2630, 2021.

[109] Baoju Wang, Zhijia Liu, Li Zhou, Yiyan Fei, Chengliang Yang, Lan Mi, Quanquan Mu, and Jiong Ma. Active-modulated, random-illumination, super-resolution optical fluctuation imaging. *Nanoscale*, 12(32):16864–16874, 2020.

[110] Adrien Descloux, KS Grußmayer, E Bostan, T Lukes, Arno Bouwens, A Sharipov, S Geissbuehler, A-L Mahul-Mellier, HA Lashuel, M Leutenegger, et al. Combined multi-plane phase retrieval and super-resolution optical fluctuation imaging for 4d cell microscopy. *Nature Photonics*, 12(3):165–172, 2018.

[111] Eliel Hojman, Thomas Chaigne, Oren Solomon, Sylvain Gigan, Emmanuel Bossy, Yonina C Eldar, and Ori Katz. Photoacoustic imaging beyond the acoustic diffraction-limit with dynamic speckle illumination and sparse joint support recovery. *Optics express*, 25(5):4875–4886, 2017.

[112] MinKwan Kim, ChungHyun Park, Christophe Rodriguez, YongKeun Park, and Yong-Hoon Cho. Superresolution imaging with optical fluctuation using speckle patterns illumination. *Scientific reports*, 5(1):1–10, 2015.

[113] Ori Katz and Noam Shekel. Using fiber-bending generated speckles for improved working distance and. *Optics Letters*, 4(C1):C2, 2020.

[114] Lydia Kisley, Rachel Brunetti, Lawrence J Tauzin, Bo Shuang, Xiyu Yi, Alec W Kirkeminde, Daniel A Higgins, Shimon Weiss, and Christy F Landes. Characterization of porous materials by fluorescence correlation spectroscopy super-resolution optical fluctuation imaging. *ACS nano*, 9(9):9158–9166, 2015.

[115] Stefan Geissbuehler, Azat Sharipov, Aurélien Godinat, Noelia L Bocchio, Patrick A Sandoz, Anja Huss, Nickels A Jensen, Stefan Jakobs, Jörg Enderlein, F Gisou Van Der Goot, et al. Live-cell multiplane three-dimensional super-resolution optical fluctuation imaging. *Nature communications*, 5(1):1–7, 2014.

[116] Ashley M Rozario, Fabian Zwettler, Sam Duwé, Riley B Hargreaves, Aaron Brice, Peter Dedecker, Markus Sauer, Gregory W Moseley, Donna R Whelan, and Toby DM Bell. Corrigendum to:'live and large': Super-resolution optical fluctuation imaging (sofi) and expansion microscopy (exm) of microtubule remodelling by rabies virus p protein. *Australian Journal of Chemistry*, 73(8):822–822, 2020.

[117] Peter Dedecker, Sam Duwé, Robert K Neely, and Jin Zhang. Localizer: fast, accurate, open-source, and modular software package for superresolution microscopy. *Journal of biomedical optics*, 17(12):126008, 2012.

[118] Harry Nyquist. Certain topics in telegraph transmission theory. *Transactions of the American Institute of Electrical Engineers*, 47(2):617–644, 1928.

[119] Claude E Shannon. A mathematical theory of communication. *The Bell system technical journal*, 27(3):379–423, 1948.

[120] Kevin Jolly. *Hands-On Data Visualization with Bokeh: Interactive Web Plotting for Python Using Bokeh*. Packt Publishing Ltd, 2018.

[121] Jörg Wiedenmann, Sergey Ivanchenko, Franz Oswald, Florian Schmitt, Carlheinz Röcker, Anya Salih, Klaus-Dieter Spindler, and G Ulrich Nienhaus. Eosfp, a fluorescent marker protein with uv-inducible green-to-red fluorescence conversion. *Proceedings of the National Academy of Sciences*, 101(45):15905–15910, 2004.

[122] Dmitriy M Chudakov, Vladislav V Verkhusha, Dmitry B Staroverov, Ekaterina A Souslova, Sergey Lukyanov, and Konstantin A Lukyanov. Photoswitchable cyan fluorescent protein for protein tracking. *Nature biotechnology*, 22(11):1435–1439, 2004.

[123] Dmitriy M Chudakov, Vsevolod V Belousov, Andrey G Zaraisky, Vladimir V Novoselov, Dmitry B Staroverov, Dmitry B Zorov, Sergey Lukyanov, and Konstantin A Lukyanov. Kindling fluorescent proteins for precise in vivo photolabeling. *Nature biotechnology*, 21(2):191–194, 2003.

[124] Mark Bates, Timothy R Blosser, and Xiaowei Zhuang. Short-range spectroscopic ruler based on a single-molecule optical switch. *Physical review letters*, 94(10):108101, 2005.

[125] Mike Heilemann, Emmanuel Margeat, Robert Kasper, Markus Sauer, and Philip Tinnefeld. Carbocyanine dyes as efficient reversible single-molecule optical switch. *Journal of the American Chemical Society*, 127(11):3801–3806, 2005.

[126] Graham T Dempsey, Joshua C Vaughan, Kok Hao Chen, Mark Bates, and Xiaowei Zhuang. Evaluation of fluorophores for optimal performance in localization-based super-resolution imaging. *Nature methods*, 8(12):1027–1036, 2011.

[127] Taekjip Ha and Philip Tinnefeld. Photophysics of fluorescent probes for single-molecule biophysics and super-resolution imaging. *Annual review of physical chemistry*, 63:595–617, 2012.

[128] Ryoko Ando, Hideaki Mizuno, and Atsushi Miyawaki. Regulated fast nucleocytoplasmic shuttling observed by reversible protein highlighting. *Science*, 306(5700):1370–1373, 2004.

[129] Satoshi Habuchi, Ryoko Ando, Peter Dedecker, Wendy Verheijen, Hideaki Mizuno, Atsushi Miyawaki, and Johan Hofkens. Reversible single-molecule photoswitching in the gfp-like fluorescent protein dronpa. *Proceedings of the National Academy of Sciences*, 102(27):9511–9516, 2005.

[130] Oleksii Nevskyi, Dmytro Sysoiev, Jes Dreier, Simon Christoph Stein, Alex Oppermann, Florian Lemken, Tobias Janke, Jörg Enderlein, Ilaria Testa, Thomas Huhn, et al. Fluorescent diarylethene photoswitches—a universal tool for super-resolution microscopy in nanostructured materials. *Small*, 14(10):1703333, 2018.

[131] J Rault, R Gref, ZH Ping, QT Nguyen, and J Néel. Glass transition temperature regulation effect in a poly (vinyl alcohol)—water system. *Polymer*, 36(8):1655–1661, 1995.

[132] Heon Sang Lee and Woo Nyon Kim. Glass transition temperatures and rigid amorphous fraction of poly (ether ether ketone) and poly (ether imide) blends. *Polymer*, 38(11):2657–2663, 1997.

[133] P Törmälä. Determination of glass transition temperature of poly (ethylene glycol) by spin probe technique. *European Polymer Journal*, 10(6):519–521, 1974.

[134] MZ Islam, A Noori, and S Paul. Photobleaching and its kinetics of fluorescein dyes in pva polymer matrices: A review. *Austin J. Anal. Pharm. Chem*, 4:1092–1097, 2017.

[135] Eli Barkai, Frank LH Brown, Michel Orrit, and Haw Yang. *Theory and evaluation of single-molecule signals*. World Scientific, 2008.